May 2020

Atomic Data Needs in Laboratory Astrophysics: Experimental Methods for Spectroscopy and Charge Exchange with Ions

Steven James Bromley
Clemson University, steven.bromley@gmail.com

Follow this and additional works at: https://tigerprints.clemson.edu/all_dissertations

Atomic Data Needs in Laboratory Astrophysics: Experimental Methods for Spectroscopy and Charge Exchange with Ions

A Dissertation
Presented to
the Graduate School of
Clemson University

In Partial Fulfillment
of the Requirements for the Degree
Doctor of Philosophy
Physics

by
Steven James Bromley
May 2020

Accepted by:
Dr. Joan Marler, Committee Chair
Dr. Chad Sosolik
Dr. Bradley Mayer
Dr. Stephen Kaeppler

Abstract

Modeling the spectra of astrophysical environments requires knowledge of the absolute cross sections for the relevant interactions occuring between ions and neutrals. Two of the common processes are a) charge transfer, which has been shown to be the source of cometary x-rays, and b) spontaneous emission, which is used as an abundance diagnostic in studies of stellar atmospheres and other exotic environments. Understanding the source of observed emission lines, e.g. charge exchange or de-excitation, will require an understanding of the electronic structure of each element in the environment being studied. This dissertation examines the charge exchange process with singly charged ions and investigates spontaneous emission from heavy atoms and ions.

Charge exchange measurements are typically performed either with a gas cell or with a gas jet. For absolute cross sections, a gas cell provides a well defined pressure and path length. The design and experimental procedure for a gas cell based experiment optimized for interactions expected to have large cross sections is discussed. Charge exchange cross sections are reported for the four symmetric ion-neutral reactions He^+-He, Ne^+-Ne, Ar^+-Ar, and Kr^+-Kr between 0.2 - 5.0 keV and compared to the available experimental and theoretical results. Extrapolation of a fit to the current data using the theoretically suggested functional form provides good agreement even with the available high energy experimental results. A modified

gas cell with improved gas conductance and the ability to scan the collision energy without altering the ion source parameters is also described.

For interactions where it is desired to extract both the product ions and/or photons from the interaction region, a crossed beam set-up is required. A gas jet provides near-complete optical access to the interaction region but a less rigidly defined pressure and path length. Two gas jets were designed for future cossed-beam experiments involving solar wind ions and simple neutrals. The first design is intended for delivering neutral beams with central densities of order 10^6 - 10^7 cm^{-3} to the CUEBIT drift tubes for producing metal ions. The operation of the jet is consistent with a simple theoretical model. A second gas jet, intended for operation at higher backing pressures, is presented and expected to produce dense targets ($n > 10^{10}$ cm^{-3}) to a crossed-beam apparatus downstream from CUEBIT.

In environments containing heavy elements, emission lines may be used to estimate the abundances of these heavy species. Therefore accurate knowledge of the electronic structure of both the ground and higher charge states of the elements is required for interpretation of the astrophysical spectra where these elements may be found, e.g. kilonovae or solar wind interactions. The electronic structure of Au I - II was studied by observing emission from gold targets ablated inside the Compact Toroidal Hybrid plasma apparatus at Auburn University. Gold lines were identified by their time-dependent behavior when compared to similar spectra of nickel targets. New emission lines are found by comparing the observed spectra to Ritz wavelengths calculated from level energies in the literature. Level lists and line lists of dipole-allowed transitions spanning 187 - 800nm are reported for Au I & II with resolution $\frac{\Delta\lambda}{\lambda} < 10^{-4}$. It is expected that these results will contribute to the understanding and interpretation of spectra from neutron star mergers and chemically peculiar stars.

Dedication

This work is dedicated to my best friend, W. Bromley, without whose golden heart this work would not have been possible.

Acknowledgments

Someone once told me that the acknowledgement section of any dissertation was often the first (and sometimes only) read portion by any of your curious peers. There have been a large number of people who have contributed to, affected, or otherwise helped me complete this work, and I have tried to be as complete as possible in acknowledging them. If I have forgotten to include you, I extend my sincerest apologies.

First, the various projects in this work would not have been possible without funding from the Clemson University College of Science, the National Science Foundation (NSF), the National Aeronautics and Space Administration (NASA), and the Department of Energy. Second, there are many people I would like to thank for their help and contributions in completing this work. First and foremost, I would like to thank my advisor, Dr. Joan Marler, for her guidance, useful critiques, and support as I've completed this work. When I came to Clemson, I had intended to study Astronomy, and I now find myself immersed in the world of experiment; I am forever thankful to my advisor for introducing me to the exciting world of experimental physics. I would also like to acknowledge the comments, critiques, and guidance of my committee members: Drs. Chad Sosolik, Bradley Meyer, and Stephen Kaeppler. Dr. Jim Harriss, thank you for the kind words, advice, and excellent coffee as I worked on the gas cells and gas jets. You also taught me a number of skills related to working

Table of Contents

List of Tables

List of Figures

List of Appendices

Chapter 1

Introduction

Astronomy is one of humanity's oldest sciences. Initially used for ceremonies and tracking the seasons, the science has expanded considerably. Starting in the 20th century with the advent of ground- and space-based telescopes, these new tools have expanded the astronomer's capabilities to precisely measure the spectral signatures of the cosmos from the infrared to highly energetic gamma rays. Interpreting these spectral signatures ultimately requires comparison to laboratory studies of the underlying physics. These laboratory studies may be of the most fundamental nature, e.g. the discovery of x- and gamma-rays, to more applied contexts such as the development of new detectors.

Today, astronomy is strongly supported by laboratory studies. In recent years, we have seen (to name a few) developments on the identification of emission lines, studies of plasma dynamics, limits on molecular reaction rates derived from trapped ions, and even the conceptualization of new observatories [1]. As noted by Brickhouse *et al.* [1], astronomy and the experimental sciences are intimately linked and will continue to be into the foreseeable future. Just as experimental studies have proven beneficial for astrophysics, both in the conception of scientific missions and

programs to their scientific returns, astronomy has emerged as an important motivator for experimental sciences in areas of atomic physics, condensed matter physics, fusion science, navigation systems, and more fundamental fields such as spectroscopy [1]. These experimental efforts with relevance to astronomy are often categorized under the umbrella of "Laboratory Astrophysics," or more informally as "Lab Astro" [1]. In the following two sections, the areas of Lab Astro relevant to this dissertation are introduced.

1.1 Atomic Data for Charge Exchange in Astrophysics

Despite its uncommonness on Earth, plasma is the predominant state of matter in astrophysical environments, and this exotic state of matter leads to a number of interesting interactions. Astrophysical plasmas consist of electrons, ions, and neutrals interacting with the particles and electromagnetic fields around them. Common interactions between particles in these plasmas include electron impact ionization (EII), where an electron ionizes an atom or ion

$$e^- + A^{q+} \rightarrow A^{(q+1)+} + 2e^- \tag{1.1}$$

or electron impact excitation (EIE), where the ion or atom is electronically excited

$$e^- + A \rightarrow A^* + e^- \tag{1.2}$$

This excitation is often followed by spontaneous emission where the atom emits a photon to return to the ground (or another excited) state. The wavelengths of these

photons are determined by the electronic structure of the emitting atom or ion. For neutral and singly ionized elements, these photons are most often in the visible (400 - 800 nm, $\sim$1 - 10 eV) and ultraviolet ($\sim$ 10 - 400 nm, 10 - 100 eV). For highly ionized species, the remaining electrons are close to the nucleus, and most emission lines shift quickly into the x-ray regime (0.01 - 10 nm, $10^2 - 10^5$ eV).

Charge exchange (CX), sometimes referred to as charge transfer or electron capture, involves the transfer of an electron from a 'target' species (B) onto an ion 'projectile' (A). In some unique cases, this process is adiabatic and produces no photons. For multicharged ($q > 1$) projectiles, this process transfers an electron into an excited state of the ion which then decays to the ground state via a photon cascade:

$$A^{q+} + B \rightarrow A^{*(q-j)+} + B^j \rightarrow A^{(q-j)+} + B^j + \gamma \tag{1.3}$$
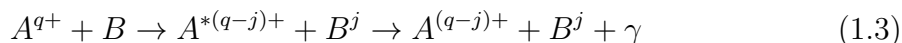
For highly charged ions, this photon cascade is primarily in the x-ray region. While most CX involves the transfer of one electron ($j = 1$), it is also possible for multiple electrons to transfer in a single collision. The likelihood of these processes occurring depends on a number of factors. In most cases there exists a dependence on not only the species A and B, but also the relative kinetic energy of the collision (E). The subsequent photon emission also depends on this collision energy and, more importantly, the electronic structure of the ion and neutral involved in the collision.

Collision processes, e.g. CX, are characterized by a *cross section*, denoted σ, which is interpreted as the probability for a given process to occur in a collision. The cross section has units of area, and for atomic processes is usually written in cm^2 or square Bohr radii (a_o^2). For two hard spheres of radius r colliding, the cross section is simply related to the size of the target particles, $\sigma = \pi(r_A + r_B)^2$. However, for atoms and electrons which behave quantum mechanically the resulting cross sections

may exhibit both an energy and an angular dependence. Typically, laboratory measurements of these cross sections are *total* cross sections where the measured cross section is some weighted sum over all the possible reaction channels for a particular process. For CX with multicharged ions, the number of capture channels may be very large, and the resulting decay pathways may have vastly different cross sections and photon yields. A good example are the calculations for electron capture of Ne^{9+}-H_2O collisions in Ref. [2]. As can be expected from Eq. 1.3, the large number of possible collision energies, targets, and projectiles leads to a high number of measurable cross sections. To date, many of the combinations of (A, E, B) have gone unstudied.

While interesting in their own right, laboratory measurements of these cross sections can be motivated by the data needs of emerging niches in astrophysics. Following the initial proposal of CX between highly charged solar wind ions and outgassed cometary neutrals as the primary ($> 99\%$) source of cometary x-rays by T. Cravens [3], comets are now realized as a "natural laboratory" in which to study the solar wind [4]. Studies continue to contribute to the scope of atomic data which aids interpretation of cometary CX emission, including expanding the ions considered in models of CX emission, e.g. [5], measuring total (absolute) charge exchange cross sections, e.g. [6], or providing new measurements of CX line-ratios for diagnostics purposes [2]. A complete review of cometary CX history (up to 2010) is available in Ref. [4]. However, it must be stated that CX emission from highly charged ions is not limited to comets or our solar system; the process may occur in any environment where hot (i.e. ionized) particles encounter neutrals, including exotic contexts such as laboratory fusion plasmas [7], supernova remnants [8], planetary atmospheres [9], and galaxy clusters [10].

The wide range of ions and neutrals in these environments implies the need for many combinations of (A, B). For example, observations of solar wind interac-

tions reveal contributions from a large number of multi- to highly-charged ions and neutrals [2, 11, 12]. In fusion studies, the cross section needs center around impurity ions (O, C, etc.) or species ablated from the walls (W, Mo, etc.) interacting with atomic hydrogen or other gases [13, 14]. Even for singly charged ions, the data needs are varied. Some unique cases such as Hall Effect Thrusters [15] require a single cross section, whereas other applications such as Thermospheric General Circulation Model [16] used in atmospheric sciences (now known as the Thermosphere-Ionosphere Electrodynamics General Circulation Model [17]), require an exceedingly large number of cross sections.

For applications where large numbers of cross sections are required but not necessarily to high precision, general trends or semi-empirical calculations may be used to guide theoretical calculations or estimate the necessary cross sections. To this end, charge exchange is typically broken into two separate categories, and these categories can be further divided into CX with singly charged ions and CX with multi- to highly-charged ions. With singly charged ions, the two categories of CX are called *symmetric* and *asymmetric* charge exchange.

Figure 1.1, reprinted from Ref. [18], shows the typical energy dependence of these two processes. Symmetric charge exchange occurs when the target and projectile are the same species, i.e. $A = B$, and the energy dependence mimics the structure of the H^+-H reaction in Fig. 1.1. For singly charged ions, symmetric reactions are resonant and the cross section has large values ($\sigma_{cx} \geq 10^{-15}$ cm^2), particularly at low energies. These cross sections decrease monotonically with E and the energy dependence, but not necessarily the magnitude, of the cross section is well described by theoretical calculations. O. Firsov carried out the first such calculation for hydrogen collisions [19], and Rapp and Francis [20] expanded the calculation method to other systems with valence s electrons. Later, Hodgkinson and Briggs developed
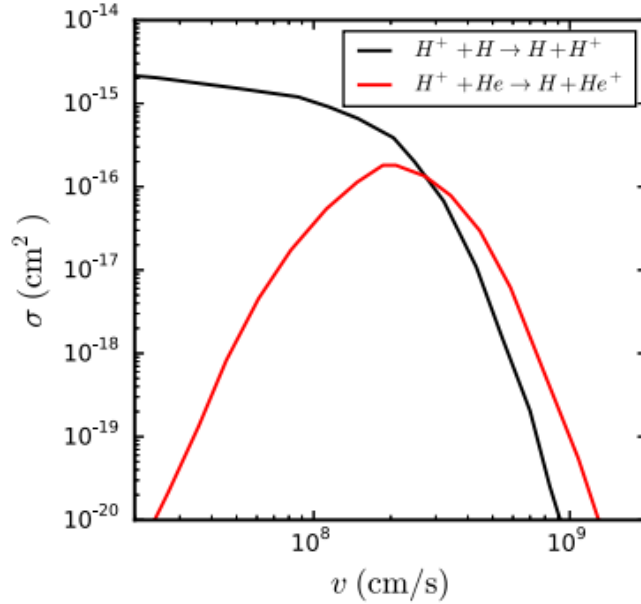
Figure 1.1 Reprint from Friedman & DuCharme [18]. Representative energy dependence of symmetric (e.g. H$^+$-H) and asymmetric (e.g. H$^+$-He) charge exchange.

an approach similar to Rapp and Francis and expanded the calculations to consider non-s electrons [21]. However, discrepancies still remain as to the magnitude of the cross sections and the validity of these approaches across a large energy range.

The second case, *asymmetric* CX, occurs when the projectile and neutral are different species. For singly charged ions, the asymmetric CX reaction may be written

$$A^+ + B \rightarrow A + B^+ + \Delta E \qquad (1.4)$$

where ΔE, called the *energy defect*, is the change of internal energy. For singly charged ions, ΔE is most often considered as the difference in ionization potentials, I_A - I_B. A representation of the energy dependence for asymmetric CX is shown by the H$^+$-He reaction in Fig. 1.1. This energy dependence may be discussed in terms of the energy defect. When ΔE is large, the cross section mimics the single-peaked structure shown by the H$^+$-He reaction in Fig. 1.1. For most asymmetric reactions, the cross

6

section rises to a maximum and then decays toward higher energies. In some cases, asymmetric reactions may have very small energy defects, and these 'accidentally resonant' reactions (e.g. $H^+ + O \rightarrow H + O^+$, $\Delta E \sim 0$) have an energy dependence similar to the symmetric case and the cross sections are generally large for most collision energies [22]. With $\Delta E = 0$, the energy dependence follows exactly as the symmetric case discussed previously. However, when the target B is a molecule, the large number of electronic or vibrational states, each with it's own ΔE, contributes to the capture process and may produce a complicated energy dependence (see Ref. [22] and the compiled data therein).

Recently, Friedman and DuCharme [18] compiled over 100 cross sections and generated a semi-empirical expression for σ_{cx} as a function of the ionization potentials and atomic numbers of the ion and neutral. This scaling law predicts cross sections for both symmetric and asymmetric reactions at velocities between $10^7 - 10^9$ cm/s within a factor of 2 of experimental data on average. This scaling law was produced from a compilation of 59 reactions with singly charged ions, 25 reactions with doubly charged ions, and 25 reactions involving charge states as high as $q = 8+$. However, the highly-charged ion CX cross sections utilized by Friedman and DuCharme were for H, H_2, and He targets, and the application for targets outside these species has not been determined.

For multi- to highly-charged ions, the *total* cross sections are typically large in magnitude ($\sigma_{CX} \geq 10^{-15}$ cm^2) and exhibit a variety of energy dependencies. For example, collisions between atomic hydrogen and fully-stripped boron (B^{5+}) or oxygen (O^{8+}) show a peak structure similar to the asymmetric case of singly charged ions [23]. However, collisions between atomic H and fully stripped carbon (C^{6+}), nitrogen (N^{7+}), neon (Ne^{10+}) and argon (Ar^{18+}) resemble the monotonic decrease seen in singly charged symmetric CX [23, 24]. In general, the magnitude of the total

cross section is largely independent of the projectile and depends solely on the initial charge state [25]. Depending on the charge states of interest, the cross section may scale linearly with charge state q [26] or the charge state to some power e.g. q^α [25].

In addition to the energy dependence of the total cross section, the cross sections for individual capture channels exhibit their own energy dependence. Both the distribution of n states (e.g. $n = 4, 5, 6, ...$) populated by CX (see [2]) and the l distribution within the n shells [27] vary with collision energy. Figure 1.2 shows these dependencies in the (n, l)-resolved cross sections for C^{5+} colliding with atomic hydrogen as calculated by Nolte *et al.* [28]. Several data needs related to these emission cross sections are discussed in Cumbee *et al.* [29]. Multi-electron transfer is often left out of spectral models due to a lack of experimental data for benchmarking. The contribution of highly charged ions, e.g. Fe^{16+}, is unknown due to unavailable atomic data but is expected to explain features of CX spectra [29]. If the energy dependence of the cross section for capture into individual states is known, then line ratios can provide a diagnostic of the energy (and thus the temperature) of the region producing the emission [30]. To summarize, studies of solar wind CX at present are primarily in need of experimental measurements of velocity-dependent line ratios for common solar wind ions such as Fe^{q+} or Mg^{q+}; for a recent example of a diagnostic line ratio measurement, see Ref. [31]. Interestingly, the need for velocity-dependent line ratios and cross sections is not limited to just highly-charged ions. For example, collisions involving simple ions (He^{2+}, H^+) and water molecules (H_2O) are of increasing interest for cometary studies [32].

To measure these photon yields and line ratios, a gas jet is often employed in a crossed-beam experiment (see Chapter 3). In the beam overlap region, the highly charged ions capture electrons from particles in the neutral beam, and the observed x-ray spectrum can be used to calculate the relevant atomic data. However, such ex-
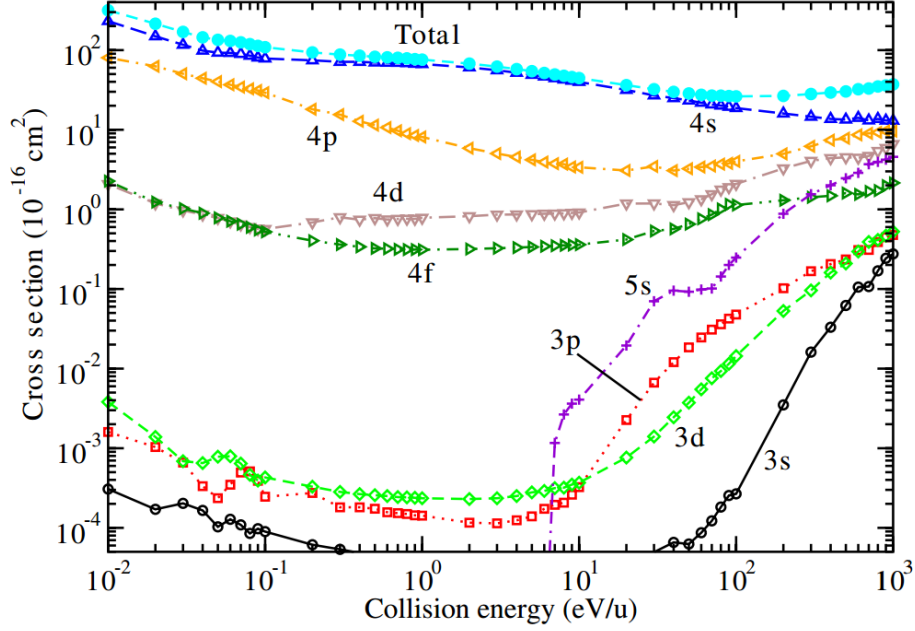
Figure 1.2 Reprint from Nolte *et al.* (Ref. [28]). Energy dependence of (n, l)-resolved charge exchange cross sections for initial capture states following CX from C^{5+} colliding with atomic H.

periments typically produce *relative* cross sections. In most cases, the spatial extent of the neutral jet is poorly quantified and placing the relative emission cross sections onto an absolute scale requires an accurate measurement of the total, absolute cross section. These total cross sections are typically measured in a *gas cell*, in which the neutral density is well-defined, and relative measurements from crossed-beam experiments may be placed onto an absolute scale via an appropriately weighted fraction of the total cross section. Further discussion of total cross sections measurements and the development of a gas cell for measuring (total) charge exchange cross sections is discussed in Chapter 2.

As one would expect from such large CX cross sections, experiments with highly charged ions are difficult. Generating large numbers of these ions requires UHV pressures ($P \leq 10^{-10}$ mbar) to limit the charge state loss to interactions with

background gases. Typical ionization potentials of highly charged ions may range from several keV up to many 10s of keV. The coulomb repulsion between the ions scales as q^2, and for many highly charged ions in close proximity the repulsion is significant. The ions, if produced from collisions with an electron beam, must remain in contact with the electrons long enough to reach the higher charge states. After producing significant quantities of these ions, they must be transported to a crossed-beam or other apparatus for further study, which again is affected by the background gas. Additionally, an ion beam extracted from any highly-charged ion source will have multiple charge states of various species contained within the beam. When studying the interactions between a single ion stage and a neutral, for example O^{8+} colliding with CO_2, some charge state selectivity of the extracted ion beam must be available.

These challenges are met with the Electron Beam Ion Trap (EBIT). The EBIT is built upon the Electron Beam Ion Source (EBIS), which was first published on in 1969 [33]. An excellent review of the science behind the source is available in Ref. [34]. Following the success of the EBIS, the EBIT was built in 1988 by Mort Levine and collaborators at Lawrence Livermore National Lab [35]. Today, EBITs are found at universities [36], national research facilities [37], and are even available from specialized commercial vendors [38]. With an EBIT, nearly every charge state of every element is accessible including ions up to fully stripped uranium, U^{92+} [39].

A schematic of the Clemson University Electron Beam Ion Trap (CUEBIT) is shown in Fig. 1.3. Though not all EBITs include the beamline shown in Fig. 1.3, the operation of the machine is similar to other EBIT sources. An EBIT produces ions by successive electron impact ionization of particles, sourced from background gas or gas intentionally injected from an external source, between a set of three drift tubes. Typical electron beam energies in EBITs are few to tens of keV, and electron beam currents are as high as 1 A. In the axial direction (left to right in Fig. 1.3),

10
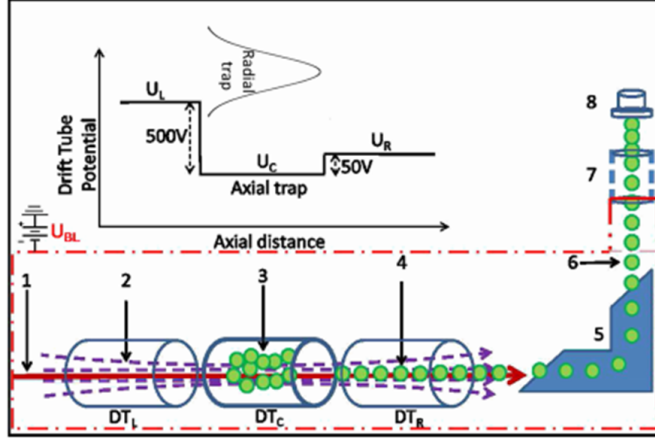
Figure 1.3 Reprint from Ref. [40]: Schematic of the Clemson University EBIT and attached beamline. The electron beam (1), drift tubes (2-4), and charge-to-mass analyzing magnet (5) are shown.

confinement results from the positive bias of the outer two drift tubes with respect to the center drift tube. In the radial direction, the ion cloud is confined by the (negative) space charge of the electron beam. In order to reach the high charge states of interest, the electron beam must have a sufficiently high density to counteract the neutralization due to background gas and provide radial confinement. In CUEBIT, the electron beam is compressed to high density (100 mA/$\pi(200\mu m^2) \sim 800$ kA/m^2) by a 6 T superconducting magnet held at 4 K by a closed-cycle cryo-compressor.

CUEBIT is equipped with two 2-3/4" CF viewports with line of sight through the trap region, and spectroscopy of trapped ions is possible. Alternatively, the ions may be extracted from the trap and collimated into a beam. By lowering the voltage of the right drift tube slightly (DT_R in Fig. 1.3), the more energetic ions may 'leak' from the trap. This 'leaky' mode allows for a continuous beam of ions to escape the trap. Alternatively, the voltage on DT_R may be shut off, and the entirety of the trapped ions may be pulsed from the trap region. The ions are guided to the analyzing magnet, (5) in Fig. 1.3, and ions of a particular charge-to-mass ratio exiting

the analyzing magnet may be carefully selected by a tunable B-field. After leaving the magnet, the beam consists of a single q/m ratio that can be guided into different apparatuses downstream. However, this ratio may be degenerate with charge states of highly charged ions produced from the background gas, and careful selection of the source gases and knowledge of the background gas are beneficial.

At the end of the CUEBIT beamline, a Cold Target Ion Momentum Spectroscopy (COLTRIMS) experiment is being constructed to study CX between solar wind ions (e.g. Ne^{10+}, Mg^{12+},...) and H_2 and He. Historically the COLTRIMS technique has been utilized to study problems related to ionization, electron impact ionization, ion-atom collisions, and even molecular fragmentation. A thorough review of this topic by Ullrich *et al.* (2003) is available in Ref. [41]. COLTRIMS is particularly well-suited for studies of solar wind CX. Using several particle and photon detectors, COLTRIMS produces "triply-differential cross sections," that is, the measurements yield information on the 3-dimensional momentum transfer in the collisions. Our "triply-differential cross sections" collect the information of the collision dynamics provided by the detection of the primary ions, secondary ions, and post-collision photons.

A schematic of the proposed COLTRIMS experiment is shown in Fig. 1.4. In COLTRIMS, a beam of a single charge state is crossed with a cold, neutral gas jet oriented perpendicular to the ion beam. In the interaction region, the ions experience a change in *longitudinal* momentum (i.e. along the direction of the incoming ion beam) arising from charge exchange between the gas jet and ion beam. Downstream from these interactions, applying a voltage perpendicular to the direction of the ion beam separates the ions with the initial charge state q from the charge states $q-1$, $q-2$, ... produced via CX. The energy of the ion beam is calculated from the potentials of the drift tubes within the EBIT, and the change in longitudinal momenta is then
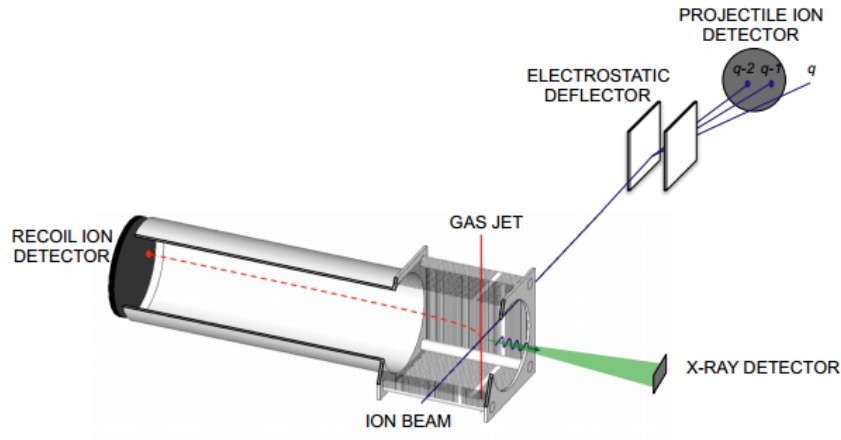
Figure 1.4 Schematic of the proposed COLTRIMS experiment [42]. Reprinted with the permission of Dr. Mike Fogle [42].

calculated from the geometry of the deflection scheme and the measured positions of the post-CX ions of charge $q - 1$, $q - 2$, ... on a position-sensitive detector.

A similar procedure may be carried out for the slow ions. In the interaction region, a set of electrodes envelop the ion-jet overlap region. With a low voltage pulse, the slow ions produced via CX are accelerated towards a second, position-sensitive detector. These slow ions have near zero velocity in the perpendicular direction (i.e. parallel to the ion beam) due to the cold temperature of the gas jet. From the geometry and voltage of the deflection scheme, the change in momenta of the slow ions is calculated from the positions and time-of-flight. The change in momenta of the ion beam and the slow ions yields the Q value, or momentum transfer, of the individual collisions. The resolution of the Q value is set by the transverse temperature of the gas jet particles, and with a sufficiently low temperature ($\sim$mK), captures into individual n states of the ion are resolvable.

The last component of the CX puzzle is the l distribution into which electrons are captured in each n shell. This information is provided by an x-ray spectrometer

13

aimed at the interaction region. From the observed x-ray spectra, the l distribution of the n states populated by CX is measured, and the velocity dependence of the (n, l) cross sections may be found by simply varying the primary beam energy. Using this technique with CUEBIT, triply-differential cross sections may be measured for solar wind ions of interest.

To summarize, CX emission may be produced in any environment in which ions encounter a neutral gas, e.g. solar wind ions interacting with cometary atmospheres. To understand the photon emission from this process, theoretical models are employed to fit the observed spectra. However, these theoretical models are guided by laboratory measurements of energy-dependent emission cross sections, and producing the required atomic data is an ongoing effort. Measuring the photon yields in the laboratory is typically carried out with a gas jet in a crossed-beam experiment, and placing these measurements onto an absolute scale requires normalization to total, absolute cross sections as measured in e.g. a gas cell. Development of neutral jets and gas cells for these purposes is discussed in Chapters 2 and 3.

1.2   Atomic Data for Spectroscopy in Astrophysics

Understanding the observed spectra of astrophysical sources requires accurate laboratory measurements of line positions. In the case of solar wind ions, the positions of emission lines are known but the velocity dependence and (n, l) distribution of the CX photon spectrum is an open question [27, 30, 32]. One of the most commonly used databases for such line positions is the National Institute of Standards and Technology (NIST) Atomic Spectra Database (ASD). In Fig. 1.5, the availability of line and level information in the NIST ASD is shown [43]. Starting at the top left is neutral hydrogen. As one moves down and to the right, the atomic number and
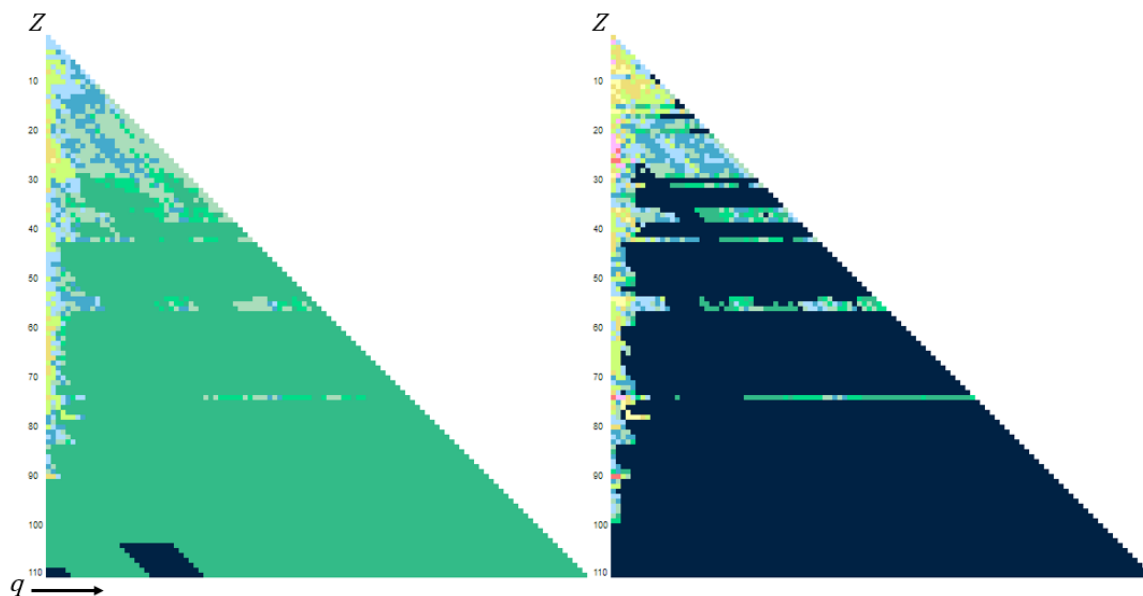
Figure 1.5 Reprint from the NIST Atomic Spectra Database [43]. *(Left)* Level holdings as a function of atomic number Z and charge q. *(Right)* Line holdings as a function of atomic number and charge state. The color coding for both the lines and levels scales from 0 holdings (dark blue) to many holdings (red).

charge state increase respectively. The color coding indicates the number of levels and lines from 0 (dark blue) to many (red). As shown in the NIST holdings, many of the high charge states of the low-Z elements ($Z \leq 26$) and most of the elements beyond iron are lacking atomic data.

The NIST holdings reflect the data needs of the wider physics community. Below iron, most elements are produced through stellar nucleosynthesis and the observed abundances are well understood [44]. Initially, the drive for accurate atomic data, including emission lines, energy levels, and oscillator strengths, focused on these low-Z elements that were most abundant and commonly observed in stellar environments. Therefore it is not unexpected that the data for these elements is relatively complete. In more recent years, the highly charged versions of these elements have received attention due to their applications in fundamental studies of quantum electrodynamics

15

(QED), developing relativistic atomic structure codes, atomic clocks, and time variations of fundamental constants; for a more complete discussion of these applications, see the review article by Kozlov *et al.* [45].

Beyond iron, emission from heavy elements such as gold, osmium, and various lanthanides have also been observed in a number of stars, including the Sun and chemically peculiar stars which have unusual abundances of these heavy elements. For more information on these peculiar stars, see Refs. [46, 47, 48, 49, 50] and the references therein. Many of these "heavy elements" ($Z > 54$) are produced by rapid neutron capture, also known as the rapid or r-process, which requires successive neutron captures over timescales much shorter than that of beta decay. The physical conditions for this process are expected to be found in either neutron star mergers or other comparably explosive events such as core-collapse supernovae though the exact sites of this process have not been confirmed [51]. To date, the available data for high-Z elements has been adequate for studies of stellar atmospheres, but as shown in Fig. 1.5, many of the elements and charge states have not received great attention.

In August of 2017, the LIGO & Virgo collaborations announced the successful detection of the gravitational wave signal from two merging neutron stars known as GW170817 [52]. No information on the exact composition of the post-merger ejecta is gleaned from the gravitational wave signal. However, electromagnetic followups of this event, for example the x-ray and optical observations of Margutti *et al.* [53] and Coulter *et al.* [54], offer new insight into these events. In the transients, the observed spectra contain no sharp features that would directly indicate r-process elements are present, but the color evolution of the ejected material is explained by radioactive heating from 0.01 - 0.05 $M_\odot$ of r-process elements [52]. Most recently, Watson *et al.* [55] have identified emission from freshly-synthesized Sr in the ejecta of GW170817 [55], and studies of the ejecta abundances are ongoing.

Extracting r-process yields from the electromagnetic transients is complicated by the large volume of atomic data, or lack thereof, for these heavy nuclei. Following the merger, the opacity of the rapidly cooling ejecta is expected to result primarily from the presence of lanthanides [56]. The presence of relatively few lanthanide elements can have a profound effect on the opacity of the ejecta as the open f-shell allows for a large number of bound-bound transitions. By carrying out the complicated opacity calculations and using them to interpret the observed spectra, some information may be inferred about the abundances of individual r-process elements.

As a qualitative example of this opacity problem, Fig. 1.6 shows the Planck mean opacity calculated by Kasen *et al.* for Nd, Fe, and Si [56]. Compared to iron group elements, the opacities of the lanthanides are of order 10 - 100 times greater. Reducing the mass fraction of a single lanthanide component (e.g. Nd in Kasen's calculations) by a factor of 100 reduces the opacity contribution by only a factor of 5, and many lanthanides may dominate the opacity with mass fractions as low as 10^{-4} [56]. One would expect the largest contribution to the opacity from elements with the most complex structure, e.g. Eu (Z $= 63$, ground configuration $4f^76s^2$) or Gd (Z $= 64$, ground configuration $4f^75d6s^2$) [56]. However, the threshold for excitation in these species is higher than both the neutral and low excited states of the lighter lanthanide ions and thus contribute less to the opacity at the ~eV temperatures in the ejecta [56, 57].

In reality, calculating a meaningful opacity for each element and ion stage requires a large input of energy levels, transitions, and oscillator strengths. To date, the necessary atomic data is calculated with atomic structure codes, particularly AUTOSTRUCTURE [57]. For most elements heavier than iron the available atomic data to benchmark these calculations (i.e. lines, levels, and transition A values) are not complete or in many cases have not been measured. The effect of accurate
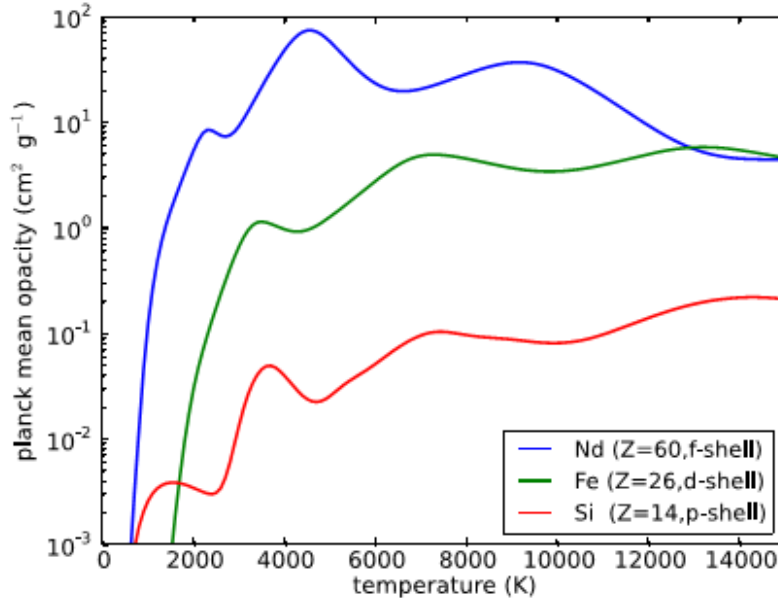
Figure 1.6 Reprint from Ref. [56]. Planck mean opacities calculated by Kasen *et al.* for Nd (lanthanide), Fe (iron-group), and Si (low-Z). The Nd opacity is from an AUTOSTRUCTURE model while the Fe and Si opacities use known line data [56].

(experimental) atomic data on the opacity calculations and the resulting r-process abundances in NSM ejecta has yet to be determined. Even in the absence of appropriate benchmarks, structure calculations for such heavy elements are complicated by core-valence coupling, core polarization, significant configuration interaction, and relativistic effects [58]. As discussed in Ref. [59], the atomic structure codes currently available are not sufficient for accurately reproducing the spectra of heavy elements.

As mentioned previously, the lanthanides and other heavy elements are also important for studies of chemically peculiar stars. These rare earth elements are primarily detected in the singly ionized form, though doubly ionized species have also been observed (e.g. [60]). As discussed in the review by Sneden *et al.* [49], the observation (or lack thereof) of heavy elements in both chemically peculiar and metal-poor stars helps drive improvement of r-process nucleosynthesis models. However the lack of atomic data limits the detection of trans-iron or even lanthanide elements to

only a handful of emission lines, and the following abundance calculations are highly sensitive to both the accuracy and quality of the atomic data available [49].

To summarize, there is a clear drive for experimentalists to study the spectra of these astrophysically relevant species. New experimental measurements of the lines and levels of these high-Z elements would be beneficial for interpretations of future NSM spectra, r-process abundance studies of stellar atmospheres, and as a useful benchmark for atomic structure codes.

1.3   Outline

This dissertation was aimed at developing, using, and improving experimental methods for measuring properties of atoms and ions relevant to the astrophysics community. The results in this work were published in several articles [61, 62, 63]. This dissertation may be summarized as follows.

In Chapter 2, the design, construction, and testing of a gas cell for measuring charge exchange cross sections is discussed. The cell was benchmarked by measuring the total charge exchange cross section for the well-studied reaction $Ar^+ + Ar \rightarrow Ar + Ar^+$ [61]. Using this design, the cross sections for the symmetric reactions with singly charged ions $A^+ + A \rightarrow A + A^+$ (A = He, Ne, Ar, Kr) were measured and compared to the available literature [62]. Using the same apparatus and technique, the cross sections for noble gas ions interacting with molecular nitrogen were measured and compared to the available literature [63]. Lastly, a second gas cell was designed, constructed, and tested to improve upon the disadvantages of the first design. The new design is featured alongside the molecular nitrogen measurements in Ref. [63].

In Chapter 3, the design, construction, and testing of two gas jet sources is discussed. The first design is small and fits inside standard 2-3/4" CF vacuum

components, and the jet conditions (pressure and temperature) are well described by a simple model. The neutral beam produced during operation is sufficient for injecting gaseous targets (noble gases, diatomics, or volatile organic compounds) into an EBIT or similar ion source. The second gas jet design is presented for incorporation into the Cold Target Ion Momentum Spectroscopy (COLTRIMS) experiment planned at CUEBIT. The COLTRIMS experiment will measure relative nl-resolved charge exchange cross sections of multi-charged ion-neutral collisions relevant to solar wind studies.

In Chapter 4, we present a new study of the emission spectra of neutral and ionized gold. Emission spectra of gold were collected from plasma discharges at the Compact Toroidal Hybrid at Auburn University. The numerous codes developed for the data analysis are discussed, and line and level lists are reported and discussed for Au I and Au II.

Lastly, in Chapter 5 the work is summarized and the outlook for future experiments stemming from this work is presented. SOLIDWORKS designs and Python codes used for the analyses in Chapters 3 and 4 are provided in Appendices A - D.

Chapter 2

Measuring Charge Exchange Cross Sections with Gas Cells

2.1 Introduction

Charge exchange has been observed in a variety of astrophysical environments. This process,

$$A^{q+} + B \rightarrow A^{*(q-j)+} + B^j \rightarrow A^{(q-j)+} + B^j + \gamma \qquad (2.1)$$
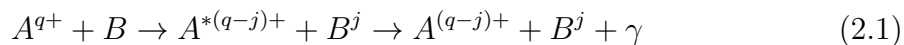
is typically broken up into two categories: asymmetric ($A \neq B$) and symmetric ($A = B$) charge exchange. In astrophysical contexts, the interactions most often involve with simple neutral molecules such as H, H_2, or He. In some niche contexts such as cometary atmospheres, the list of neutrals may expand to include more complicated molecules such as N_2, CO_2, or CO. Compared to thermal emission, the photons produced by Eq. 2.1 are characteristic and unique to the species A. Therefore, the emission lines may be used as diagnostics of the local environment and may provide

information on the abundances, densities, temperatures, and velocities of the species producing the CX spectrum.

The large number of possible ions, neutrals, and energies that could contribute to astrophysical spectra highlights the need for laboratory studies of this process. To understand the source of charge exchange emission, models require absolute, total charge exchange cross sections for each combination of A and B. Ideally, these cross sections would be nl resolved, i.e. the cross section for each reaction channel (initial and final state) is available on an absolute scale.

In the lab, measuring absolute charge exchange cross sections involves the interaction of an ion beam with a gas target region. In this context, we may derive an expression for the charge exchange cross section by drawing parallels to the derivation of the attenuation of a monochromatic beam of light traveling through a medium; see Ref. [64]. Consider an ion beam traveling in the z direction. We assume that the only source of current loss is charge exchange and equate the rate of neutralization $\frac{dI}{dz}$ to the current loss via charge exchange

$$\frac{dI}{dz} = -In\sigma_{cx} \tag{2.2}$$

where n is the neutral target density and σ_{cx} is the charge exchange cross section at energy E. Here we consider that the ion beam is monoenergetic. Rearranging we have

$$\frac{dI}{I} = -n\sigma_{cx}dz \tag{2.3}$$

Assuming that the neutral density is a constant over the length of our interaction region, i.e. $\frac{dn}{dz} = 0$, integration over the length of the gaseous region from $z = 0$

to $z = L$ yields a CX analog of the Lambert-Beer law [64]

$$I(L) = I_o e^{-Ln\sigma_{cx}}. \tag{2.4}$$

The exponential may be expanded by the Taylor series $e^{-x} = \sum_{n=0}^{\infty} \frac{(-x)^n}{n!}$. We assume the target gas behaves ideally, i.e. $PV = Nk_bT$. For 'thin' targets, $PL\sigma_{cx} \gg k_bT$, the expansion may be truncated to $e^{-x} \approx (1-x)$. Thus Eq. 2.4 simplifies to:

$$I(L) = I_o \left(1 - \frac{LP\sigma_{cx}}{k_bT} \right). \tag{2.5}$$

Solving for σ_{cx}, we arrive at the charge exchange cross section written in terms of an initial (pre-gas) current, a final (post-gas) current, the pressure of the neutral gas in the interaction region, and the path length over which the ion traveled in the presence of the neutral gas:

$$\sigma_{cx} = \frac{k_bT}{PL} \left(\frac{I_o - I}{I_o} \right) \tag{2.6}$$

As shown by Eq. 2.6, charge exchange cross sections may be calculated from measurements of ion beam currents with and without gas in an interaction region and the spatial extent (L), temperature (T), and pressure (P) in that region. For multicharged ions, charge exchange cross sections are of order 10^{-15} cm^2, and beam currents from EBIT or EBIS-type ion sources are typically below 1 nA. For such low currents, the target thickness PL must be sufficiently large to produce a measurable decrease in the ion beam current. For ultra-high vacuum pressures typical of multicharged ion beamlines (10^{-9} mbar), a 10% decrease in beam current due to charge exchange would require the path length L be over 40 *kilometers*. Such long

path lengths are simply unrealistic. If we consider a smaller region of higher pressure, $P \sim 10^{-4}$ mbar, we find the required path length is on the order of several dozen cm. Additionally, by tuning the beam into a small region of high pressure, the ion beam alignment may be carried out without gas in the interaction region and the effect of beam divergence within the interaction region is minimized. With such a high pressure, the apertures of the apparatus must be small enough to limit the effect of gas leakage into the ion beamline. These conditions (a short, high pressure environment) are provided by a 'gas cell' apparatus.

In the following, we discuss the design, construction, and testing of two such gas cells for measuring charge exchange cross sections. The first design, titled the 'Manipulator Gas Cell' (MGC) was optimized for measuring charge exchange cross sections with multicharged ions and incorporates a small, high pressure interaction region. In Secions 2.2 - 2.4, the development of the MGC and subsequent experimental measurements of the absolute charge exchange cross sections for the symmetric reactions $A^+ + A \rightarrow A + A^+$ (A = He, Ne, Ar, Kr) and the asymmetric ion-molecule reactions $A^+ + N_2 \rightarrow A$ (A = He, Ne, Ar, Kr) are presented.

In Sec. 2.5, we discuss the design and development of a second gas cell, titled the 'Floating Gas Cell', which builds upon the design of the MGC and explores improvements on the traditional gas cell approach.

2.2 Design and Benchmarking of a Manipulator-Mounted Gas Cell

The first gas cell design is referred to as the Manipulator Gas Cell (MGC), and a schematic of this design is shown in Fig. 2.1. The cell itself is machined from
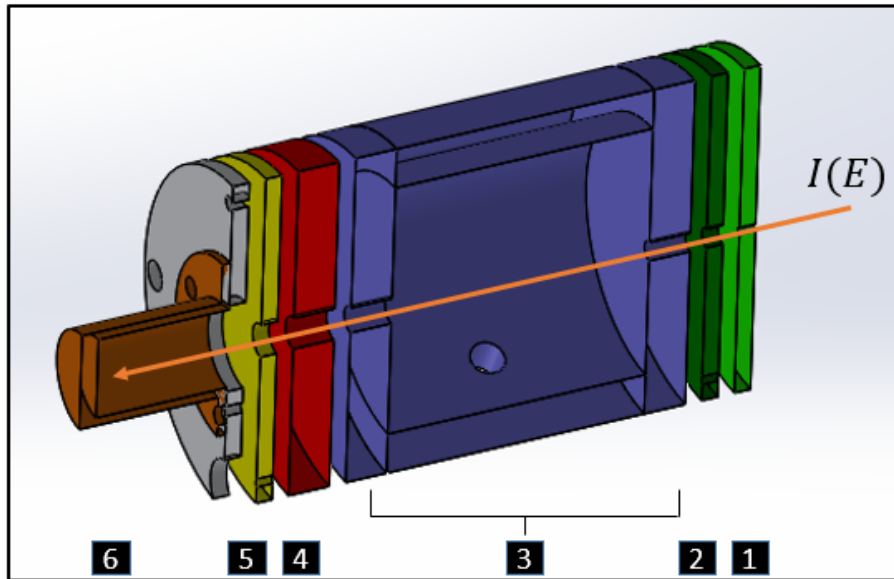
Figure 2.1 SOLIDWORKS schematic of the Manipulator Gas Cell. Electrical components are shown in the order they are traversed by the ion beam: 1) faceplate, 2) skimmer, 3) cell body, 4) retarding field analyzer, 5) suppression electrode, and 6) faraday cup.

a cylinder of non-magnetic stainless steel (SS 316) with an inner diameter of 4.0 cm, length 4.0 cm, and an outer diameter of 5.26 cm. All components, save for the faraday cup, are machined from non-magnetic stainless steel (SS 316) with an outer diameter of 5.26 cm. The electrical components of the cell are labeled in the order they are traversed by an ion beam: 1) faceplate (bright green), 2) skimmer (dark green), 3) front endcap, cell body, and back endcap (dark blue), 4) retarding field analyzer (RFA, red), 5) suppression electrode (yellow), and 6) faraday cup with mounting plate (orange and grey respectively).

The components of the gas cell are electrically isolated from each other by MACOR top-hat washers with an outer diameter of 0.29", wall thickness, 0.04", and heights such that 0.1" rests inside the holes of each plate, and the lip ensures 0.1" separation between adjacent plates. Electrical connections are made by kapton-
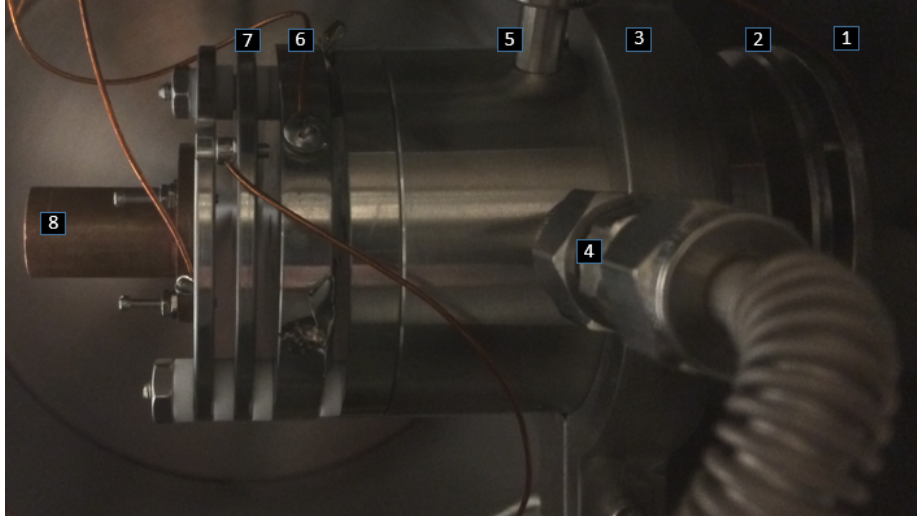
Figure 2.2 A photograph of the Manipulator Gas Cell, adapted from Ref. [62]. The components are labeled as following: 1) faceplate, 2) skimmer, 3) circular mounting bracket, 4) pressure gauge tubing, 5) gas injection tubing and cell body, 6) retarding field analyzer, 7) suppression electrode, and 8) faraday cup. The electrical connections to the faraday cup, suppression electrode, and retarding field analyzer are also shown.

coated wires under the heads of screws in either the face of each component or, where possible, on the outer edge of the component. The faceplate measures 2.5 mm thick with a central aperture of 1 mm. Between the faceplate and cell body a second, grounded skimmer (thickness 2.5 mm, aperture 2 mm) was placed. The front endcap and back endcaps of the cell measure 6.3 mm thick with apertures of 3 and 4 mm respectively. At the back of the cell, the retarding field analyzer (RFA, thickness 6.3 mm, aperture 6 mm) and suppression electrode (thickness 2.5 mm, aperture 6 mm) rest between the faraday cup and cell body. The faraday cup (FC) is machined from oxygen-free high-purity copper (OFHC) with an internal diameter of 6.3 mm and a length of 20 mm (aspect ratio 0.3).

A photograph of the assembled cell is shown in Fig. 2.2. The components of the gas cell are mounted on two #5-40 rods threaded into the cell body at the front and rear of the cell. The electrical components are held in place by nuts at the end
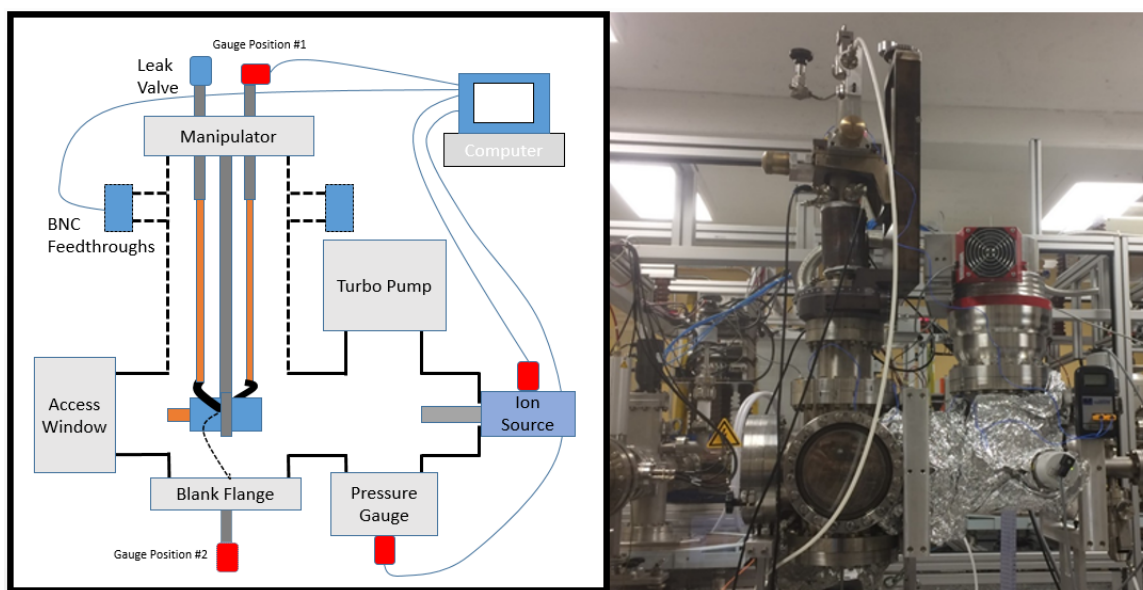
Figure 2.3 *(Left)* Schematic of the gas cell chamber showing the layout of the cell, manipulator, and ion source. *(Right)* Photograph of the gas cell chamber in the same orientation as the schematic.

of each #5-40 rod. The assembled cell is mounted on an ultra-high vacuum (UHV) manipulator by a circular bracket around the cell body which connects to a long stainless steel rod threaded into the 3.33 in. CF flange at the top of the manipulator. The manipulator itself is capable of translation in x, y, and z and 360° rotation for alignment with various ion sources, including a singly-charged gas ion source and the CUEBIT. The manipulator is mounted on a vacuum chamber consisting of two 8 inch CF crosses. A schematic of this chamber is shown alongside a photograph of the setup in Fig. 2.3.

At the top of the manipulator, two hollow 1/4" stainless steel rods were placed through the 3.33" CF and welded in place. On the atmosphere side, a manually operated UHV leak valve and a full-range cold-cathode (CC) gauge (Pfeiffer PKR 251) were attached to the tubing by Swagelok elbows, commercially available CF-to-Swagelok adapters, and two custom aluminum mounts held in place by the screw
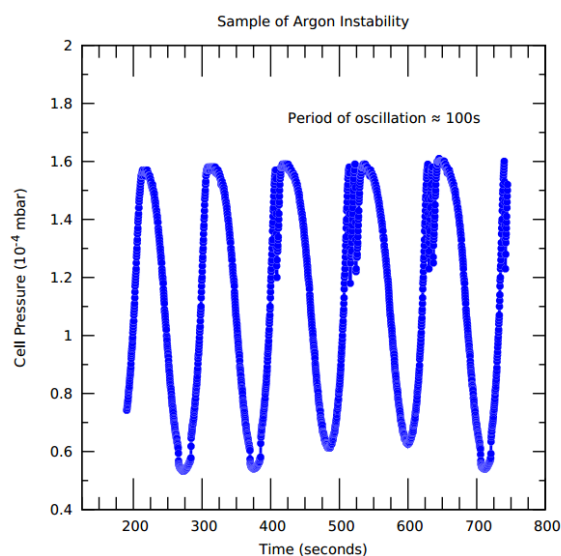
Figure 2.4 Measured cell pressure as a function of time during an argon instability. The oscillation occurs for a fixed position on the leak valve.

heads of the 3.33" flange. On the vacuum side, 14" of OFHC tubing and Swagelok unions connect the steel tubing in the flange to 350 mm long flexible stainless steel tubing. A second set of Swagelok unions connect the flexible tubing to 1/4" steel tubing threaded into the cell body. On one side of the cell the gas is injected by opening the leak valve at the top of the manipulator, and the cell pressure is monitored by the full-range gauge at the end of the second set of tubing.

Cold-cathode (CC) gauges measure gas pressure by ionizing gas inside the gauge and measuring the ion current on the cathode. During initial testing of the cell, an "argon instability" was observed in the readings of the CC gauge measuring the cell pressure. A plot of the measured pressure during this instability in our apparatus in shown in Fig. 2.4. In these CC gauges, the instability arises from sputtering of the gauge walls by the ionized argon. During the discharge, secondary electrons and the ionized argon aid in removing adsorbed gas from the cathode walls which rapidly increases the pressure inside the gauge. At a high enough pressure, the

discharge controller shuts off and the gas is pumped away. Once the pressure is low enough, the discharge re-ignites and the process repeats. The period of oscillation appears to decrease with increasing initial pressure. Following a scrub with fine-grit sandpaper and a typical UHV chemical cleaning, the sputtered metal is removed and the instability is absent for a short time. A more complete discussion of this phenomenon is found in Ref. [65].

Following a change in pressure, the cell gauge takes of order 10 minutes to stabilize, and small adjustments to the pressure are unmeasurable due to the long tubing between the cell body and gauge location. A solution to both this issue and the argon instability was explored via the following. The flange at the bottom of the chamber was replaced with a 8"-to-2-3/4" ConFlat zero-length reducer. On the atmosphere side, a Swagelok-to-CF converter connects this flange to a Pfeiffer Full-Range Bayard-Alpert Gauge (PBR 260) located at "Gauge Position #2" in Fig. 2.3. In vacuum, a Swagelok union connects the flexible stainless tubing from the cell, which is rotated 90° w.r.t the axis of the cell, to stainless steel tubing on the reducing flange at the bottom of the chamber. Lastly, "Gauge Position #1" was fitted with a UHV shutoff valve to aid in venting the chamber during modifications.

The "argon instability" was not observed when using a hot cathode gauge (Pfeiffer PBR 260) in place of the CC gauge as the hot filament prevents gas from adsorbing to the walls of the gauge. This modified setup was used for the majority of the experimental measurements discussed in this chapter. In total, the experimental chamber (Fig. 2.3) contains three pressure gauges: 1) a Pfeiffer Full-Range Cold Cathode (PKR 251) on the ion source, 2) a second PKR 251 gauge on the chamber near the turbo pump, and 3) a hot cathode gauge (PBR 260) connected to the gas cell. All three gauges are calibrated at the manufacturer to measure pressures of pure N_2. When measuring pressures of other gases, the conversion $P_{true} = K \times P_{measured}$

was used where values of K are supplied by the manufacturer for most common gases. All three gauges feed into a Pfeiffer Maxi-Gauge controller which was interfaced to a computer by a RS232 cable. Values are read into LabVIEW by drivers from the manufacturer.

Both the ion source and gas cell require a continuous feed of gas during operation. For experiments using the same gas in both the ion source and gas cell, a single gas bottle was used. The bottle connects to the pump, cell, and ion source by a series of 1/4" push-to-connect T's, valves, and low density polyethylene (LDPE) tubing. A manually operated, push-to-connect shutoff valve was placed in-line with a scroll pump. After evacuation to 2×10^{-2} mbar, the lines were flushed with the gas and re-pumped 3 times. After pumping, the lines are held at 6 PSI above atmosphere to prevent contamination from possible leaks in the push-to-connect fittings. For experiments with different gases for the cell and ion source, each section (ion source, cell) was pumped and flushed independently and isolated from the rest of the gas system by in-line manually operated push-to-connect valves.

The ion source used for this work was an OMICRON ISE 10 sputter ion source. In this source, a thorium oxide coated iridium filament produces up to 10 mA of emission current. The anode is floated +120 V above both the cathode and surrounding 'energy' electrode. During operation, the emitted electrons are accelerated to 120 eV (fixed by the controller), ionize the injected neutral gas, and the resulting ions are pulled from the filament region by an extraction electrode. Finally, a focusing electrode collimates the ions into a beam. For typical operating conditions, $P_{source} = 4 \times 10^{-4}$ mbar, the achievable beam currents are generally proportional to the mass of the gas and the beam energy. For Ar^+ beams above 1 keV, FC currents are of order 10's of nA and FP currents may be as high as 5-6 μA. For Ar^+ below 1 keV, FC currents are on the order of several nA. For 0.2 keV He^+, FC currents are

close to 0.6 nA and FP currents are less than 1 μA.

When measuring cross sections the electrically isolated components of the cell serve several purposes. Both the faceplate and skimmer aid in beam alignment by allowing only the most collimated portion of the beam into the gas cell. As the beam current measured at the faraday cup will be much smaller than the current incident on the front of the cell and the expected current losses are small, it is useful to have a measure of the stability of the ion source. During gas injection, little gas escapes to the chamber, and thus any change in faceplate current will be a result of changing ion source conditions. During an experiment, the faceplate current is monitored in addition to ion source pressure to ensure that changes in FC current are due to charge exchange and not drifts in ion source conditions. The faceplate current is monitored by a Keithley 2010 and a pre-amplifier connected to the computer and interfaced via LabVIEW. The faraday cup current is monitored by a Keithley 485 interfaced to LabVIEW via a GPIB-to-USB adapter. All measured currents and pressures are interfaced in a single LabVIEW code with timestamps.

The front endcap, cell body, and back endcap ensure that the neutral pressure is well-defined within the interaction region. The apertures at the front and rear of the cell (3, 4 mm) limit the gas flow from the cell into the chamber. For the turbo pump used here, lighter gases are pumped less efficiently compared to heavier species such as argon or krypton, and the ratio of cell-to-chamber pressure is of order 750 for He and 1000 for Ar or Kr.

At the rear of the cell, each component plays a key role in measuring cross sections. Immediately behind the rear endcap, a retarding field analyzer (aperture 5 mm) allows for measuring the energy distribution of an ion beam. By increasing the voltage on the RFA, ions in front of the aperture acquire a change in energy of $\Delta E = -|e|V_{RFA}$. By fitting a gaussian profile to the resulting curve of $\frac{dI_{FC}}{dV_{RFA}}$ versus

V_{RFA}, the beam energy selected on the ion source can be confirmed. After the RFA, a suppression electrode at -120 V prevents secondary electrons, produced from ions striking the copper faraday cup, from exiting the cup and providing a false current reading.

With this design a typical measurement of a charge exchange cross section is as follows. Gas is injected into the ion source and allowed to stabilize with the emission current set at the maximum value (10 mA). The gas cell is aligned with the ion beam by adjusting both the translational and rotational positions of the UHV manipulator until the maximum current in the faraday cup is achieved. Starting at 1 keV, the extraction and focusing voltages of the ion source are varied until the maximum beam current, as measured by the FC, is achieived. These voltages are recorded, and the process is repeated for 9-10 evenly spaced energies (0.2 - 1.0 keV, or 1.0 - 5.0 keV). After these values have been optimized, the beam energy is reset to 1 keV, and values of the FC current, $I_o(E)$, are recorded for each set of optimized ion source voltages $(V_{energy}, V_{extract}, V_{focus})$.

The beam energy is again reset to 1 keV. Gas is injected by opening the leak valve until the cell pressure is of order $1 - 2 \times 10^{-4}$ mbar; pressure stability is typically achieved in $\sim$ 5 minutes. Beam currents, $I(E)$, are recorded for each set of optimized ion source voltages, and this process is repeated for a total of four cell pressures between $1 - 8 \times 10^{-4}$ mbar. In total, this process takes 1 - 1.5 hours depending on the number of energies chosen. After the gas is shut off, the system base pressure $(2 \times 10^{-8}$ mbar) returns within 1 - 2 hours. Any measurements where the ion source pressure, and thus the faceplate current, changed significantly between the I_o measurements and gas shut-off were removed from our analysis. For the pressures used here $(P < 10^{-3}$ mbar), the probability of a single collision is low, and thus any ion that has undergone charge exchange is unlikely to undergo a second collision.
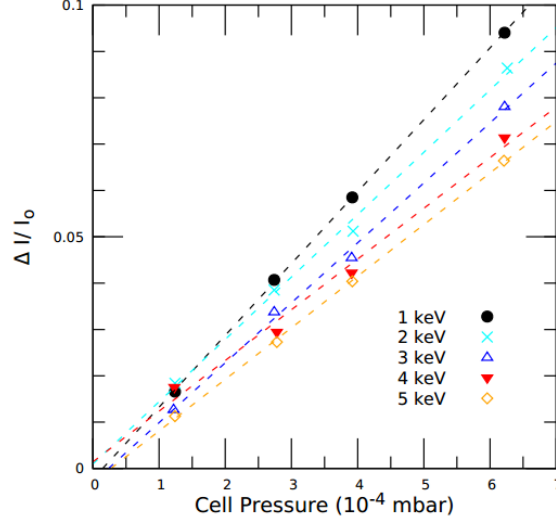
Figure 2.5 A plot of $\frac{I_o(E) - I(E)}{I_o(E)}$ versus cell pressure for beams of Ar^+ passing through neutral argon [62]. Error bars of each $\frac{\Delta I}{I}$ measurement are smaller than the plotted symbols. Pressures are measured with an uncertainty (not shown) of $\pm 15\%$.

Rearranging Eq. 2.6, we find

$$\frac{I_o(E) - I_{gas}(E)}{I_o(E)} = \frac{PL}{k_b T}\sigma_{cx} \tag{2.7}$$

In plots of $\frac{I_o(E) - I_{gas}(E)}{I_o(E)}$ versus pressure, we observe a strictly linear relationship between the current loss and pressure which is indicative of the single collision regime. A sample of current loss data for 1 - 5 keV beams of Ar^+ incident on neutral Ar is shown in Fig. 2.5. From a fit to the current loss versus pressure plot, the cross section is then simply calculated from the slope m of the fit: $\sigma_{cx} = \frac{mk_b T}{L}$.

The cross section is calculated from measurements of the pre-gas currents at each energy, $I_o(E)$, the with-gas currents $I(E)$, and the target pressures. The temperature of the gas, T, is set by the ambient room temperature (298 K). The path length, L, is set by the geometric length of the cell. However, gas leaking out of the apertures adds to the path length. A calculation of this contribution was

carried out by Ref. [66], and other works with thin-walled gas cells have found that the contribution from leaking gas is best handled by adding the sum of the aperture radii [6]. We adopt the same convention as Greenwood *et al.* [6] for thicker-walled cells and consider the total path length as the sum of the endcap lengths (12.6 cm) and length of the cell (40 mm) for a total path length of 52.6 mm.

Lastly, we estimate the systematic uncertainty of our cross section measurements by adding in quadrature the following uncertainties: uncertainty in the pressure (15%, provided by Pfeiffer Vacuum), path length (7%, sum of entrance and exit radii divided by the total path length), temperature (0.5%, 1K/298 K), a 2% uncertainty in I_o from charge exchange with background gas in the chamber, a 3% contribution from current drifts in the ion source (calculated from the largest observed change in FP current during a typical measurement), 1% from measuring I (stated by the manufacturer), and noise in the pre-amplifier (1%). In total, the systematic uncertainty is ±17%.

Each energy range (0.2 - 1.0 keV, 1.0 - 5.0 keV) was measured 4 times, and the value of the cross section is taken as the mean of the measured values. The statistical uncertainty in the cross section is taken as the standard deviation of the measured cross sections and is of order 5 - 10%. In the initial test of the cell, the cross section for the collision

$$Ar^+(E) + Ar(\text{thermal}) \rightarrow Ar(E) + Ar^+(\text{thermal}) \tag{2.8}$$
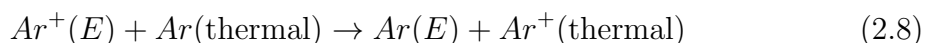
was measured. The measured cross sections, shown in Fig. 2.6, are in excellent absolute agreement with the measurements of Martinez *et al* [67]. Our measurements of the $Ar^+ + Ar \rightarrow Ar + Ar^+$ cross section and the discussion of this apparatus was published in Review of Scientific Instruments, see Bromley *et al.* (2018) [61].
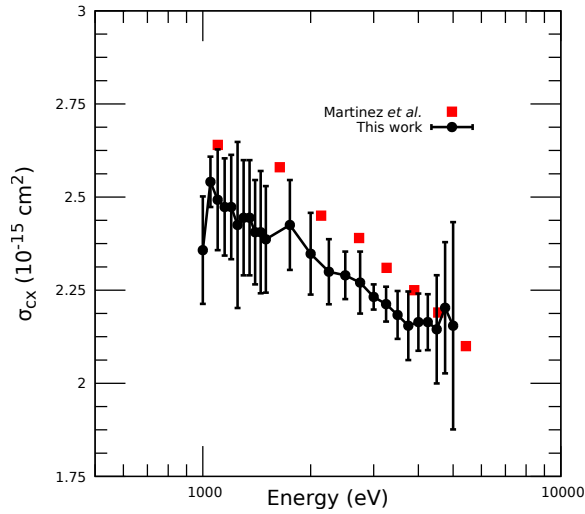
Figure 2.6 Reprint from Ref. [61]. Charge exchange cross sections for $Ar^+ + Ar \rightarrow Ar + Ar^+$ between 1.0 - 5.0 keV. The results of Martinez *et al.* were digitized from Ref. [67].

2.3 Symmetric Charge Exchange with Noble Gas Ions

Parts of the text in this section have been borrowed and/or adapted from Ref. [62]. When both the projectile and target, or ion and neutral, are the same species the charge exchange reaction between them is *symmetric*, and $\Delta E = 0$. In this case the process is *resonant* and charge exchange is possible at any energy. For these systems the cross section dependence on collision energy can be written in the form [20, 21]:

$$\sigma_{cx}^{1/2}(v) = -k_1 \ln(v) + k_2 \tag{2.9}$$

This equation was first derived by Firsov [19] for hydrogen-hydrogen collisions, and was independently found by Dalgarno and McDowell in Ref. [68]. Later, Rapp and Francis (RF) [20] expanded on their work, and later Hodgkinson and Briggs (HB)

[21] expanded upon the work of Rapp and Francis. To summarize, the ion and neutral, A^+ and $A^+ + e^-$, are treated as a non-stationary state of the collision complex (A_2^+), and the Z dependence arises from the ionization potential in the k_1 and k_2 terms. As described in RF, the charge exchange cross section can be calculated from an integration over the impact parameter b and the probability for charge exchange, $P(b,v)$, at velocity v:

$$\sigma(v) = 2\pi \int_0^\infty P(b,v) b \, db \qquad (2.10)$$

In the collision complex, Rapp and Francis assume a hydrogen-like s orbital for the valence electron, and the resulting expression for $P(b,v)$ becomes

$$P(b,v) = \sin^2 \left[\left(\frac{2\pi}{\gamma a_o} \right)^{1/2} \left(\frac{I}{\hbar v} \right) b^{3/2} \left(1 + \frac{a_o}{\gamma b} \right) \exp \left(-\frac{\gamma b}{a_o} \right) \right] \qquad (2.11)$$

where a_o is the Bohr radius, $\gamma = (I_p/13.6 \text{ eV})^{1/2}$, I_p is the ionization potential of the neutral in eV, v is the velocity of the ion, and b is the impact parameter [20]. For small impact parameters b, the probability oscillates between 0 and 1, and decays to 0 at large b. RF assumes this oscillating function averages to 0.5 when considering $b = 0$ to $b = b_1$. The cross section for charge exchange then follows as $\sigma = \frac{1}{2}\pi b_1^2$. To find the value of b_1, RF enforce the condition that $P(b_1, v) = 0.5$, and thus

$$\left(\frac{2\pi}{\gamma a_o} \right)^{1/2} \left(\frac{I}{\hbar v} \right) b_1^{3/2} \left(1 + \frac{a_o}{\gamma b_1} \right) \exp \left(-\frac{\gamma b_1}{a_o} \right) = \frac{\pi}{6} \qquad (2.12)$$

For $(\gamma b_1/a_o) \gg 1$, the pre-exponential factors of b_1 vary negligibly compared to the exponential factor. The pre-exponential b_1 factors are replaced by an average value, $\bar{b}_1$, and the expression may be solved for b_1 within the exponential. Inserting the

resulting expression into $\sigma = \frac{1}{2}\pi b_1^2$ RF finds

$$\sigma(v)^{1/2} = \left(\frac{1}{2}\pi\right)^{1/2}\left[-(a_o/\gamma)\ln(v) + (a_o/2\gamma)\ln\left[\frac{72\bar{b}_1^3}{\pi\gamma a_o}\left(\frac{I^2}{\hbar^2}\right)\left(1+\frac{a_o}{\gamma\bar{b}_1}\right)^2\right]\right] \quad (2.13)$$

which simplifies to Eq. 2.9. In the absence of non-resonant terms that may contribute at high energies (e.g., ionization without charge exchange), the v dependence of the cross section may be viewed classically as a time dependence. For faster ions, less time is available for the charge exchange to occur, and the cross section for the charge exchange is decreased. Eq. 2.9 holds for intermediate velocities (10^5 cm/s $< v < 10^8$ cm/s), and the parameters k_1 and k_2, though not explicitly listed in the publications of RF and HB, may be found by digitizing the $\sigma(v)$ versus v plots from both papers.

In 2000, Pullins *et al.* [69] noted an error in the assumption of the potential used by Rapp and Francis. The original potential assumed by Rapp and Francis takes the form [69]:

$$\Delta V(r) = 2I_p r\exp(-\alpha r) \quad (2.14)$$

where $\alpha = (2I_p)^{1/2}$. At the large distances where charge exchange occurs, the potential is more correctly written as

$$\Delta V(r) = \frac{8}{3}I_p r\exp(-\alpha r) \quad (2.15)$$

Such an error leads to the RF values of k_1 and k_2 underestimating the values of the cross section. In the remainder of this work, the values for the RF k_1's and k_2's are those with the 4/3 prefactor from Pullins *et al.* [69] applied.

Using the apparatus and experimental procedure described in Sec. 2.2, the

cross sections for the collisions $A^+ + A \rightarrow A + A^+$ (A = He, Ne, Ar, Kr) were measured between $E = 0.2 - 5.0$ keV. The results in the following discussion were published in Journal of Physics B: Atomic, Molecular, and Optical Physics in Ref. [62]. The measured cross sections are compared to the available results in the literature and the RF (with Pullins *et al.* [69] correction applied) and HB predictions as digitized from the original papers [20, 21]. The values of k_1 and k_2 for the original predictions and a fit of Eq. 2.9 are recast into the form

$$\sigma^{1/2}(E) = -k_1 \ln(E) + k_2 \tag{2.16}$$

and listed in Table 2.1 where the energy E is in eV and the resulting cross section, $\sigma_{cx}(E)$, is in cm^2.

Our apparatus and procedure measure the total attenuation from the initial ion beam attributed to neutralization of ions in the beam by single charge exchange. However, other (non-CX) processes should be considered, *i.e.* ionization, elastic scatter, and inelastic scatter. While the cross sections for ionization of neutrals by ions in these specific systems are unmeasured, the values obtained for a comparable system are found to be approximately 10^{-18} cm^2 [70] or nearly three orders of magnitude below the σ_{cx} values obtained here. For the elastic and inelastic processes, differential cross section data for these species have been obtained by other groups (He [71, 72], Ne [73], Ar [74, 73], Kr [73]). In these data, the authors find that the cross section for elastic scatter is comparable to that of charge exchange. However, differential cross-section measurements show the data to be strongly peaked in the forward direction. Given the acceptance angle of our gas cell apertures, ions participating in forward peaked elastic scatter are not attenuated from the beam. In these noble gas reactions, inelastic scatter is preferentially through angles greater than several degrees but the

magnitudes are small compared to the magnitude of elastic scattering cross sections at these energies.

A final consideration is the ion beam source in which ions are produced by electron bombardment which could lead to the production of excited ions. However, the velocity of the ions ($\approx 10^6$ cm/s) and the distance from the ion source to the gas cell ensure that all but metastable ions have decayed to the ground state before entering the gas cell. To check the effect of metastable ions in the incident beam on the measured cross sections, measurements were repeated at various ion source pressures, which should modulate the metastable population. No measurable effect was found. Therefore, it is assumed that the fraction of metastable ions present in the incident beam is small enough to be negligible.

Historically, symmetric cross sections were obtained by measuring ion beam current losses after passing through a gaseous target, and the charge exchange cross section is calculated in one of two ways. The cross section may be calculated from integrating a set of measured differential cross sections (e.g. [71]), or only the total cross section is obtained as in Ref. [75]. In literature involving the first case, the differential cross sections are measured with large step sizes between collision energies ($\sim$ keV). Additionally, these measurements are often complicated by small beam currents which are sensitive to fluctuations in ion source conditions. In the second case, misalignment of the ion beam and/or scattering outside of the acceptance angle of the detector can contribute to systematic errors. In the literature, most works have restricted themselves to 'low' ($E < 1$ keV) or 'high' ($E > 1$ keV) energies. In this work, the UHV manipulator allows for precise alignment with the center of the ion beam, and the large angular acceptance allows for collecting all collision products within the expected range of forward scatter. Combined with the energy range of our apparatus, 0.2 - 5.0 keV, our cross sections may be used to bridge the gaps between

previous experiments and benchmark the available predictions across the intermediate regime.
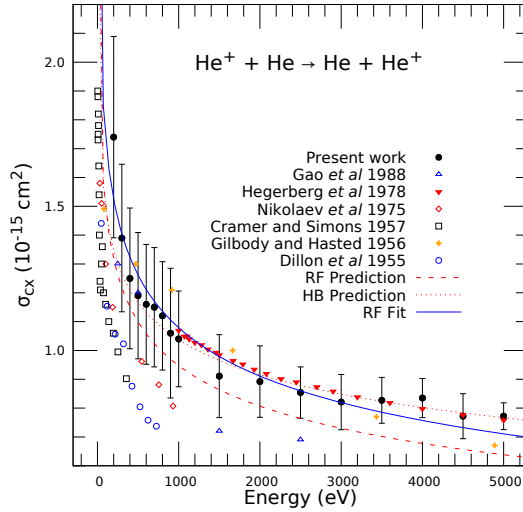
Figure 2.7 Current and prior [71, 75, 76, 77, 78] measurements of the total charge exchange cross section for He$^+$ + He. The error bars shown represent statistical uncertainty in these measurements which also have a systematic uncertainty $\pm$ 17%. Theoretical treatments based from Rapp and Francis (RF) [20] and Hodgkinson and Briggs (HB) [21] as well as a fit of the present measurements to Eq. 2.9 are shown as dashed red, dotted red, and solid blue lines respectively.

.

The total charge exchange cross section obtained for He$^+$ on He between 0.2 - 5.0 keV is shown in Fig. 2.7 and on an expanded scale in Fig. 2.8. We observe the expected qualitative trend, which is a reduction in σ_{cx} as a function of the ion energy. In addition, our data show an overall agreement with multiple previous measurements on this system which serves to validate our experimental approach. There is a deviation from prior data below 1000 eV which can be attributed to the different methods used in those measurements (Gilbody and Hasted [78] and Nikolaev *et al.* [76]) in particular to the assumptions made about the role of inelastic processes at higher pressures. Figures 2.7 and 2.8 also show the predicted energy-
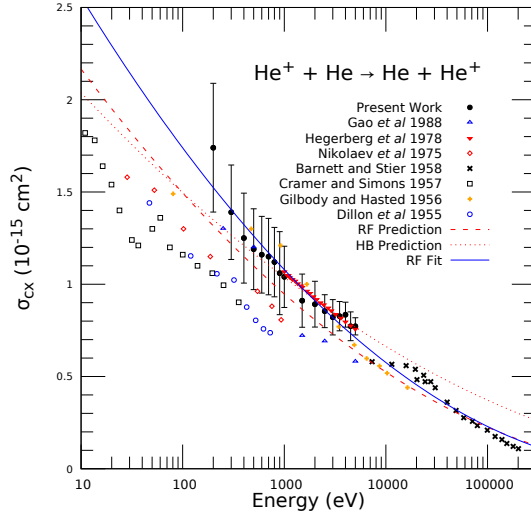
Figure 2.8 Total charge exchange cross section for He^+ + He on an expanded energy scale. The error bars shown represent statistical uncertainty in these measurements which also have a systematic uncertainty $\pm$ 17%.

dependence based on the treatments of RF and HB. Both methods agree with the present intermediate velocity results, and the RF agreement extends out to include the higher energy results (Fig. 2.8) obtained by others.

Our results for Ne^+ charge exchange cross sections between 0.2 - 5.0 keV are shown in Fig. 2.9 as well as prior results obtained for this system that extend well out beyond 1 MeV [79, 78, 80]. The current data appear to be in good agreement with the measurements of Kikiani *et al.* [79] and Gilbody [78] but differ significantly from those of Dillon *et al.* [80]. Given the much different setup used in Ref. [80], especially with respect to a possible underestimation of the path length over which the charge exchange has occurred, it is reasonable to assume the cross sections obtained by these authors are underestimated. As in the He case, also shown are the results from the treatments of RF and HB. Both the RF and HB results consistently overestimate the cross section above 1 keV compared to the present results.

Figure 2.10 shows the total charge exchange cross sections for Ar^+ on Ar as
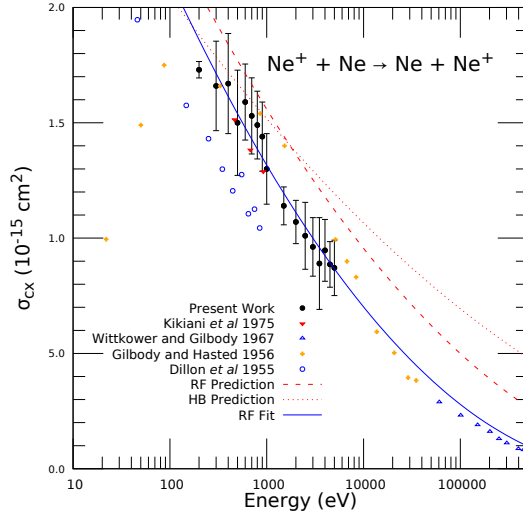
Figure 2.9 Total charge exchange cross section for $Ne^+ + Ne$ on an expanded energy scale. Data from Refs. [79, 78, 80] are shown. The error bars shown represent statistical uncertainty in these measurements which also have a systematic uncertainty $\pm$ 17%.

well as other prior measurements [67, 61, 69, 81, 80]. These include our own previous measurements obtained during the benchmarking of the apparatus [61]. For the intermediate velocity range we show excellent agreement with the measurements of Martinez *et al* [67] while the results of Dillon *et al.* [80], as noted previously, are lower compared to the current data. Both the RF and HB treatments appear to agree with our measured cross sections; however, significant deviations are apparent at both lower and higher energies for the HB result. Compared to the previous low energy results, the trend of our cross sections beneath 1 keV is inconsistent with both the work of Pullins *et al.* [69] and the RF prediction. While it is possible that our source produces both the metastable Ar^+ $(^2P_{1/2})$ and ground Ar^+ $(^2P_{3/2})$ ions, which differ in cross section by as much as 10% beneath 1 keV [69], the population of metastable Ar^+ $(^2P_{1/2})$ is expected to be small as discussed previously. The discrepancy between the present work and Pullins *et al.* is unexplained.
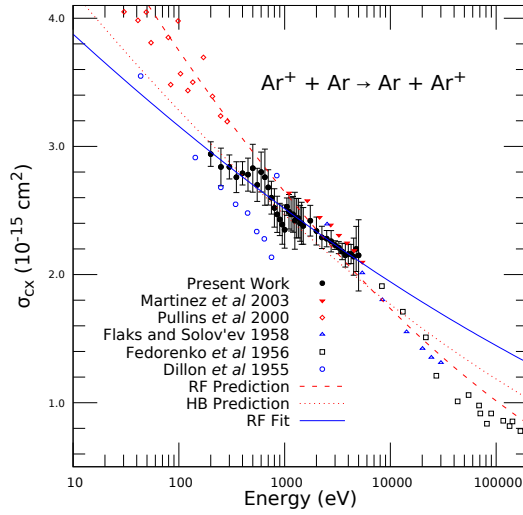
Figure 2.10 Total charge exchange cross section for $Ar^+ + Ar$ on an expanded energy scale. Data from Refs. [67, 61, 69, 81, 80] are shown. The error bars shown represent statistical uncertainty in these measurements which also have a systematic uncertainty $\pm$ 17%.

Figure 2.11 shows the data obtained for the $Kr^+ + Kr$ cross section as well as other experimental measurements [82, 83, 84, 80]. The most contemporary data are from Hause *et al.* [82] who measured cross sections in the range of 1 - 300 eV using the guided ion beam technique. Those results, which overlap with the current data at 300 eV, differ by only 4% at this point. Overall, below 1000 eV the current data are in agreement with the work of Kushnir *et al.* [84] but appear higher than the measurements of Galli *et al* [83] and, as in the other systems studied, the data of Dillon *et al.* [80]. The RF prediction is in excellent agreement with the present work and Kushnir *et al.* [84] below 1 keV. In this energy range, the HB prediction is smaller by as much as 7%. A fit of the present work to the RF functional form is similar to the RF prediction at low energy and in agreement with the work of Hause *et al* [82]. In the extrapolation of the fit curve to energies above 5 keV, where experimental measurements do not exist for Kr, the fit curve and the RF prediction
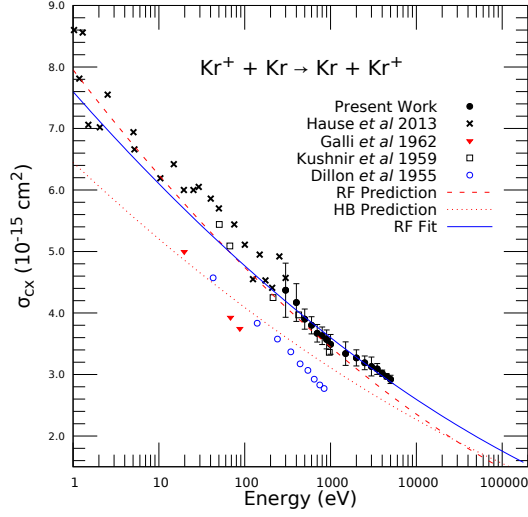
Figure 2.11 Total charge exchange cross section for $Kr^+ + Kr$ on an expanded energy scale. Data from Refs. [82, 83, 84, 80] are shown. The error bars shown represent statistical uncertainty in these measurements which also have a systematic uncertainty ± 17%.

start to diverge. The good agreement of the extrapolated curve in He and Ne to the available experimental data is suggestive that the present measurements may be useful for determining the cross section at higher energies also. The numeric values of the fit parameters as well as those extracted from the published RF and HB predictions are recast in the form $\sigma_{cx}^{1/2}(E) = -k_1'\ln(E) + k_2'$ and listed in Table I.

For all four cases, the cross sections monotonically decrease as a function of energy and fit well to the expected functional form as expressed in Eq. 2.9. The RF and HB predictions are useful tools for predicting the magnitude of the charge exchange cross section in the measured energy range and require only knowledge of the ionization potential. However the agreement with the fit deviates at energies below 100's eV and greater than 10 keV as compared to previous measurements. At high energy, HB overestimates the magnitude for the He, Ne, and Ar. The RF prediction also overestimates the magnitude of the cross section in the case of Ne and

Table 2.1 Values of the two parameters k_1' and k_2' for theory [20, 21] and experimental fits. Values listed give cross sections in cm^2 with energy E in eV.

Element		k_1' ($\times 10^{-9}$)	k_2' ($\times 10^{-8}$)
	HB Prediction	2.808	5.161
He	RF Prediction	3.424	5.443
	RF Fit	3.845	5.491
	HB Prediction	2.741	5.790
Ne	RF Prediction	3.722	6.520
	RF Fit	4.251	6.565
	HB Prediction	3.309	7.253
Ar	RF Prediction	4.252	8.080
	RF Fit	2.631	6.831
	HB Prediction	3.551	8.013
Kr	RF Prediction	4.415	8.919
	RF Fit	3.822	7.724

Ar. (There is no experimental data for Kr in this energy range.) This is most likely due to the difficulty in including the contributions from different impact parameters correctly. As an alternative to relying solely on either theoretical calculation, fits of the functional form (Eq. 2.9) to our current measurements better approximate the cross section at higher energies in the case of He and Ne as compared to the previous experimental data shown. The agreement in these two cases may not be so surprising as k_1 and k_2 are constant at high energies in the original derivations by RF and HB.

However, at low velocities an average treatment of the impact parameter, which produces constant values for k_1 and k_2, may not be sufficient. At very low energies the charge exchange process is highly dependent on the electronic structure of the quasi-molecule formed through the course of the collision [20]. The representation of the wavefunction at low energies is complicated by the molecular states involved in the charge exchange process. To further develop a general expression for single charge exchange across an expanded energy range, full theoretical treatments of the

A$_2^+$ (A = He, Ne, Ar, Kr) quasi-molecule and additional benchmarking experiments are required.

2.4 Charge Exchange between Noble Gas Ions and N$_2$

The following text details measurements of the total absolute charge exchange cross sections of noble gas ions and molecular nitrogen. The measurements were published in *Atoms*, see Ref. [63]. Consider again Eq. 2.1 with singly charged ions, i.e.

$$A^+ + B \rightarrow A + B^+ + \Delta E \tag{2.17}$$

When the neutral B in Eq. 2.17 is a molecule, the charge exchange cross section deviates from the expected behavior for asymmetric or symmetric reactions. Typically when $\Delta E = 0$, the process is resonant as in the case of the symmetric collisions presented previously where the cross section is well explained by semi-classical calculations over most energy ranges. Asymmetric reactions (A $\neq$ B) may exhibit similar behavior for reactants with small energy defects, e.g. H$^+$ + O $\rightarrow$ H + O$^+$ + $\Delta E(\sim 0)$ [22]. When the energy defect is large ($\Delta E > 0$), the cross section is typically smaller [85]. However, cross sections for reactions with a large ΔE may become significant in certain high collision energy regions.

When reactant B is a molecule, the number of possible reaction channels is large compared to the atomic case, and the energy dependence of the charge exchange cross section deviates from the single-peaked structure seen in asymmetric reactions such as those compiled by [18]. This is illustrated in particular by collisions between N$_2$ and atmospheric ions H$^+$ and O$^+$ in the summary of [22]. In the case of the
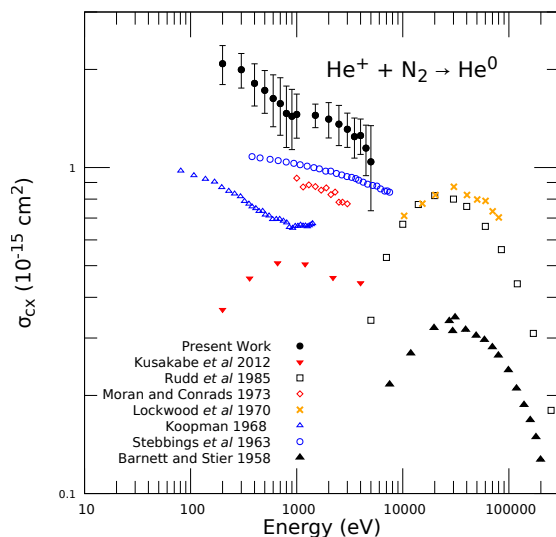
Figure 2.12 Total charge exchange cross sections for He^+ and N_2. The measurements shown: full circles (present work, manipulator-mounted gas cell (MGC)), inverted triangles [86], hollow squares [87], diamonds [88], × [89], hollow triangles [90], open circles [91], triangles [92]. The error bars shown represent statistical uncertainty in the present measurements.

He^+-N_2 reaction, discrepancies still remain between a variety of experimental efforts [86, 87, 88, 89, 90, 91, 92], including as much as a factor of 3 in magnitude and qualitatively different behaviors as a function of collision energy.

Using the MGC apparatus and technique discussed previously, we present measurements of the charge exchange cross sections for the reactions $A^+ + N_2 \rightarrow A$ (A = He, Ne, Ar, Kr). The measurements were carried out with the same procedure as previously discussed for the symmetric reactions, and the results are compared to the available literature.

The charge exchange cross sections for the noble gas ions and neutral N_2 are shown in Figs. 2.12 - 2.15. The $He^+ + N_2$ reaction has been studied across a wide energy range [86, 87, 88, 89, 90, 91, 92]. All seven previous results shown in Fig. 2.12 utilized a gas cell or similar apparatus, and all but Rudd et al. [87] and Koopman [90] were able to measure both the charged and neutral components of
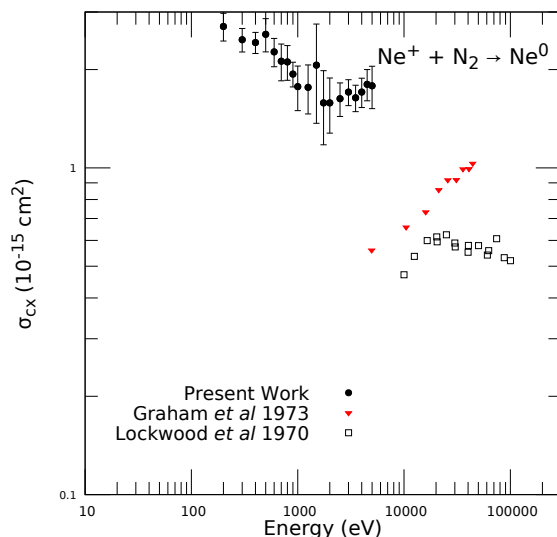
Figure 2.13 Total charge exchange cross sections for Ne^+ and N_2. The measurements shown: black circles (present work, MGC), inverted triangles [93], squares [89]. The error bars shown represent statistical uncertainty in the present measurements.

the ion beam post-charge exchange (CX). By looking at the slow collision products, both Koopman [90] and Stebbings [91] identified the dominant CX channel as the disassociation $He^+ + N_2 \rightarrow He + N^+ + N$ via a two-step process.

As shown in Fig. 2.12, experiments at energies above 10 keV agree in trend, showing a peak at around 30 keV. For energies below 10 keV, the works of [88, 90, 91] show a monotonic decrease in the cross section with increasing energy. The most recent work [86] suggests a drop off toward low energies which is inconsistent with the He^+-N_2 results from [91, 90]. The apparatus of Kusakabe et $al.$ [86] is able to examine the charged and fast neutral components of their primary ion beam but are not equipped to detect the slow collision products. The measured decrease in σ_{cx} with decreasing energy by [86] was argued to be a consequence of the energy defect for the dissociation process, $\Delta E \sim 0.2$–0.3 eV.

Our measurements show a monotonic decrease with increasing energy; however, our cross sections are systematically higher. A voltage of -120 V was applied

48

to the suppression electrode to reflect any secondary electrons produced from the fast neutral component of the ion beam hitting the Faraday cup. Our measured cross sections include a contribution from elastic and inelastic scatter from angles above 13°.

For $Ne^+ + N_2$, only two experimental results are available [89, 93]. Lockwood's cross sections [89] are nearly half an order of magnitude smaller than the present work and span an energy range outside the scope of our apparatus. The measurements by Graham et al. [93] studied the charged and neutral components of their ion beam post-CX, but their measured cross sections were placed on an absolute scale by comparison to known cross sections of protons in the respective target gases. The only point where the measurements of [93] overlap with the present work is at 5 keV where the present measurements are four times larger. This reaction's angular dependence is unstudied and our data again may include contributions from large angle elastic and/or inelastic scatter. Assuming the other works in Fig. 2.13 isolated the charge exchange component of the total cross section, our measurements indicate that large angle non-CX scatter is comparable to CX between 0.2 and 5.0 keV.

$Ar^+ + N_2$ collisions have been studied from 0.01 to 100 keV by several groups [94, 95, 89, 96]. The earliest work by [96] measured the energy distribution of both the charged and neutral component of the transmitted ion beam, and inferred the dominant reaction channel at low energy was $Ar^+ + N_2(v = 0) \rightarrow Ar + N_2^+(v = 1) + 0.093$ eV. At higher energies, [94] suggests that the large number of near-resonant reaction channels leads to a relatively flat cross section as a function of energy. For measurements between 0.5 and 1 keV, we find excellent agreement between the present work and [94]. The present work and [94] have the same magnitude cross section as the higher energy results of [89, 95].

For Kr^+-N_2 (Fig. 2.15), only one previous work is available, Lockwood (1970) [89].
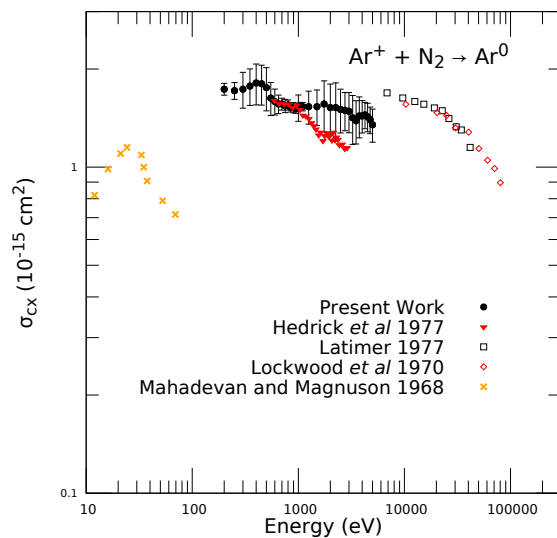
Figure 2.14 Total charge exchange cross sections for Ar^+ and N_2. The measurements shown: black circles (present work, MGC), inverted triangles [94], squares [95], diamonds [89], × [96]. The error bars shown represent statistical uncertainty in the present measurements.
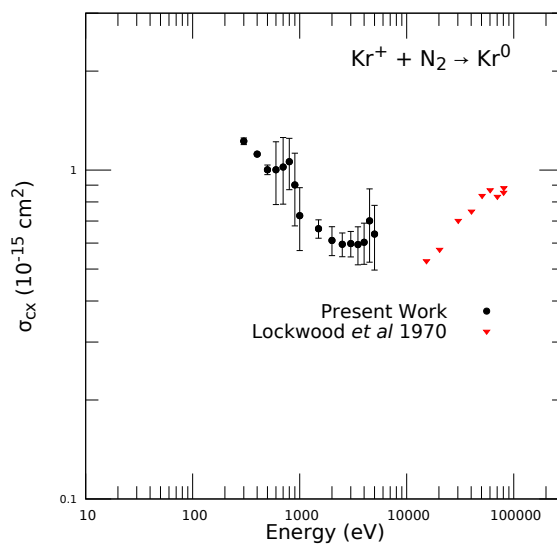
Figure 2.15 Total charge exchange cross sections for Kr^+ and N_2. The measurements shown: black circles (present work, MGC), inverted triangles [89]. The error bars shown represent statistical uncertainty in the present measurements.

This paper contains measurements above 10 keV for all four systems studied here. Unlike Lockwood's results in He$^+$ and Ar$^+$, their data show an increase in σ_{cx} with increasing energy for Kr$^+$-N$_2$. This indicates that the collision energy of the cross section maximum is higher than in the other cases. We note that of the four reactions studied here, only the Kr$^+$-N$_2$ reaction contains a negative energy defect ΔE.

In summary, a manipulator-mounted gas cell was designed for measuring charge exchange cross sections with large magnitudes. The apparatus was tested by measuring cross sections for the symmetric reaction Ar$^+$+Ar, and the results are consistent with the available literature [61]. Using the vetted apparatus, measurements of σ_{cx} were carried out for the other symmetric collisions A$^+$-A (A = He, Ne, Kr). The measured cross sections are consistent with the available experimental and theoretical results for these systems. Comparison of the RF [20] and HB [21] theories to the compiled data suggests that the RF expression, corrected with the 4/3 prefactor from Pullins *et al.* [69], most often shows the best agreement with the compiled data. However, at higher energies where experimental data are sparse, fits to experiments in the keV range may more appropriately capture the energy dependence of the cross sections at high ($E > 10$s keV) energies.

Additional experiments were conducted to measure the energy dependence of σ_{cx} for A$^+$ (A = He, Ne, Ar, Kr) and N$_2$ targets. In each of the four cases, the measured cross sections appear inflated w.r.t. the limited measurements in the literature. From these cases, we expect that elastic and/or inelastic scattering processes to angles beyond 13° may be comparable to charge exchange in the keV energy range.

2.5 Design and Benchmarking of an Electrically Floated Gas Cell

The work in this section builds upon the design and discussion of the electrically floated gas cell from Bromley *et al.*, *Atoms* (2019) [63]. Here we have expanded the discussion of the design and possible future modifications in the following sections.

2.5.1 Design & Assembly

Having the gas cell attached to the manipulator is very useful for aligning the gas cell to the beam while the apparatus is under vacuum. However, the design has several disadvantages. Most importantly, the pressure gauge for the gas cell was located 14 inches from the cell and connected by 1/4 inch flexible stainless steel tubing. As a result of this, it took several minutes after each pressure change for equilibration to be reached between the gas cell and the gauge. With the current ion source, each adjustment of the beam energy requires manual adjustments of the three ion source voltages ($V_{\text{energy}}, V_{\text{extract}}, V_{\text{focus}}$). The combination of manually adjusting these voltages and waiting for the pressure to stabilize leads to a typical measurement of 10 different energies taking between 1 - 1.5 hours. This is particularly problematic if the pre-gas and post-gas values of I_o differed significantly which would lead to the measurements being discarded. Lastly, the long tubing for gas injection prolongs the return to system base pressure, i.e. 2×10^{-8} mbar after 1–2 hours.

A new gas cell was designed to improve the accuracy of the pressure measurements and speed up the data collection. This design incorporates several key changes to address the issues related to the long measurement times. First, the conductance between the gas injection and pressure measurement is considerably increased. The

leak valve (injection) and pressure gauge (measurement) are connected to a 2-3/4"
CF cross which attaches to an 8" CF flange at the top of the chamber. An internally
threaded cylinder was machined such that the outer diameter was ~0.001" larger
than the hole in the mounting flange. After cooling the cylinder in liquid nitrogen,
the cylinder was placed inside the hole in the flange and allowed to rise to room tem-
perature. A hollow tube (inner diameter 1.3") threaded into this fixed cylinder thus
connects the gas reservoir to the cell body. This assembly technique allows minimal
gas leakage from the reservoir to the chamber.

The hollow tube is both rotatable and translatable, but changes to the orien-
tation and height must be made at atmosphere. By adjusting the height and rotation
of the rod the attached cell may be aligned with the ion source via a HeNe laser.
The position of the rod is locked in via a retaining nut on the external threads of the
hollow rod. This design provides a large increase in conductance which decreases the
time to wait for pressures to stabilize during gas injection or a complete gas shut-
off. After installation and initial pumpdown, the system base pressure is reduced to
5×10^{-9} mbar, a factor of 4 improvement over the MGC design.

Second, the measurement duration is significantly affected by the number of
beam energies chosen. For each energy, the three ion source voltages are scanned by
hand. In this new design the initial beam energy is set at the source. By electrically
floating the entire gas cell to a high voltage, the incoming ion beam is decelerated, and
the ion beam energy becomes $E_{\mathrm{ion}} = |e|(V_{\mathrm{source}} - V_{\mathrm{decel}})$. By utilizing a programmable
power supply incorporated into the system's LabVIEW control software, scanning
the energy at a given target pressure is limited only by the high voltage rise time and
response of the associated electronics.

This new design, named the "(electrically) Floated Gas Cell" (FGC) is shown
in Figure 2.16. The cell itself is similar in size to the MGC discussed in Sec. 2.2, and

the design drawings were prepared by undergraduate Corey Ahl. The gas cell body is machined from a single block of 316 stainless steel. A central bore along the length of the block, and a second hole drilled perpendicular w.r.t the first, were machined in the block with an internal diameter of 40 mm. The length of the body (40 mm) ensures a similar path length to the MGC design. The gas reservoir is connected to the cell body via the hollow rod discussed previously, and electrical isolation is provided by a MACOR ring between the cell body and the hollow rod. This MACOR ring was machined with a shoulder such that a titanium mesh could be braced within it. The MACOR ring and mesh are shown in the right side of Fig. 2.16. The mesh prevents an E-field perpendicular to the ion beam caused by the floated cell and the nearby grounded support rod. Teflon sleeves insulate the screw heads connecting the cell body and the hollow support rod.

The order and separation (0.100") of electrical components is identical to the MGC, and an incident ion beam passes through (in order): faceplate (1 mm aperture), skimmer (1 mm aperture), front endcap (3 mm aperture), back endcap (4 mm aperture), retarding field analyzer (5 mm aperture), suppression electrode (5 mm aperture), and faraday cup (10 mm aperture). Note that both faceplate and skimmer have smaller apertures (2 & 3 mm in the MGC design, 1 & 1 mm in the FGC), and the incoming ion beam is more collimated with a smaller radius and less transmitted current. The angular acceptance is similar to the MGC ($\pm 13°$ w.r.t the incoming beam). Additionally, a change was made to the retarding field analyzer to improve the E field of the RFA. A depression in the RFA allows a fine mesh to be placed within the aperture of the RFA, and a backing plate bolts to the RFA and holds the mesh in place. This RFA design, shown in Fig. 2.17, offers a more robust means of holding the thin mesh rigid and perpendicular to the incoming beam. The mesh used was a 100×100 stainless steel mesh (wire thickness 0.001", open area 90%), and

54
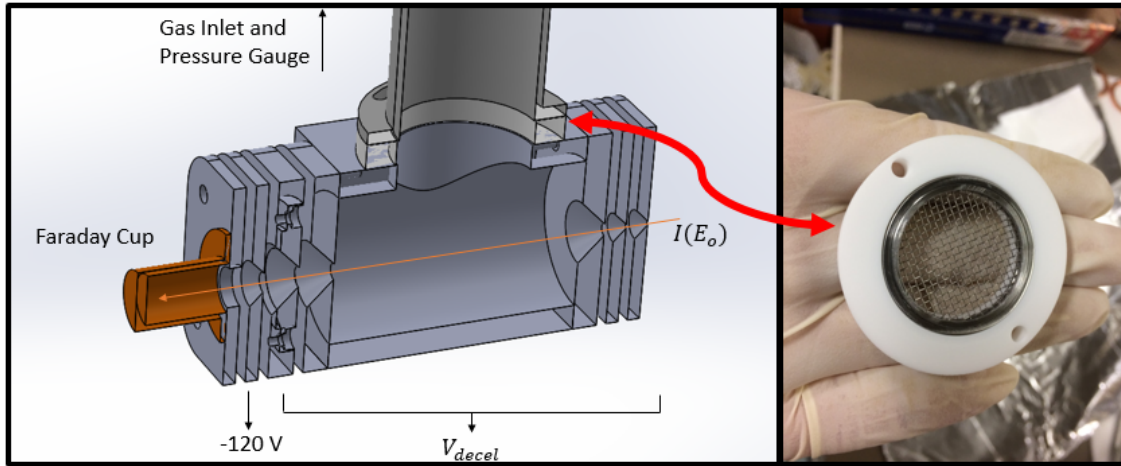
Figure 2.16 *(Left)* A SOLIDWORKS design of the FGC. Shown is the gas inlet, MACOR spacer (mesh not shown), and gas cell components with knife edges. The direction of the incoming beam is indicated by the orange arrow. *(Right)* A photograph of the MACOR spacer and the encapsulated wire mesh.

measurements of beam currents with and without the mesh verify the manufacturer stated open area.

The assembled cell body is shown in Fig. 2.18. Each electrical component slides along 4 pieces of #4-40 rod screwed into the four corners of each face of the cell body. Components are separated by 0.100" thick MACOR top-hat washers, and the components are held in place by #4-40 nuts at the end of each threaded rod. Electrical connections (not shown) are made by attaching UHV-compatible wire to each component, and connections to atmosphere are made through two electrical feedthroughs at the bottom of the vacuum chamber.

2.5.2 Benchmarking the FGC Design

Following the design and construction of the FGC, the apparatus was attached to the same chamber used for the MGC. The cell is aligned with the ion source via a HeNe laser, and the cell position is locked in via tightening of the retaining nut.
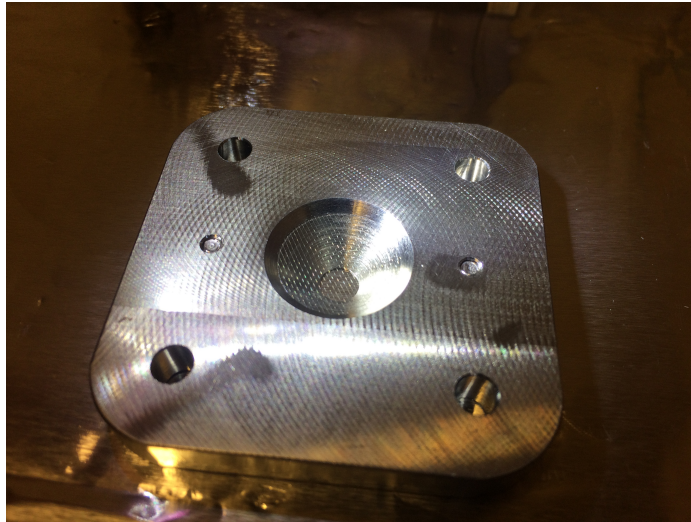
Figure 2.17 A photograph of the back of the FGC RFA with the mesh in place.

Figure 2.18 A photograph of the assembled FGC body. The order and purpose of each component mimics those of the MGC in Fig. 2.1.
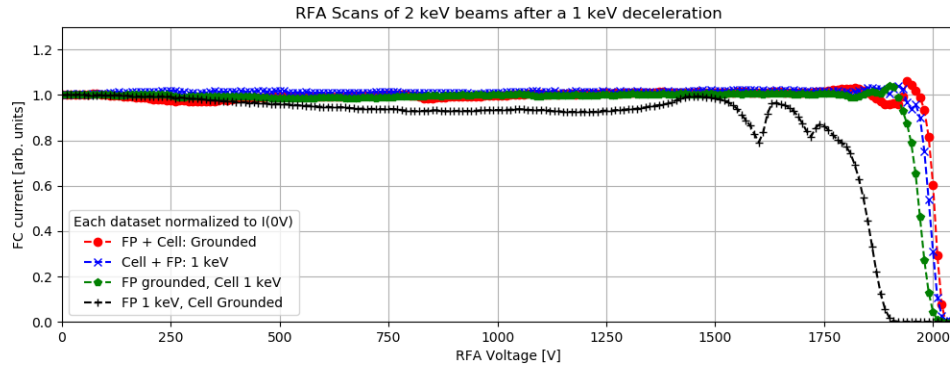
Figure 2.19 RFA voltage scans of 2 keV Kr$^+$ beams after passage through various components floated at 1 keV. The y-axis was normalized such that $I_{FC}(V = 0)$ was set to 1 for each dataset.

Initial tests of the FGC show a decreased chamber pressure due to the removal of the manipulator. During operation with noble gases, the ratio of cell pressure to chamber pressure is similar to the MGC and is 700 - 1000 depending on the gas species. However, the time to stabilize following a change of gas injection pressure is reduced to only a few minutes, and the time to return to system base pressures following gas shutoff is significantly reduced from 1 - 1.5 hours to ~15 minutes. Similarly, the duration of a measurement spanning 10 energies is signficantly reduced by the use of the deceleration system from 1 hr to 15 - 20 minutes.

By performing RFA scans of an ion beam after passage through the cell, we may understand the effect of the deceleration potential on the ion beam. Fig. 2.19 shows a plot of the Faraday cup current I_{FC} versus RFA voltage for a 2 keV beam passing through various components floated at 1 keV. The red circles represent a typical $I - V_{RFA}$ profile for an ion beam. For a 2 keV beam, the RFA voltage has no effect until ~1900 V where the RFA voltage acts to focus the ion beam. At higher voltages, the ion beam is rejected and the beam is cutoff at approximately the ion beam energy. With both the cell body and faceplate (+ skimmer) floated at the deceleration potential, the RFA curve is nearly identical. With the skimmers

57
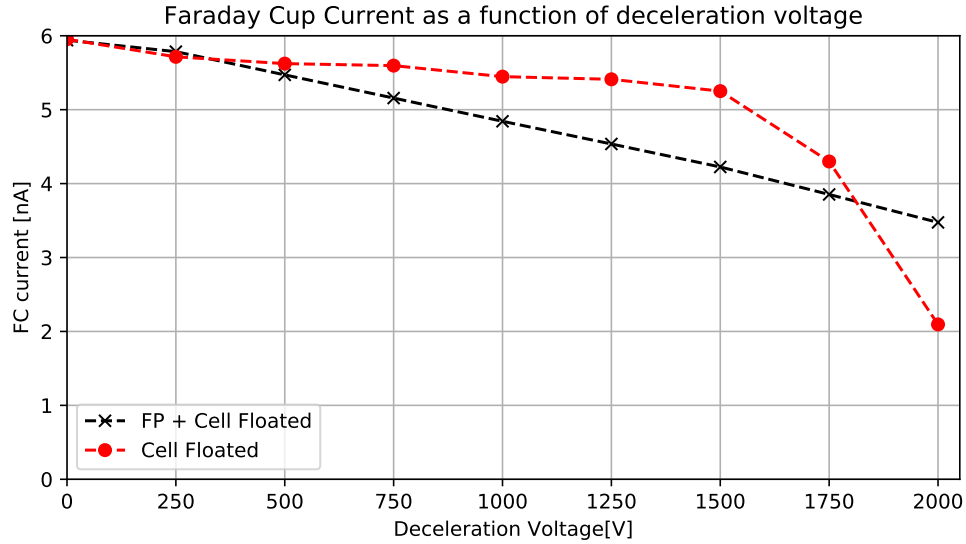
Figure 2.20 Faraday cup currents as a function of V_{decel} for a 3 keV Ar$^+$ beam. The black '×' were measured with both the cell and faceplate at the deceleration voltage, and the red 'O' represent data taken with only the cell floated at the deceleration voltage.

grounded and the cell body floated at 1 keV (green circles), we see that the RFA curve is similar in shape to the no-decel curve. However, with only the faceplate at the deceleration voltage we see a complicated transmission profile, and the beam is cut off nearly 100 V lower than the ion beam energy. This is likely due to stray fields caused by the lack of ground in front of the faceplate and possibly the exposed (floated) ends of the threaded rod holding the electrical components.

Alternatively, we may examine how the deceleration voltage affects the measured currents. Ideally, the I_{FC} vs V_{decel} curve would imitate the no-decel RFA curve in Fig. 2.19. However, due to machining tolerances and the choice of knife-edges on the cell components, a different behavior is observed. Figure 2.20 shows the measured faraday cup currents for an Ar$^+$ beam, originally at 3 keV, and the resulting faraday cup currents as the deceleration voltage is scanned from 0 - 2 keV. The black '×' are measured by scanning V_{decel} with both the faceplate and cell body floated to the

deceleration voltage, and the red 'O' are the measurements with only the cell body floated. As shown, the data with only the cell floated indicate a non-linear behavior as V_{decel} approaches the beam energy. For a 2 keV beam (not shown), the dropoff is significant, and the available beam energies are limited. However, when floating both the skimmers and cell body, energies as low as 300 - 400 eV are achievable. As there is gas leakage out of the ends of the cell, the ion velocity must be well defined before entering the gaseous region. Therefore for the following work, we require that both the skimmers and cell body be floated to ensure the ions are decelerated before entering the target gas.

When decelerating ions with both the faceplate and cell body at V_{decel}, the FC currents drop linearly with deceleration voltage. The most likely explanation of this behavior is a perpendicular component of E_{decel} arising from the alingment with the incoming ion beam or uneven removal of material during the machining of each knife-edge aperture. As V_{decel} increases, the perpendicular component of v_{ion} (w.r.t the axis of the cell) grows in comparison to the longitudinal component of v_{ion}. One would expect that for a beam without perfect alignment with the axis of the cell, off-axis ions move outside the collection angle of the FC as V_{decel} is increased. The cone shape of each aperture likely contributes to this effect.

We may look at the effect of target gas on the I_{FC} measurements. The behavior as a function of gas pressure should mimic that seen in the MGC (see Fig. 2.5). Of the accessible reactions, symmetric charge exchange cross sections are largest for Kr at low energy, and thus the current loss due to charge exchange should be the largest. As the cross section decreases with increasing energy, any effect of the deceleration voltage on the observed current losses (as a function of energy) should be more pronounced at lower energies, i.e. high deceleration voltage.

As a test, a beam of Kr^+ was generated at 1 keV and decelerated from 1 keV
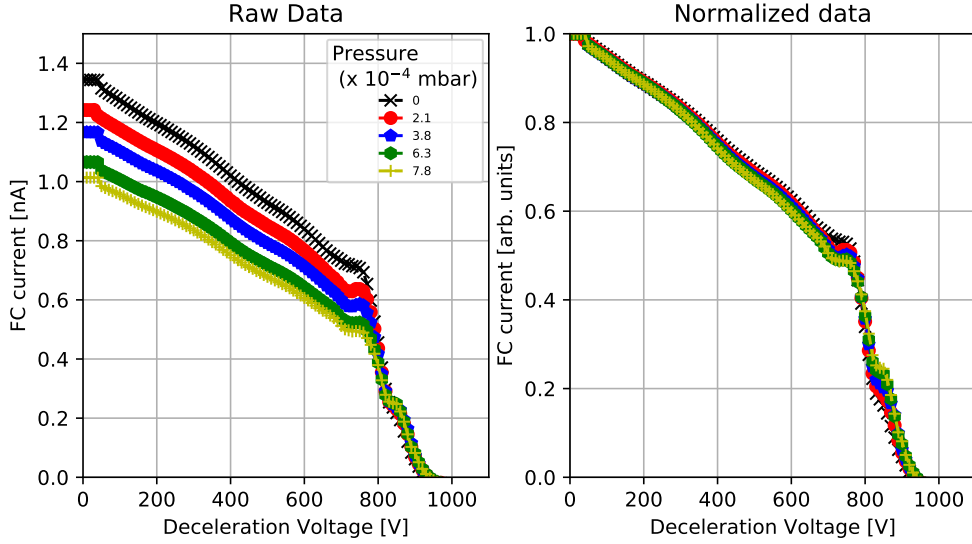
Figure 2.21 Faraday cup currents as a function of deceleration voltage at various target pressures. *(Left)* Raw data for I_{FC} versus V_{decel}. *(Right)* The same data normalized such that $I_{\mathrm{FC}}(V = 0) = 1$ for each pressure.

to 0 keV by scanning V_{decel} at 4 gas pressures between $2 - 8 \times 10^{-4}$ mbar. The results are shown on an absolute scale (left) and a normalized scale (right) in Fig. 2.21. As shown, the measured FC current at each deceleration voltage decreases with pressure. The structure of the FC current versus V_{decel} curve is largely independent of the gas pressure beneath $\sim$750 eV ion energy. Above 750 eV, a non-linear drop in FC current, as a function of deceleration voltage, is observed at all gas pressures, and the beam is cut off $\sim$ 50 - 100 eV lower than the selected beam energy (1 keV). This is not a problem if the current loss is linear with gas pressure. Using the same dataset, Fig. 2.22 shows plots of $\Delta I/I$ versus cell pressure for selected ion energies. As shown, the current loss, even at high energy, i.e. low deceleration voltage, deviates from the linearity seen in similar plots from the MGC, e.g. Fig 2.5. Therefore, we assume that this deceleration method is only applicable when the ion energy is large relative to the deceleration voltage.
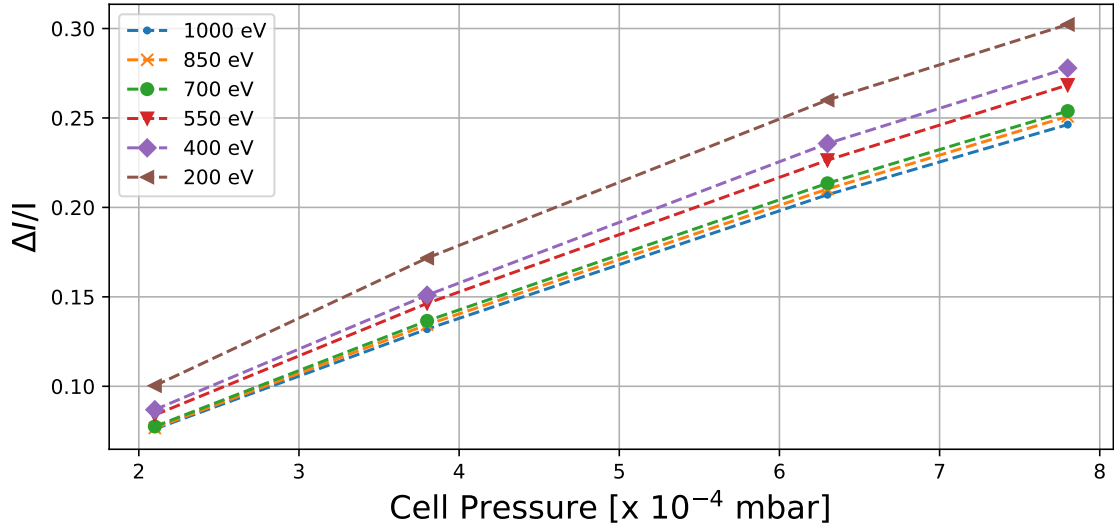
Figure 2.22 $\Delta I/I$ versus cell pressure for a decelerated 1 keV beam at selected ion energies. Note that $E_{\text{ion}} = |e|(V_{\text{source}} - V_{\text{decel}})$ is calculated from the selected source energy and the output of the high voltage supply.

As a final check on the effect of the FC current drop off (arising from increasing V_{decel}) on measured cross sections, the cross section for the Ar^+-Ar reaction was measured and compared to the results from the MGC (Ref. [61]). To accomplish this, the region 1 - 5 keV was broken into two regions (1 - 3 keV, 3 - 5 keV), and the measurements were taken in two passes. First, the 1 - 3 keV measurements were accomplished by generating beams of 3 keV Ar^+ and using the deceleration voltage to sweep from $0 \rightarrow 2$ keV in V_{decel}, i.e. $E_{\text{ion}} = 3 \rightarrow 1$ keV. Similarly, the 3 - 5 keV band was measured via a decelerated 5 keV beam. The measurements were repeated 4 times following the procedure discussed previously and the resulting cross sections are shown in Fig. 2.23 with a -50 eV offset for clarity. In calculating the cross sections, we have used the same path length as the MGC and assumed a target gas temperature of 298 K.

As shown, the FGC cross sections beneath 4500 eV are in agreement with the
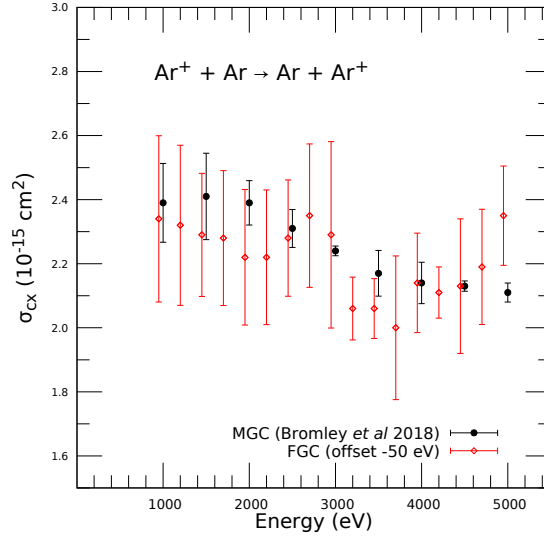
Figure 2.23 A comparison of the Ar$^+$-Ar charge exchange cross section from the MGC (Reprinted from Ref. [61]) and the FGC (present work, offset -50 eV).

MGC results within the error bars. On average, the statistical error bars in the FGC ($\sim$ 9%) are nearly twice as large as the MGC design ($\sim$ 5%). The use of 1 mm apertures in both the faceplate and skimmer decrease the beam current significantly compared to the MGC design ($I_o^{MGC} \sim$ 10–60 nA, $I_o^{FGC} \sim$ 2–10 nA, depending on ion source pressure and beam energy), and the smaller beam currents lead to larger scatter in the Faraday cup current measurements [63]. The systematic uncertainty is estimated to be the same as the original MGC design, $\pm$17% [61].

The effect of the knife edge apertures on the measured cross sections is not yet clear, and measurements must be made with a cylindrical set of apertures. Additionally, the effect of the knife-edge apertures on the path length is not yet understood. Reverting the faceplate and skimmer apertures to their original sizes (2, 3 mm) would increase the measured beam currents and reduce the statistical uncertainties in the measured cross sections. Such a change would also solidify confidence in the path length and shed light on the effect of different apertures shapes on the RFA curves of

decelerated ion beams.

In summary, the FGC design offers significant advantages over the traditional MGC design. With the MGC, one experimental set (consisting of 10 energies each) spanning either 0.2 - 1.0 keV or 1.0 - 5.0 keV, took 3 h due to the long pumping times (up to 2 h) and the measurement duration (1 h). With the FGC design, one experimental set, spanning 2 keV in E, may be accomplished in 0.5 h, and thus a single reaction may be measured from 0.2 - 5.0 keV within 8 h (breaking the energy range in 2 - 3 sections and performing each four times). At present, the achievable energies from a low source energy are limited to several hundred eV. However, adjusting the apertures as previously discussed may bring even lower energies within reach. Equipped with a set of skimmers without knife edges at the original aperture dimensions (2, 3 mm), the FGC design is expected to outperform the MGC design in both measurement duration and repeatability. Lastly, the total measurement duration can be further reduced by using a 0 - 5 kV voltage source, and the entire 0.2 - 5.0 keV energy range could be accessed and measured with a single 5 keV source beam.

Chapter 3

Gas Jet Designs for Crossed-Beam Experiments

3.1 Introduction

Recall the expression for charge exchange from Chapter 2, Eq. 2.1:

$$A^{q+} + B \rightarrow A^{*(q-j)+} + B^j \rightarrow A^{(q-j)+} + B^j + \gamma \tag{3.1}$$
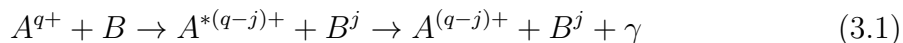
where the charge exchange process with multicharged ions may produce one or more photons, γ. In a gas cell, such as those discussed in Chapter 2, the optical access to the interaction region is restricted by the geometry of the cell. Any additional open apertures into the cell body, for e.g. an x-ray spectrometer, would increase the gas leakage into the chamber and affect the ion beam before it enters the collision region. While the cell could be equipped with a window, this introduces significant mechanical challenges including alignment, use of UHV-compatible materials, and poor solid angle coverage. An alternative to a gas cell is a gas jet, sometimes referred

to as a neutral beam/jet or molecular beam, which offers several unique advantages.
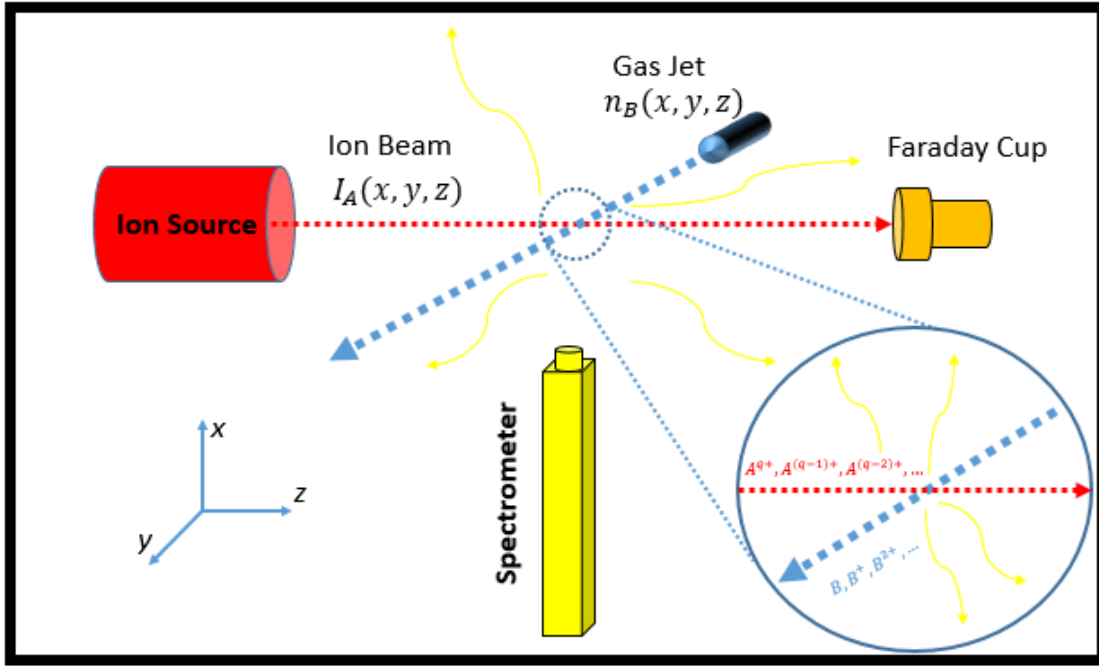
Figure 3.1 A schematic of a crossed-beam experiment utilizing a multicharged ion beam (red) and gaseous neutral jet (blue).

An example of a crossed-beam experiment utilizing a gas jet is shown in Fig. 3.1. As shown, a crossed-beam experiment utilizing a neutral jet provides significant optical access to the collision region. For processes with well-known total cross sections, the line intensities for each post-CX radiative channel may be assigned an absolute cross section as some appropriately weighted fraction of the total cross section. In many crossed-beam experiments, such as those in Ref. [97], the density of the jet is less well-characterized compared to a gas cell and the setup is used primarily to measure relative cross sections for each emission pathway. Compared to a gas cell, the access to the collision region when using a gas jet also allows for easy extraction of the slow ions produced from charge exchange. In many cases, a small and well-defined collision region is desirable for extracting slow collision products.

This is particularly useful for CX where the differential cross section may exhibit a strong angular dependence in both the scattering of the primary beam [98] and the slow ions [41].

For many multicharged ions the absolute cross sections for various targets and single charge transfer for individual charge states is not known, and placing the cross sections for individual emission lines on an absolute scale is difficult. A gas cell, such as the Manipulator Gas Cell in Chapter 2, may be used to first measure the absolute, total cross section for each pair of initial and final charge states (i, j) in Eq. 3.1. A gas jet may then be used to measure the relative contribution of each CX channel to the total cross section by weighting the individual channels by the observed photon counts for each channel. While directly measuring *absolute* charge exchange cross sections with a gas jet is possible, it carries some disadvantages compared to a gas cell. In a crossed-beam experiment, both the jet and ion beam are of similar size ($\sim$ millimeters), and precise alignment is difficult. Additionally, the density in the jet may not be well-known or easily measured, and calculating the effective path length requires knowledge of the 3-dimensional density distributions of both the gas jet and ion beam.

The principles behind the operation of a gas jet are well described in the text "Atomic and Molecular Beam Methods" (1988) by Giacinto Scoles [99], and the following discussion follows from there. A gas jet is produced by a supersonic expansion from a high-pressure gas reservoir into a low-pressure environment. Figure 3.2 shows the structure of such a jet during operation. The initial conditions behind the nozzle are the stagnation state, defined by the pressure and temperature (p_o, T_o). The pressure difference between the stagnation state and the surrounding chamber, $p_o - p_b$, accelerates the gas toward the exit of a converging nozzle. When the ratio p_o/p_b exceeds the value $G = (\frac{\gamma+1}{2})^{\gamma/(\gamma-1)}$, which is less than 2.1, the mean velocity of the
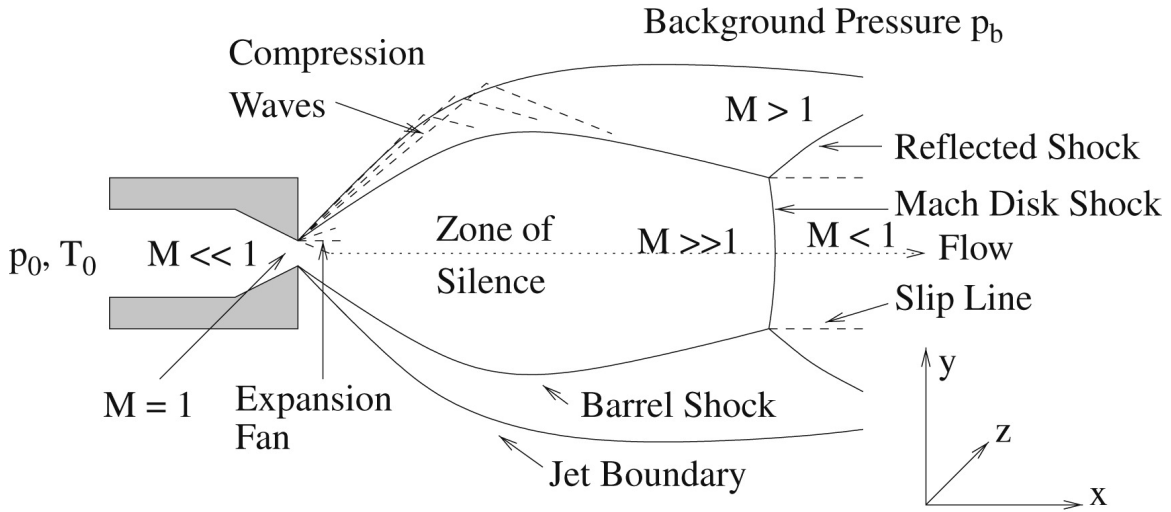
Figure 3.2 Reprint from Ref. [100]'s high-resolution version of a free jet expansion in [99].

gas is equal to the local speed of sound [99]. The Mach number, M, is defined as the ratio between the speed of the gas and the local speed of sound

$$M = v/v_s \tag{3.2}$$

which is equal to 1 at the exit of the nozzle. As the gas expands into the volume defined by p_b, the gas accelerates and the Mach number increases accordingly. This expansion is isentropic, that is, adiabatic and reversible. As the beam expands into the "zone of silence" in Fig. 3.2, called so because the jet particles are traveling faster than the speed of sound, i.e. the speed at which the influence of the chamber conditions propagate, the gas cools and approaches 98% of its final velocity within several nozzle diameters for most gases [99]. Downstream from the nozzle, a Mach Disk and corresponding shock structure is formed, and the location of the disk is relatively insensitive to the choice of gas. The location of the disk instead depends

67

on the geometry of the nozzle and skimmer and the two pressures p_o and p_b [99]:

$$\frac{x_M}{d} = 0.67 \left(\frac{p_o}{p_b} \right)^{1/2} \tag{3.3}$$

where x_M is the location of the mach disk as measured from the nozzle exit and d is the diameter of the nozzle opening. For gas jets in crossed-beam experiments, the mach disk and shock structure are prevented from forming by placing a skimmer at a distance less than the value of x_M from the end of the nozzle [99].

For many experiments, it may be useful to know the properties of the jet, such as the pressure $p(x, y, z)$, temperature $T = (T_\parallel, T_\perp)$, and the parallel and transverse velocities $\vec{v} = (v_\parallel, v_\perp)$. These parameters are estimated by a simple model by Schmidt et al. [101], and the derivation is based on the thermodynamics of an expanding ideal gas. In the following, we outline the simple model by Schmidt et al. Assume an ideal gas such that $p = nk_BT$ and $\gamma = \frac{C_P}{C_V} = 5/3$. Assuming changes in p, n, T are quasistatic and adiabatic and the gas expands due to a pressure gradiant along z, the following conditions hold [101]:

$$\frac{dn}{n} = \frac{3}{5}\frac{dp}{p} \tag{3.4a}$$

$$d(nAv) = 0 \tag{3.4b}$$

$$\frac{dv}{dt}Mn = -\frac{dp}{dz} \tag{3.4c}$$

$$\frac{dp}{p} = \frac{5}{2}\frac{dT}{T} \tag{3.4d}$$

Substituting $p = nk_BT$ into Eq. 3.4c and combining Eqns. 3.4a and 3.4b, we

find

$$\frac{dp}{p} = -v\frac{M}{k_B T}dv \tag{3.5a}$$

$$\frac{dp}{p} = -\frac{5}{3}\left(\frac{dv}{v} + \frac{dA}{A}\right) \tag{3.5b}$$

which together may be written [101]

$$\left(\left(\frac{v}{v_s}\right)^2 - 1\right)\frac{dv}{v} = \frac{dA}{A} \tag{3.6}$$

where the speed of sound v_s is defined as

$$v_s = \sqrt{\frac{5}{3}\frac{k_B T}{M}} \tag{3.7}$$

As discussed previously, for $p_o/p_b > 2.1$ the velocity of the gas at the exit of the nozzle is equal to the speed of sound, and hence $v_{nozzle} \equiv v_s$. To calculate the temperature, and thus the velocity at the nozzle exit we combine Eqns. 3.4d and 3.5a to find

$$dT = -\frac{2}{5}Mk_B v dv \tag{3.8}$$

Integrating and assuming the velocity of the jet is much greater than the velocity of the gas at the stagnation pressure p_o we find

$$T_{nozzle} - T_o = -\frac{2}{5}\frac{M}{k_B}\int_{v_o}^{v_{nozzle}} vdv = -\frac{M}{5k_B}v_{nozzle}^2 \tag{3.9}$$

which from Eq. 3.7 yields $T_{nozzle} = \frac{3}{4}T_o$. For a quasistatic, adiabatic process the quantity $P^{1-\gamma}T^\gamma \equiv$ const., and thus the number density and pressure at the exit of

the nozzle follow for $\gamma = 5/3$:

$$n_{nozzle} = \frac{3\sqrt{3}}{8}n_o \tag{3.10a}$$

$$p_{nozzle} = \frac{9\sqrt{3}}{32}p_o \tag{3.10b}$$

The number of particles per second leaving the nozzle is then simply

$$N_{nozzle} = (vnA)|_{nozzle} = \frac{3p_o A_{nozzle}}{16}\sqrt{\frac{15}{k_B T_o M}} \tag{3.11}$$

We are now equipped to derive the velocity and the thermodynamic properties of the jet as a function of radial distance away from the jet, or more appropriately the 'area' of the jet at a given distance z. From Eq. 3.9 we have $T = T_o - v^2\left(\frac{M}{5k_B}\right)$, from which the local speed of sound v_{ls} follows as $v_{ls}^2 = v_s^2 - \frac{v^2}{3}$ [101]. By substituting $x = v/v_s$, Schmidt et $al.$ derive the following. Integrating Eq. 3.6 from A to A_{nozzle} we have

$$\int_{A_{nozzle}}^{A} \frac{dA}{A} = \int_{x_{\text{nozzle}}}^{x} \left(\frac{x}{1 - x^2/3} - \frac{1}{x}\right) dx \tag{3.12}$$

Here x_{nozzle} is defined by $v_{\text{nozzle}}/v(p_o, T_o) = \sqrt{3}/2$. Integration yields

$$\frac{A}{A_{\text{nozzle}}} = \frac{9}{16x(1 - x^2/3)^{3/2}} \tag{3.13}$$

For $A/A_{\text{nozzle}} \gg 1$, $x \sim \sqrt{3}$ and the velocity simplifies to

$$v_{\text{jet}} = \sqrt{3}v_s = \sqrt{\frac{5k_B T_o}{M}} \tag{3.14}$$

Eq. 3.14 was confirmed to be correct for monoatomic ideal gases [102]. Lastly,

using the relations $T = T_o - v^2(M/5k_B)$, $P^{1-\gamma}T^\gamma = \text{const.}$, and Eq. 3.13 we arrive at the (longitudinal) temperature, density, and pressure of the jet as a function of cross-sectional area A:

$$\frac{T}{T_o} = \left(\frac{3\sqrt{3}}{16}\frac{A_{\text{nozzle}}}{A}\right)^{2/3} \tag{3.15a}$$

$$\frac{n}{n_o} = \frac{3\sqrt{3}}{16}\frac{A_{\text{nozzle}}}{A} \tag{3.15b}$$

$$\frac{P}{P_o} = \left(\frac{3\sqrt{3}}{16}\frac{A_{\text{nozzle}}}{A}\right)^{5/3} \tag{3.15c}$$

The above relations are valid for $A_{\text{beam}} > A_{\text{nozzle}}$ but only while the pressure within the jet is high enough such that collisions maintain quasi-staticity. Inside the nozzle, random thermal energy is converted into directed kinetic energy, and the transverse temperature is much less than the longitudinal component. However, both n and p will continue to decrease as the gas expands. Using the derived relations for the density n and the pressure p of the jet, Schmidt *et al.* derive a final expression for the on-axis jet density as a function of distance along the z axis. They write the density as

$$n(0,0,z) = \frac{\eta^{\delta r}(z)N_{nozzle}}{v_{jet}\pi\delta r^2} \tag{3.16}$$

where δr is the radius of a small disk on the z-axis a distance z from the nozzle. The quantity $\eta^{\delta r}(z)$ is the probability for an atom leaving the nozzle to pass through an area (oriented perpendicular to the skimmer) with radius δr, and for $z \gg \delta r$ takes the form

$$\eta^{\delta r}(z) = \frac{\delta r^2}{z^2}\chi \tag{3.17}$$

Assuming a three-dimensional Maxwellian velocity distribution of temperature

71

T_{nozzle} at the exit of the nozzle, the numerical factor χ is evaluated by integrating the velocity distribution over the cone in velocity space defined by the disc of radius δr [101]. Let us assume the nozzle and skimmer are separated by a distance L. The minimum time to traverse a distance δr off-axis is given by $t = L/v_{jet}$, and for a given L we may write both the maximum allowed transverse velocity and the numerical factor χ as

$$v_{\perp}^{max} = \frac{\delta r}{L} v_{\text{jet}} \tag{3.18}$$

$$\chi = \int f(v)dv^2 = 2 \int_0^{v_{\perp}^{\text{max}}} \left(\frac{m}{2\pi k_B T}\right) exp\left[\frac{-mv}{2k_B T}\right] v dv \tag{3.19}$$

The effective divergence angle of the beam, α, is given by $\tan(\alpha) = \chi^{-1/2}$ [101]. The cross-sectional area of the jet at a given z follows as $A(z) = \pi z^2 (\tan^2 \alpha)$. Using Eqns. 3.15a - 3.15c, we have an estimate of the density, pressure, and temperature of the beam as a function of z and distance from the jet axis. From Eq. 3.18, the maximum allowed transverse velocity for the nozzle-skimmer geometry may be used to estimate the upper limit of the transverse temperature. Assuming the velocities are distributed such that 2 d.o.f $\times (\frac{1}{2} k_B T_{nozzle}) = mv_{\perp}^2$, the upper limit of the transverse temperature becomes $T_{\text{max}}^{\perp} = \frac{m(v_{\perp}^{\text{max}})^2}{k_B T}$. Lastly, using the expressions for N_{nozzle} and v_{jet}, the on-axis density may be written in terms of the stagnation pressure, nozzle area, and distance along the z axis:

$$n(0,0,z) = n_o \frac{3\sqrt{3}}{16} \frac{A_{\text{nozzle}}}{\pi z^2} \chi \tag{3.20}$$

To summarize, the model from Schmidt *et al.* [101] assumes the gas from a reservoir, defined by p_o and T_o, is accelerated in a converging nozzle by a pressure

72

gradient along the z axis. From the stagnation state in the gas reservoir (p_o, T_o), the longitudinal velocity of the jet particles, v_{jet}, may be calculated. The on-axis density is given as a function of distance from the nozzle, z, in Eq. 3.20, and the off-axis density (Eq. 3.15b) and pressure (Eq. 3.15c) are calculated by assuming a quasi-static, adiabatic expansion of the gas. The temperature along z is defined by Eq. 3.15a [101]. For crossed-beam experiments where the neutral and ion beams intersect at 90°, the most important temperature is the transverse temperature. An upper limit on the transverse temperature is derived by considering the maximum allowed transverse velocity that would make it through each skimmer in the expanding gas jet.

While several approximations are made in their derivation, Schmidt *et al.*'s model is sufficient for discussing the operation of a gas jet as a function of the geometry and nozzle parameters p_o and T_o. In the following sections, the model is applied to the design of two gas jet sources. The first jet features a small, compact design intended for loading gaseous targets into an Electron Beam Ion Trap or similar ion source. In particular, such a jet would be useful for loading volatile organic compounds (VOCs) into the Clemson University Electron Beam Ion Trap.

This technique, called Metal Ions from Voltatile Compounds (MIVOC), has proven successful for both Electron Cyclotron Resonance (ECR) ion sources [103] and EBITs [104]. These volatile compounds are metal-containing compounds, for example ferrocene (chemical formula $\text{Fe}(\text{C}_5\text{H}_5)_2$), with relatively high vapour pressures. With some heating, the materials readily sublimate and may be injected by a ballistic or supersonic jet into an ion source. Loading metal atoms into an EBIT in this manner is an alternative to schemes where ions are injected from an external ion source. A neutral jet containing the element of interest allows for continuous gas injection as the gas can drift into the drift-tube region. However, such an injection system must be carefully constructed to limit the effect on the background pressure, and ultimately

the charge state balance, within the trap.

A second, high-pressure design is proposed for crossed-beam experiments downstream from CUEBIT (see Ch. 1). The operational requirements of this jet are used to motivate the proposed design, and the expected jet behavior is characterized with the model of Schmidt *et al.* [101]. A Python code for calculating jet conditions (density, temperature, velocity, etc.) using the model of Schmidt *et al.* is provided in Appendix A. SOLIDWORKS drawings of both the low and high pressure jet components are provided in Appendices B and C.

3.2 Design and Benchmarking of a Low-Pressure Gas Jet for Loading Metals into CUEBIT

As discussed previously, it is necessary for gas injection into CUEBIT to have a minimal effect on the background pressure. To that end the gas injection system should consist of a cold, collimated neutral beam directed into the drift tube region. To start, we may estimate the required neutral density to produce sufficient numbers of ions for a crossed-beam experiment downstream. Assuming a nominal ion beam current of 0.1 nA of a single charge state, the required ion number (per second) produced in the source (assuming minimal losses en-route to the crossed-beam chamber), goes as $N_{\text{ion}} = \frac{I_i}{q|e|}$. For most elements of interest, the ion charge q is order of 10. This yields an ion number in the trap at a given time of 6×10^7. Within the trap, the number of ions produced per second is approximately

$$N_{\text{ion}} \approx \frac{n_o \sigma_{\text{EII}} j_e V_{\text{overlap}}}{|e|} \tag{3.21}$$

where n_o is the neutral density in the trap, σ_{EII} is the cross section for electron

impact ionization of the relevant species, j_e is the current density of the electron beam, V_overlap is the overlap volume of the neutral and electron beams, and e is the elementary charge. Assuming σ_EII is of order 10^{-16} cm^2, a nominal electron beam current of 100 mA with a beam radius of 200 μm [40], and the overlap region is the size of the electron beam, the required neutral density is of order 10^-7 - 10^8 cm^{-3}. Such low densities are certainly achievable. Additionally, the trapping produced by the electron beam and the gyrofrequency of the electron beam ensures that more than one collision is possible as the electrons traverse the neutral gas. Thus we will consider this density as a soft requirement of our low-pressure jet design.

As discussed in Sec. 3.1, the profile of the jet is determined by the physical geometry of the nozzle/skimmer and the stagnation state (p_o, T_o) in the gas reservoir. While commercial nozzle/skimmers are viable, efforts were undertaken to machine the bulk of the jet system in-house. A nozzle and a skimmer were drawn up and machined from aluminum by the Clemson University Physics and Astronomy Instrumentation shop. A schematic of the nozzle is shown in Fig. 3.3. The diameter D of the central bore measures 0.014" for the nozzle and 0.024" for the skimmer. The nozzle and skimmer bores are surrounded by a 0.02" flat that is required to ensure the drill bit does not tear the tip of the work. The exterior angles of the two pieces measure 100°, and the thick walls create an interior angle of 9°. For stagnation pressures of order 1 mbar, nozzle diameter 0.014" and background pressures of order 10^{-4} mbar, the expected Mach disk location from Eq. 3.3 is 0.94". To constrain the transverse gas temperature to a few mK and reduce the divergence of the neutral beam, a separation between the nozzle and skimmer of 0.57" was chosen.

A schematic of the nozzle and skimmer assembly inside of a 2-3/4" CF cross is shown in Fig. 3.4. The jet and its housing are broken up into four sections that are discussed in order. In Section 1 (yellow), the gas reservoir is maintained inside
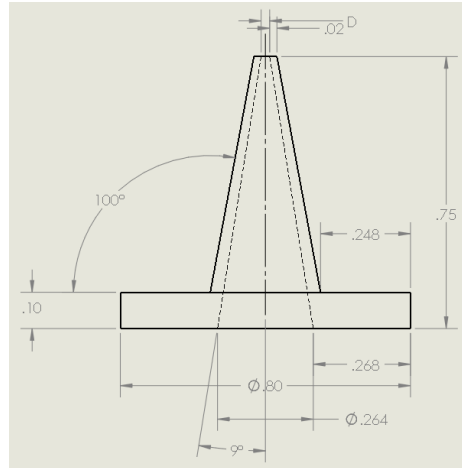
Figure 3.3 A SOLIDWORKS drawing for the nozzle and skimmer.

of a 1.33" CF 3-way flange. On the left side of the 1.33" CF 3-way, gas is injected via a digitally controlled UHV leak valve. At the rear of the leak valve, tubing from a gas canister or heated volatile holder connects to the valve, and the gas reservoir pressure is controlled by an interfaced Python code. The stagnation pressure p_o is measured in the gas reservoir by a Pfeiffer Pirani gauge, and the third connection attaches to the 2-3/4"-to-1.33" zero-length CF reducer in Section 2 (red). On the vacuum side, a 1/4" Swagelok connector (part SS-400-R-4 with tubing removed) is welded to a stainless steel plate which bolts to the reducer. A 2.3" length of 1/4" OD oxygen free high purity copper tubing then connects the Swagelok connector at the gas reservoir to the Swagelok connector at the nozzle mount in Section 3 (yellow). The nozzle described above is held between the Swagelok plate and the cyclindrical nozzle mount. The recess for the brim of the nozzle is machined to an incredibly close fit (0.005") with the nozzle. A cyclindrical holder, shown in Section 4 (green), holds the nozzle and the skimmer such that the nozzle and skimmer central bores are 0.57" apart as discussed previously. The nozzle/skimmer mount is machined with slots to prevent gas buildup between the nozzle and skimmer. Lastly, at the right
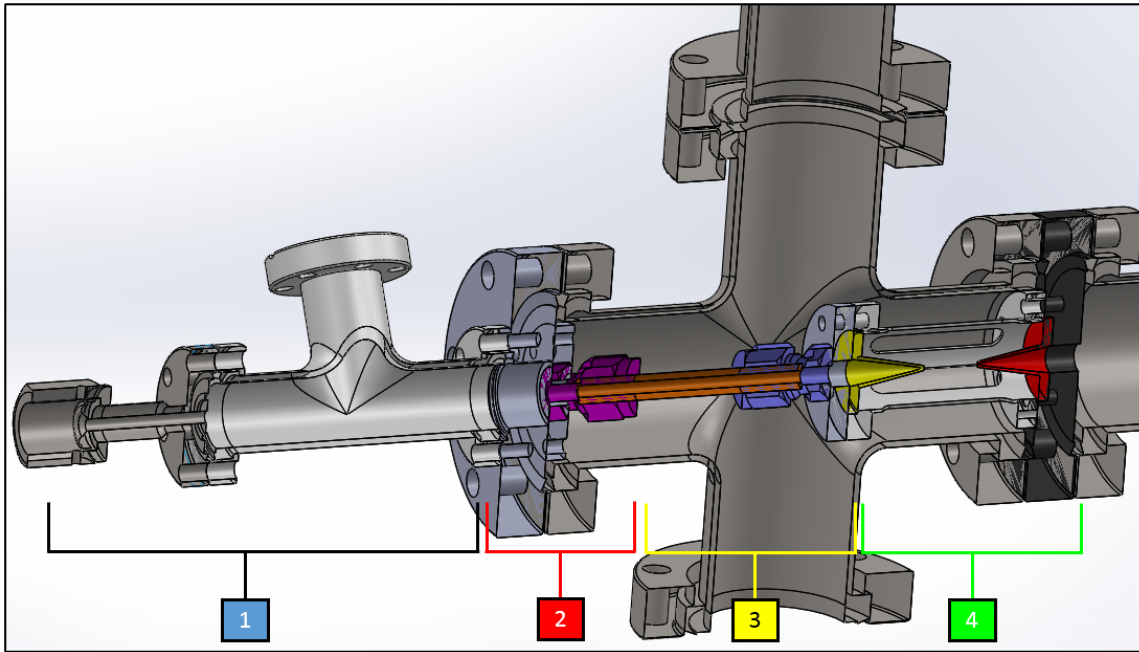
Figure 3.4 A SOLIDWORKS assembly of the nozzle and skimmer system mounted inside of 2-3/4" CF crosses. The four sections are labeled: 1) Gas injection (yellow), 2) nozzle-to-reservoir connection (red), 3) nozzle mount (yellow), and 4) skimmer mount (green).

side of Section 4 the nozzle/skimmer bolts to a double-sided CF flange (black). A small recess is machined into the double sided flange for a close fit (within a few 0.001") with the skimmer, which is held in place by the nozzle mount. At the top and bottom of the cross, a pressure gauge and turbo pump (not shown) complete the gas jet assembly.

An initial test of the jet was conducted by measuring the pressures in the section immediately around the nozzle and a 'dump' chamber downstream. A schematic of the test setup is shown in Fig. 3.5. The test chamber consists of three parts denoted by the conductances C_1, C_2, and C_3. The nozzle chamber, denoted by C_1, is the 2-3/4" CF cross housing the jet in Fig. 3.4 and is connected to a turbo pump (Varian/Agilent TurboVac #333810, $S = 80$ L/s) and a full-range cold-cathode gauge
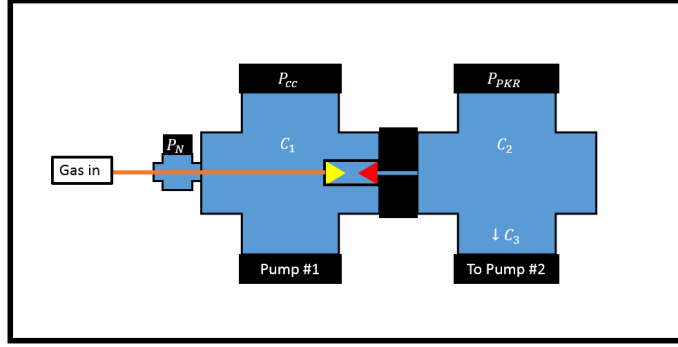
Figure 3.5 A schematic (not to scale) of the test chamber used for the low pressure gas jet including the nozzle (yellow) and skimmer (red). Three pressure gauges are shown: the stagnation pressure (P_N), the chamber immediately around the nozzle/skimmer system (P_{cc}), and the downstream 'jet dump' gauge (P_{PKR}). Pump #1 is connected directly to the chamber, and long flexible tubing (C_3) connects pump #2 to the jet dump. The three conductances considered in the testing of the jet are shown as C_1, C_2, and C_3.

(P_{cc}). Assuming the gas leakage through the skimmer at base pressure is negligible, the effective pumping speed S_e of the first section may calculated via [105]:

$$\frac{1}{S_e} = \frac{1}{S_1} + \frac{1}{C_1} \tag{3.22}$$

and for the $C_1 = 56.5$ L/s (stated by the manufacturer) and $S_1 = 80$ L/s we find an effective pumping speed $S_e = 33.1$ L/s. The jet dump is connected to the nozzle housing by a double sided flange with a hole through which the jet exits the skimmer. The dump chamber (C_2) consists of two 2-3/4" CF crosses connected in series and contains a pressure gauge (P_{PKR}) and a turbo pump (Pfeiffer HiPace 80, $S = 67$ L/s) connected by approximately 1.4" wide by 25" long flexible stainless steel tubing. The conductance of this tubing C_3 may be calculated from the expression for the conductance of long thin tubes [105]:

$$C_{tube} = 12.1 \times \frac{d^3}{l} \text{ [L/s]} \tag{3.23}$$

78

where both the diameter d and the length l are in cm. This expression is an *upper limit* of the conductance as the tubing is bent to allow connection to the turbo pump. Using the above dimensions the upper limit of the conductance of the long flexible tubing is 8.6 L/s. Adding the conductances of the two CF crosses and the long tubing in series

$$\frac{1}{C_{\text{dump}}} = \frac{1}{C_2} + \frac{1}{C_2} + \frac{1}{C_3} \tag{3.24}$$

yields $C_{\text{dump}} = 6.6$ L/s and an effective pumping speed of the jet dump of 6.0 L/s.

Lastly, we must also consider the flow of background gas through the skimmer. The skimmer may be approximated as an orifice as any gas making it through the skimmer will not scatter out of the jet dump. The conductance C_{skim} may be written [105]:

$$C_{\text{skim}} = A_{\text{skim}}\sqrt{\frac{k_B T_T}{2\pi M}} \tag{3.25}$$

where our test gas N_2 yields $C_{\text{skim}} = 0.05$ L/s. Given the scale of this conductance value compared to the conductances of the nozzle chamber C_1 and the jet dump $C_2 + C_3$, we ignore gas flow driven by the pressure differential $P_{\text{cc}} - P_{\text{PKR}}$ through the skimmer.

During operation of the jet, the total throughput into the system, Q_{gas} may be expressed as

$$Q_{\text{gas}} = Q_{\text{nozzle}} + Q_{\text{dump}} = S_{\text{e1}}\Delta P_{\text{cc}} + S_{\text{e2}}\Delta P_{\text{PKR}} \tag{3.26}$$

where S_{e1} is the effective pumping speed of the nozzle chamber, denoted by C_1 in Fig. 3.5, S_{e2} is the effective pumping speed of the jet dump, and P_{cc} and P_{PKR} are the pressures in the respective sections. Within each section, the pressure will increase in accordance with the gas flow and the effective pumping speeds within the section.
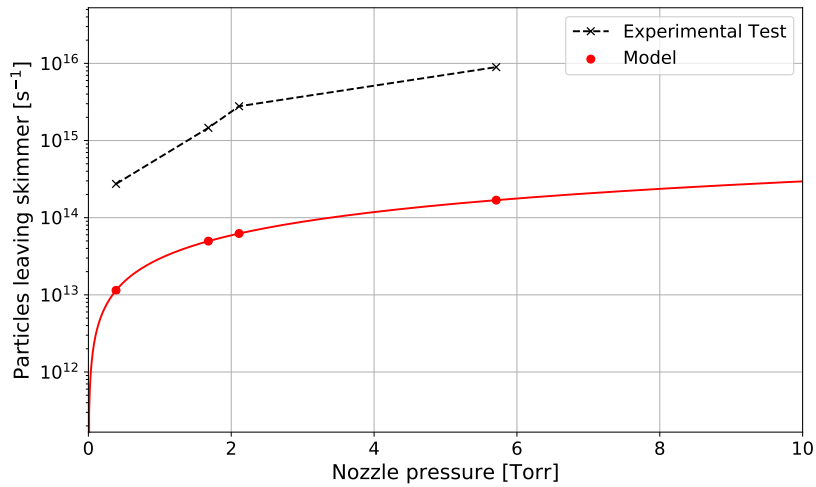
Figure 3.6 Pressure test of the low pressure gas jet. The number of particles per second exiting the skimmer is calculated from the increases in pressure inside nozzle and jet dump chambers. The expected number from Schmidt. *et al.* (Ref. [101]) is shown as a solid red line.

In the nozzle chamber, the gas load will be high due to the skimming of the majority of the jet particles. By measuring changes in pressure, ΔP during the operation, the gas load and the number of particles entering the jet dump may be calculated as a function of the nozzle pressure P_N as measured by a Pirani gauge.

Fig. 3.6 shows the result of such a test. Due to the available pumps, the maximum (safe) nozzle pressure is around 6 mbar. In theory the jet backing pressure could be increased considerably if a larger pump was added in parallel or as a replacement to the nozzle chamber pump. The model by Schmidt *et al.*, plotted as the solid red line above, is shown plotted at each of the nozzle pressures used in the experimental test. This model underestimates the number of jet particles entering the dump region by a factor of $\sim$37 on average. This is not unexpected as the number of particles entering the skimmer depends upon the upper limit of the transverse temperature. If the transverse temperature is lower than expected, the number of particles entering

80

the jet would be greater. Additionally, the calculations of the conductance values are approximations, and overestimations of the effective pump speeds would inflate the calculations of the jet and background contributions.

Though there is a discrepancy between the measured and expected number of particles in the jet, we may use the model of Schmidt *et al.* [101] to estimate the relevant thermodynamic properties. For an N_2 (m $= 4.65 \times 10^{-26}$ kg) reservoir at $P_o = 7$ mbar, $T_o = 300$ K, the following properties are expected. Within several nozzle diameters along z the particles reach a terminal velocity of 667 m/s. Using Eq. 3.18, the upper limit of the transverse velocity (14 m/s) provides an upper limit of the transverse temperature at 2.2 mK. Using these operating conditions, the expected neutral density at a location 16" away on-axis (the expected skimmer-to-drift-tube distance) is $n(z = 16'') = 5 \times 10^5$ cm^{-3}. If a larger pump were to replace Pump #1 in Fig. 3.5 and the nozzle pressure were raised to 100 mbar, the estimated neutral density is raised to 6×10^6 cm^{-3}. Such a jet would achieve a neutral density within a factor of 2 of the 'soft' density target of 10^7 cm^{-3}. Given the increase in ionization efficiency from the gyrofrequency of the EBIT electron beam within the trap, such a jet would be sufficient for loading gases into the drift tube region of CUEBIT.

3.3 Developing A High-Pressure Gas Jet Design for Crossed-Beam Experiments With Highly Charged Solar Wind Ions

The second jet design is intended for performing charge exchange measurements in a crossed-beam setup downstream from the CUEBIT source. This high pressure jet is optimized for the Cold Target Recoil Ion Momentum Spectroscopy

(COLTRIMS) experiment discussed in Ch. 1. From crossed HCI and neutral beams, the number of charge exchange events per second (R) may be approximated by [42]:

$$R = \sigma_{\text{cx}} \rho_{\text{n}} \rho_{\text{i}} v_{\text{ion}} V_{\text{overlap}} \zeta \qquad (3.27)$$

where σ_{cx} is the charge exchange cross section, ρ_{n} is the neutral density, ρ_{i} is the ion density, v_{ion} is the ion velocity, V_{overlap} is the overlap volume between the HCI and neutral beams, and ζ is a geometrical factor. The ion density is calculated as $\rho_{\text{i}} = I_{\text{i}}/q e v_{\text{ion}} r^2$ where I_{i} is the beam current, q is the ion charge state, e is the electron charge, v_{ion} is the ion velocity, and r is the ion beam radius. Assuming typical operating conditions ($I = 100$ pA, $r = 1$ mm, $q = 8$), $\sigma_{\text{cx}} = 10^{-15}$ cm^2, $\zeta = 1$ and $V = 5$ mm^3 we find that the minimum counts to operate the spectrometer (≈ 1 count pixel^{-1}s^{-1}) requires a neutral density of $\rho_{\text{n}} = 10^{11}$ cm^{-3} [42]. However, given that the charge exchange cross section scales with the charge state [25, 26], the required neutral density is reduced to 10^{10} cm^{-3}. Therefore we will consider $n_o(\text{z}_{\text{int}}) = 10^{10}$ cm^{-3} as the lower bound of the jet density at the intersection of the jet and ion beam.

Consider the application of the low-pressure gas jet (Sec. 3.2) to a COLTRIMS type setup. When mounted on a 6" CF cross, the interaction region at the center of the cross (7" from the skimmer) would experience a neutral density of order 10^6 cm^{-3} and $T_\perp \sim 2$ mK. While the temperature is sufficient, the neutral density is a factor of 10^4 too small.

A simple solution would be to move the nozzle and skimmer closer to the interaction region to combat the $1/z^2$ density drop-off. Moving the exit of the skimmer 2" from the interaction region, the on-axis neutral density is raised to 3×10^7 cm^{-3}. With this new geometry and raising the pressure to 0.5 bar, the density increases
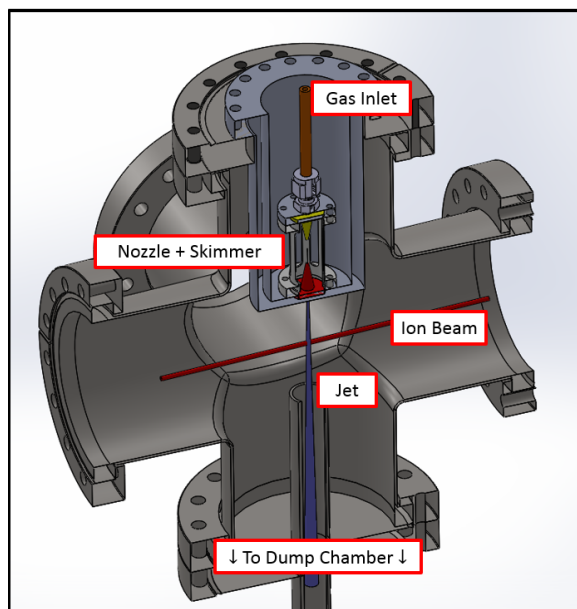
Figure 3.7 SOLIDWORKS Assembly of the high pressure gas jet. A representation of the ion beam (red) and gas jet (purple) are shown.

to 2×10^9 cm^{-3}. While it is possible to move the jet closer (1" separation $\rightarrow 8 \times 10^9$ cm^{-3}), this may interfere with the electrodes for extracting post-CX slow ions in the COLTRIMS measurements. Instead, we may increase the transverse temperature for the sake of density. Reducing the nozzle-skimmer separation from 0.57" to 0.25" and keeping the same nozzle and skimmer diameters, 0.014" and 0.024" respectively, the upper limit of the transverse temperature is raised to 11 mK. However, the density at the interaction region is raised to $n(2'') = 2.5 \times 10^{10}$ cm^{-3}.

Using the same 2-3/4" construction as the low-pressure jet and raising the backing pressure to nearly 500 mbar, any turbo pump would likely be overwhelmed. Instead, the nozzle-and-skimmer system is modified to fit inside a 6" 6-way CF cross. This change requires that the nozzle-skimmer system be mounted in a sealed extension to reduce the ion-skimmer separation to 2". Lastly, an appropriately shaped jet dump must capture the jet particles after they traverse the interaction region.

Fig. 3.7 shows a cross-sectional view of the SOLIDWORKS assembly of this new design. Many of the components may be repurposed from the design of the low-pressure jet (Fig. 3.4). The nozzle and skimmer are machined from aluminum with diameters 0.014" and 0.024" respectively. The nozzle-skimmer separation is set by the steel housing such that the apertures are 0.25" apart (fixed). This nozzle & skimmer housing rests inside a hollow stainless steel cylinder bolted to a custom 6" CF flange with a circular bore and bolt pattern. At the bottom of the cylinder, the skimmer rests inside a circular depression, and a small aperture (equal in diameter to the base of the skimmer) allows the jet particles into the beamline. Flexible stainless steel tubing (identical to those used in the MGC, Fig. 2.2) connects the copper tubing at the rear of the nozzle to a steel gas feed-through (not shown).

While this design limits the gas leakage from background gas floating around the nozzle chamber, each particle leaving the skimmer will increase the beamline pressure. To limit this effect, a 'jet dump' is designed such that any particle entering the dump is unlikely to scatter and re-enter the beamline. Consider the conductances of a small orifice (Eq. 3.25) and a long tube (Eq. 3.23). For a given (small) diameter, the conductance of a tube is signicantly smaller than an aperture. Using a tube of an appropriate diameter right below the gas jet, the majority of the jet particles will be captured and pumped away.

For the expected transverse temperature of 11 mK, the half-angle divergence of the jet is 1.5°. Assuming the skimmer-interaction distance is 2" and the interaction-dump distance is also 2", the size of the jet on the far side of the interaction region is only 0.22 in. (5.4 mm). To err on the side of caution and to combat possible misalignment of the jet and the dump, we adopt a diameter of the jet dump entrance of 3/4" (19 mm). Assuming that each particle passing through the skimmer enters the jet dump, the entirety of the jet represents a room temperature gas load of

5×10^{-5} mbar-L/s. For a 500 L/s turbo pump attached directly to the dump chamber, the chamber pressure will be 1×10^{-7} mbar. For a tube of diameter 19 mm and 203 mm (8") long connecting the dump and interaction chamber, the conductance is $C_{\text{tube}} = 4.2$ L/s. As the pressure in the beamline is significantly lower than the jet dump pressure, the resulting gas load on the beamline from leakage *out* of the jet dump is estimated at 4×10^{-7} mbar-L/s. A nominal pump speed at the interaction region of 30 L/s leads to an increase in beamline pressure during jet operation of 1×10^{-8} mbar. This pressure increase is comparable to the expected background pressure within the interaction region. Given that the pump speed in the dump and the effective pump speed in the interaction region will be larger, the gas load from the jet should have a minimal effect on the operation of the COLTRIMS setup.

To summarize, two gas jet designs were developed. The first design, the "low pressure gas jet," is intended to produce a cold neutral beam with densities between $10^6 - 10^8$ cm^{-3} to an interaction region 16" away from the jet skimmer. These densities are sufficient for loading metal-containing volatile organic compounds into CUEBIT with the purpose of producing metal HCI beams. The design is optimized for fitting inside standard 2-3/4" CF hardware, and operates via a digitally controlled leak valve. The performance of the jet was checked against a simple theoretical model by Schmidt *et al.* [101], and performance of the jet is consistent with the model behavior. The initial test estimates that the neutral densities produced by the system, backed by a 7 mbar gas reservoir, are on order $n(z_{\text{int}}) = 10^5 - 10^6$ cm^{-3}. Raising the pressure to produce the desired densities of $10^7 - 10^8$ cm^{-3} will require an additional turbo pump acting in parallel or as a replacement for the current pump.

A second gas jet design, the "high pressure gas jet," was presented for future COLTRIMS experiments downstream from the CUEBIT source. This design is intended to produce cold, dense neutral targets with densities of 10^{10} cm^{-3} within

several inches of the skimmer exit. The high pressure design was optimized for COLTRIMS-type measurements by modifying, as necessary, the design of the low pressure jet. The jet is produced by a nozzle and skimmer housed inside an extension that protrudes near the ion beam in a 6" CF cross. The design was optimized to provide the required transverse temperature for COLTRIMS-type measurements while retaining a modest pumping requirement. It is expected that these two designs will contribute to the production and use of metal HCI beams at CUEBIT.

Chapter 4

Gold Spectroscopy

As discussed in Ch. 1, measurements of the spectra of heavy elements are useful to both astrophysicists and atomic theorists. Laboratory measurements of emission lines and their intensities enable abundance studies in a variety of astrophysical environments. For atomic theorists, spectral measurements produce valuable benchmarks, e.g. line positions, energy levels, and oscillator strengths, for many atomic structure codes [59]. At Clemson University, a new collaboration with the University of Georgia, Queen's University Belfast, and Auburn University is exploring the spectra of lowly-charged heavy elements relevant to neutron star mergers. These elements include Re, Os, Ir, Pt, and Au.

Gold (Au) was chosen as the first element of study due to its simple (relative to Re, Os, Ir, and Pt) electronic structure. In this work, the spectra of Au I and II were observed at the Compact Toroidal Hybrid at Auburn University, and this chapter discusses the data collection, data analysis, and results of these experiments. In Sections 4.1 and 4.2, a brief discussion of the relevant background material is presented which largely relies on the text *Atomic Physics* by Dr. Chris Foot [64] and Chapter 4 from *Quantum Optics* by Dr. Mike Fox [106].

Section 4.3 provides a historical review of the available data for Au I and II. In Sec. 4.4 an overview of our experimental apparatus and procedure is provided. In Sec. 4.5 - 4.6, the data analysis is discussed, and the final results for Au I and II lines and levels are presented in Sec. 4.7 - 4.8. Where applicable, samples of the Python codes used to analyze the data are available in Appendix D. For access to the entirety of the data analysis codes, see the GitHub repository by clicking here.

4.1 Electronic Structure

In 1913 Bohr presented his model of the hydrogen atom. In an atom, electrons orbit a nucleus of protons and neutrons. For an electron orbiting a single proton, Bohr equated the force required for the centripetal acceleration experienced by the electron and the electrostatic force between the proton and electron:

$$\frac{mv^2}{r} = \frac{e^2}{4\pi\epsilon_o r^2} \tag{4.1}$$

Bohr assumed that the electron orbits are quantized, that is

$$mvr = n\hbar \tag{4.2}$$

where n is an integer. Using Eqn's. 4.1 and 4.2, we find $r = a_o n^2$, where $a_o = \hbar^2/(me^2/4\pi\epsilon_o)$ is the Bohr radius. For the electron orbiting a proton, the sum of the kinetic and potential energies of the electron is written

$$E = \frac{1}{2}mv^2 - \frac{e^2}{4\pi\epsilon_o r} \tag{4.3}$$

Using Eq. 4.3 and the expression for r above, we arrive at Bohr's energy levels

of hydrogen

$$E = -\frac{e^2/4\pi\epsilon_o}{2a_o}\frac{1}{n^2} \tag{4.4}$$

which agrees well with observed spectra of neutral hydrogen [64]. For heavier, hydrogen-like ions, $e \rightarrow eZ$, and the expression becomes

$$E = -\frac{Z^2 e^2/4\pi\epsilon_o}{2a_o}\frac{1}{n^2} \tag{4.5}$$

which is sufficient for explaining the gross structure of hydrogenic ions [64]. However, when the number of electrons is greater than 1, this expression is inadequate as the electrostatic interaction between the electrons is not considered in the derivation. Bohr's derivation largely ignores the quantum nature of the electron and the proton. For multi-electron systems, a different approach is required.

Let us consider the modern, quantum mechanical description of an atom. In an atom, the wave function of the electron obeys the Schrodinger Equation [64]

$$\left[\sum_i \frac{-\hbar^2}{2m}\nabla_i^2 + \sum_{i<j} V_{ij} + \sum_i V_{in}\right]\Psi = E\Psi \tag{4.6}$$

where the sum is over the number of electrons, V_{ij} is the electrostatic interaction between the electrons, and V_{in} is the electron-nucleus attraction for each electron [64]. For hydrogen, this equation may be solved analytically (see Ref. [64]) and the solution for each set of quantum numbers (n, l, m) is the product of a spherical harmonic $Y_{l,m}(\theta, \phi)$ and an associated Laguerre polynomial L_{n-l-1}^{2l+1}. For multi-electron systems, the wave function may be constructed from a linear combination of these hydrogenic functions $\psi = L_{n-l-1}^{2l+1} \times Y_{l,m}$, and the coefficients are calculated by approximations of the electron-electron repulsion terms [64].

For our purposes, the state of each electron, defined by the quantum numbers

(n, l, m), is labeled by a one-electron hydrogen-like orbital and the resulting structure is a called a *configuration*, e.g $2s2p, 2s3p$, and so on. For light atoms, the potential V_{ii} may be separated into two contributions: the central field, $V_{\mathrm{CF}}(r)$, which is the average potential generated by all of the electrons, and the residual electrostatic interaction V_{re} that is not represented by the central field. When the residual electrostatic interaction is small compared to the central field, V_{re} acts as a small perturbation.

The repulsion between the valence electrons (represented by the perturbation V_{re}) causes each electrons' orbital angular momentum to change. Both the total momentum $\vec{L} = \vec{l}_i + \vec{l}_{i-1} + ...$ and the z component L_z are constant and commute with the Hamiltonian H_{re}. Additionally, the total spin $\vec{S} = \vec{s}_i + \vec{s}_{i-1} + ...$, and the z component S_z also commute with H_{re}. These two quantities, L and S, couple together to form the total angular momentum, $\vec{J} = \vec{L} + \vec{S}$, and this *spin-orbit interaction* is represented by a perturbation of the form $H_{\mathrm{so}} = \beta(\vec{S} \cdot \vec{L})$ [64]. The eigenstates of the Hamiltonian may thus be written as a linear combination of eigenstates $|LM_z SM_z\rangle$ defined by the total and z components of the momentum and spin respectively. This is known as the *Russel-Saunders* or LS coupling scheme.

For each configuration, the possible states are labeled by L and S and are called *terms*. These terms are written with the notation ^{2S+1}L, where L takes the values S ($L = 0$), P ($L = 1$), D ($L = 2$) and so on. For each term, J may take any of the integer-separated values between $|L - S|$ and $|L + S|$, and each combination of term and J value, $^{2S+1}L_J$, is called a *level*. In the presence of an external magnetic field, each J level is split into $2J + 1$ *states* labeled with the quantum number M_J. This is known as the Zeeman effect, and the separation between m states is not resolvable in the experiments performed for this dissertation.

The spin-orbit coupling scales with atomic number, and for heavy elements may become comparable to the residual electrostatic interaction [64]. As a result, L

and S are no longer constant and thus the LS coupling scheme is a poor descriptor of the level structure. However, these systems may be described by $j - j$ coupling. In $j - j$ coupling, the individual orbital and spin momenta of each valence electron couple together independently, e.g. $\vec{j_1} = \vec{l_1} + \vec{s_1}$ and $\vec{j_2} = \vec{l_2} + \vec{s_2}$, which then couple together to form the total momenta $\vec{J} = \vec{j_1} + \vec{j_2}$. The level labels are written in the notation $(j_1, j_2)_J$ where J may take any of the integer-separated values that satisfy $|j_1 - j_2| < J < |j_1 + j_2|$.

As mentioned previously, the eigenstates in the LS or $j - j$ coupling schemes are often written as linear combinations of hydrogen-like orbitals, and the *purity* of the state is the contribution from the leading term in the expansion. For most low-Z elements the eigenstates are very pure, and the LS coupling scheme provides an accurate description of the electronic structure of the atom or ion [64]. The eigenstates and energy levels in either LS or $j - j$ coupling are most often calculated with atomic structure codes such as those of Cowan or GRASP2K and are discussed elsewhere (see Refs. [58] or [59] for more details).

Lastly, the coupling schemes (either LS or $j-j$) may be expanded by including nuclear effects in the Hamiltonian. For atoms or ions with non-zero nuclear spin, the nuclear spin I couples with the total momenta J to form $\vec{F} = \vec{I} + \vec{J}$, and an additional (but small) shift occurs between levels with different values of the quantum number M_F. Though this effect is included in this discussion for completeness, the scale of the hyperfine splitting is small and not resolvable in the measurements presented in this work. Further discussion on this topic is available in Ref. [64].

4.2 Electronic Transitions

Thus far, a discussion of the landscape of electronic structure has been provided. Electrons obey quantum mechanics and may only exist in discrete states around an atom. The number of electrons around an atom determines the possible states in which the electrons can exist. Electrons around atoms or ions may be excited to a higher energy state. This excitation may arise from interactions with light or other particles, e.g. free electrons. Given enough time, electrons in excited states will de-excite and produce a photon with wavelength

$$\lambda = \frac{hc}{E_u - E_l} \tag{4.7}$$

where h is Planck's constant, c is the speed of light, and E_u and E_l are the energies of the upper and lower level respectively. However, not all transitions are allowed to occur; that is, the probability for a particular de-excitation pathway depends on the properties of the upper and lower levels. For a given transition this probability is expressed as the Einstein A coefficient with units of s^{-1}. Using the notation above, A_{ul} is the rate at which an atom in the upper level will spontaneously emit a photon and decay to the lower level. Alternatively, the *lifetime* of the upper level may be defined as

$$\tau_u = \frac{1}{\sum_i A_{u \to i}} \tag{4.8}$$

where index i sums over all of the allowed transitions from level u. In the event that a level is defined by a single transition, the lifetime is simply the inverse of the A value for that transition. For the transition from state u to state l, the transition rate may

be calculated from Fermi's Golden Rule [106]:

$$W_{u \to l} = \frac{2\pi}{\hbar} |M_{ul}|^2 g(\hbar \omega) \tag{4.9}$$

where $|M_{12}|$ is the *matrix element* for the transition, and $g(\hbar\omega)$ is the density of final (lower) states. The matrix element is calculated from the eigenfunctions of the system and the Hamiltonian of a perturbation, H', that produces a photon release into the continuum [106]

$$M_{ul} = \langle u | H' | l \rangle = \int \psi_u^*(r) H'(r) \psi_l(r) d^3 r \tag{4.10}$$

where $\psi_u(r)$ and $\psi_l(r)$ are the upper and lower level wave functions. For electric dipole (E1) transitions the Hamiltonian takes the form $H' = -\vec{p} \cdot \vec{\epsilon}_0$. The quantity $\vec{p}$ is the electric dipole of the atom and $\vec{\epsilon}_0$ is the electric field amplitude. For optical transitions, only the electrons are affected by the transitions, and the dipole is written $\vec{p} = -e\vec{r}$. It follows that the matrix element may be rewritten

$$M = -\vec{\mu} \cdot \vec{\epsilon}_0 \tag{4.11}$$

where the quantity μ is the *electric dipole moment* of the transition. Assuming the field amplitude $\vec{\epsilon}$ is polarized in one direction (e.g. $\vec{x}$) and constant over the extent of the wavefunctions, the expression for the dipole moment becomes [106]:

$$\mu = -e \langle u | x | l \rangle = -e \int \psi_u^*(r) x \psi_l(r) d^3 r \tag{4.12}$$

The Einstein A coefficient is then directly related to this dipole moment via the following [64]:

$$A_{ul} = \frac{\omega^3}{3\pi \epsilon_0 \hbar c^3} |\mu_{lu}|^2 \tag{4.13}$$

93

Transition	Notation	Einstein A coefficient	Radiative lifetime	Parity change
Electric dipole	E1	10^7–10^9 s^{-1}	1–100 ns	yes
Magnetic dipole	M1	10^3–10^5 s^{-1}	0.01–1 ms	no
Electric quadrupole	E2	10^3–10^5 s^{-1}	0.01–1 ms	no
Magnetic quadrupole	M2	0.1–10 s^{-1}	0.1–10 s	yes
Electric octupole	E3	0.1–10 s^{-1}	0.1–10 s	yes
$\vdots$				

Figure 4.1 Reprint from [106]. Orders of magnitude for the A values, lifetimes, and features of different transition mechanisms.

where ω is the wavenumber of the released photon.

To summarize, the Einstein A coefficient of electric dipole transitions is determined by the matrix element, $|\mu_{lu}|$, which is calculated from the wavefunctions of the involved energy levels. Alternatively, the transition rate (for E1 transitions only) may be expressed as an *oscillator strength*, f, which is the dimensionless ratio between the transition rate and the rate at which a classical electron oscillating at the same frequency as the emitted radiation would oscillate. In some cases, the oscillator strength is reported as $\log(gf)$, where g is the Lande-g factor for the upper level [64]. The oscillator strength f is written in terms of the dipole moment as [106]:

$$f_{lu} = \frac{2m\omega_{ul}}{3\hbar} |\langle u| r |l \rangle|^2 = \frac{2m\omega_{ul}}{3\hbar e^2} |\mu_{lu}|^2 \tag{4.14}$$

For the plasmas utilized in this work, the observed transitions are all electric-dipole allowed transitions. As shown in Fig. 4.1, electric dipole (E1) transitions have transitions rates on the order of $10^7 - 10^9$ s^{-1}, and higher order transitions (E2, E3) or magnetic transitions (M1, M2) have much lower transition rates. For E1 transitions, the transitions must obey several *selection rules*. The rules for a single electron in a hydrogen-like system are as follows. First, the parities of the upper and lower levels must be different. In the electric dipole operator the single factor of r is odd, and if

94

the parity of the initial and final states are not different then the resulting integral in the electric dipole moment is exactly 0. As the wavefunctions for the upper and lower levels have parity given by $(-1)^L$, it follows that for the dipole moment to be non-zero that $\Delta L = \pm 1$. As photons do not affect with electron spin, the individual spin quantum numbers do not change and thus $\Delta S = 0$. Lastly, it follows from the rules for ΔL and ΔS that the total momenta must change, $\Delta J = 0, \pm 1$. Note that from angular momentum conservation and that photons carry a momentum of 1, no transitions may occur from a $J = 0$ to $J = 0$ term.

For heavy elements where the spin-orbit coupling is not negligible, the above selection rules are invalid as the numbers L and S are not well defined. In this case, the electric dipole transitions are bound by only two rules: 1) parity must change, and 2) $\Delta J = 0, \pm 1$. This allows the possibility for more than one electron to be involved in each transition as the levels are not beholden to the entirety of the LS selection rules just discussed. For the species in this work, Au I and Au II, the spin-orbit coupling is non-negligible, and the relevant E1 selection rules are limited to changes in parity and $\Delta J = 0, \pm 1$.

4.3   Summary of Known Au Spectroscopic Data

As discussed in Ch. 1, the atomic data available for high-Z elements is quite limited. Among the high-Z elements expected in neutron star merger ejecta, neutral and ionized gold are two of the simpler systems. The ground state of Au I consists of a closed $5d$ shell with a single valence $6s$ electron, and excited states of the system commonly take the form $5d^9(^2D)6snl$ where the outer electrons $(6snl)$ couple together before coupling to the core [107]. In the ion the configuration interaction is significant, and the coupling between the $5d^9$ and $5d^8$ cores and the valence shells leads to a large

number of levels; many of the terms are best described by $j - j$ coupling as the configurations are well-mixed with low purity [108]. In Au III, the assignment of LS terms is practically meaningless as purities may be as low as 11% [109].

The bulk of the known emission lines for Au I and II come from the surveys of hollow cathode spectra by [110] (PS), [107] (ED), and [108] (RW). Their studies comprise the bulk of the available data in the NIST Atomic Spectra Database. Platt & Sawyer primarily focused on Au I, and the work of Ehrhardt & Davis corroborated the level structures from the former. For both the ion and neutral many of the emission lines observed by one of the surveys is absent from the spectra of the other two. For example, lines from the Au I $6s6p(^4D_{5/2})$ level of Platt & Sawyer are absent from the spectra of Ehrhardt & Davis. However, ED's spectra contained few lines from levels with large orbital angular momentum, and excitation of levels with a $5d^9$ core was generally lacking. To date, terms of the $6s6p$ and $6s6d$ configurations of Au have yet to be corroborated by multiple sources.

The Au II literature contains similar problems, and both PS and ED report significantly fewer lines in Au II compared to Au I. However, Rosberg & Wyart, using a combination of hollow cathode spectra and Cowan's codes, report oscillator strengths for over 400 classified transitions. Of these transitions less than 30 are above 300 nm. To date, the structure of Au II remains incomplete and levels between 135,000 cm^{-1} and the ionization limit at 162,950 cm^{-1} have yet to be reported. These levels are likely in the triply excited configurations, e.g. $5d^76s^26p$, and have yet to be investigated aside from a single level in RW [108]. Many authors have utilized laser-induced fluorescence or similar techniques to measure lifetimes and transition probabilities for a small number of lines and levels of the Au systems [111, 112, 113, 114, 115, 116, 117]. Even so, the majority of the known levels below 135,000 cm^{-1} have little to no reported visible transitions associated with them.

All three surveys (PS, ED, RW) utilized hollow cathode sources wherein the high electron densities are often offset by a lower electron temperature. Though ED also studied arc and spark spectra, they limited these measurements to the range 300 - 400 nm. Comparing the three studies, it is apparent that population of the higher energy levels was generally poor as many of the corresponding transitions have very low intensities. It can be expected that a plasma source with a higher electron temperature may yield significant excitation of these levels, and new transitions from these levels may be observed. New UV-VIS measurements of Au I and II, when combined with the previous surveys, could provide relatively complete spectra for benchmarking future atomic structure calculations of these systems.

In the remainder of this Chapter, new measurements of the spectra of Au I and II are discussed. The data was analyzed using a series of custom Python codes developed at Clemson University. A sample of these codes are available in Appendix D and the GitHub repository by clicking here.

4.4 Spectroscopy at the Compact Toroidal Hybrid

The measurements of Au I and II spectra were carried out at the Compact Toroidal Hybrid (CTH) experiment at Auburn University [118]. CTH is a stellarator/-tokamak hybrid device developed to investigate the effects of 3D magnetic shaping on the stability of current-carrying plasmas. A thorough discussion of the machine and its' operation are available in Hartwell *et al.* [118]. In the following, a brief summary of the CTH is provided. While CTH is capable of operating without driving plasma currents, this work utilizes current-carrying discharges similar to previous experiments that investigated potential plasma diagnostic lines of W I [119]. A schematic of the CTH is shown in Fig. 4.2, and maximum field intensities are around 0.7 T.
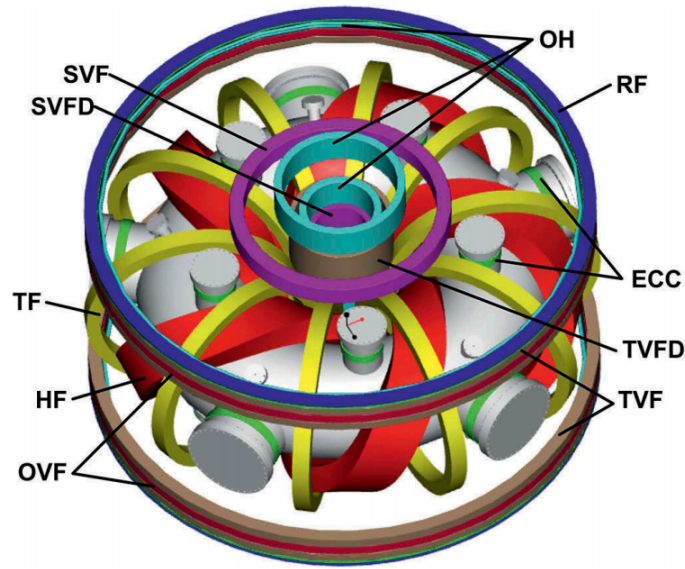
Figure 4.2 Reprint from [118]. A schematic of the Compact Toroidal Hybrid at Auburn University. The five-fold symmety and the field, error correction, and heating coils are shown.

Each CTH discharge proceeds as follows. At the start of the discharge, 10 electric generators provide 10 MW to power the field coils. A stable stellarator magnetic field configuration is generated, and hydrogen gas is puffed into the center of the vacuum chamber. Shortly after the gas is injected, the Electron Cyclotron Resonance Heating (ECRH) system(s) fire. Microwaves at 18 GHz are guided into the vacuum chamber by rectangular waveguides connected to klystron microwave sources. The microwaves ionize the hydrogen and heat the plasma such that the central electron density is on the order of 10^{18} m^{-3} and the central temperature is $T_e < 20$ eV. Once this base plasma is generated, the Ohmic Heating (OH) system discharges and produces a voltage in the OH coils. This voltage induces a plasma current up to 80 kA, and plasma conditions at the core of the device are $n_e < 5.0 \times 10^{19}$ m^{-3} and $T < 200$ eV. In total, each current-driven ('ohmic') discharge lasts between 40 - 80 ms.
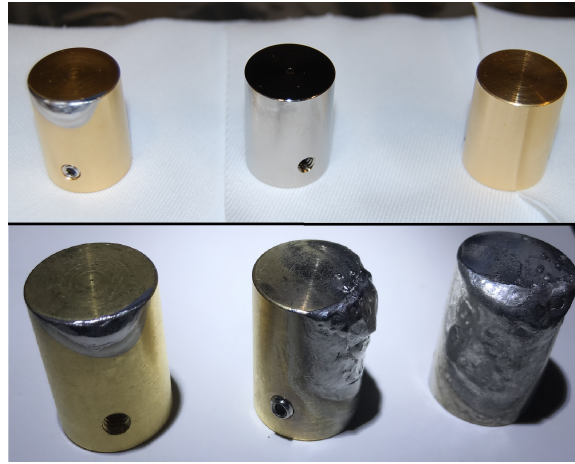
Figure 4.3 Photograph of the gold and nickel probes used to study gold spectra. (*Top*) From left to right: gold probe after weak OH discharges, the unfired nickel probe, and the second unfired gold probe. (*Bottom*) From left to right: The same gold probe as shown above, the second gold probe after many strong OH discharges, and the nickel probe after similar strong OH discharges.

In Johnson *et al.* (2019) [119], the CTH was used to perform spectroscopic investigations of potential plasma diagnostic lines of W I relevant to fusion research. In their work, spectra from a tungsten probe, inserted into the CTH vessel at various depths, were collected and compared to the W I literature. In this work, a similar experiment was carried out to study the emission spectra of gold. Two non-magnetic stainless steel (SS-316) cylinders, measuring 0.75" wide by 1.0" tall were electroplated with a thin nickel strike and 4 μm of pure gold. The nickel strike was necessary for the gold to stick to the probe surface. As the nickel may also be eroded into the plasma and produce emission lines, a separate steel cylinder was coated in 25 μm of pure nickel for comparison. The gold and nickel probes are shown in Fig. 4.3 both before and after the experiments in this chapter. The total length of plasma exposure for the nickel and gold probes is of order $\sim$ seconds.

At the top of the CTH vacuum chamber a manipulator holds a stainless steel rod that connects to the probes by two #8-32 stainless steel screws which thread

through the probe walls and into a groove machined into the support rod. At the maximum retracted position, the bottom of the probe sits outside the last closed flux surface. At the underside of the vacuum chamber, a lens mounted in front of an optical fiber collects light from around the probe tip into a Princeton Instruments HRS 500 Scanning Spectrograph. Prior to data acquisition, the spectrometer was calibrated with the Princeton Instruments IntelliCal software and a Hg lamp. The manufacturer quotes a systematic uncertainty of 0.02 nm which is consistent with the observed wavelengths of most background lines. A sample of the background lines are shown in Table 4.1. The largest deviation (0.05 nm) is found for the 656.27 nm line of neutral H. The calibration in neighboring wavelength regions is similar to the 0.02 nm uncertainty in the rest of the spectra, so this 0.05 nm discrepancy is likely an anomaly. However, as an upper bound, an uncertainty of 0.05 nm is adopted for all reported transitions.

The manipulator and the use of both nickel and gold probes allows for identification of lines belonging exclusively to the charge states of gold. By collecting spectra with both nickel and gold with the same calibration, center wavelength, and approximate plasma conditions, overlays of the two spectra reveal gold lines by their absence from the nickel spectra. Additionally, by looking at the intensities of each emission line as a function of depth into the plasma, the likely source of each line (background gas, iron/nickel, gold) is revealed. As the gold probe is inserted farther into the plasma, both the density and temperature are higher, and thus more gold is eroded into the plasma and excited. In total, 127 discharges were carried out with the three probes, and a summary of the measurements spanning 187 - 800 nm is shown in Table. 4.2. For most depths, the wavelength range 187 - 800 nm was broken into 17 ranges and center wavelengths were chosen such that there is a 2 - 3 nm overlap at the edges of the wavelengths regions. The measurements with the first gold probe

Table 4.1. Comparison of some observed contaminant lines versus their wavelengths in the NIST database [43]. Experimental uncertainties are listed in parentheses in Column (3).

Source	λ_{NIST} (nm)	λ_{exp} (nm)	$\Delta\lambda$ (nm)
C III	229.69	229.68(02)	0.01
C III	279.45	279.46(01)	-0.01
Fe II	279.79	279.77(02)	0.02
Fe II	294.84	294.84(03)	0.0
O III	326.55	326.54(01)	0.01
Fe I	359.27	359.27(02)	0.0
H I	434.05	434.05(01)	0.0
N II	472.16	472.16(02)	0.0
H I	486.14	486.14(0)	0.0
C I	588.95	588.96(0)	-0.01
C I	601.65	601.63(01)	0.02
N I	648.17	648.17(01)	0.0
H I	656.27	656.22(0)	0.05
Fe I	685.52	685.50(01)	0.02
N I	746.83	746.85(01)	-0.02
C III	778.04	778.03(0)	0.01

	Number of Discharges			
Probe | Depth (cm):	0	3	6	9
Au(1)	17	17	12	12
Au(2)	0	0	17	0
Ni	12	12	17	11

Table 4.2 Summary of the gold experiments at the Compact Toroidal Hybrid

were carried out with peak plasma currents between 6 - 33 kA, and the measurements with the second gold probe (Au(2) in Table 4.2) and the nickel probe were carried out with peak plasma currents between 55 - 69 kA.

At the start of each discharge ($t = 0$), a trigger is sent to the spectrometer. For each discharge, the spectrometer covers approximately 40 nm, and the spectra are integrated and collected at a rate of 800 Hz (every ~ 1.25 ms). Around frame 60 ($t = 75$ ms), the ECRH system has produced noticable emission from the plasma. Around frame 80 ($t = 100$ ms), the plasma is current-driven and the line intensities increase dramatically compared to the current-free portion of the discharge. In Fig. 4.4, a heatmap of a sample spectra is shown. Each peak in the spectra is plotted as a circle at the line center as a function of frame number. The peak height is encoded by the color from 0 (dark blue) to 20,000 (yellow). The maximum intensity for each pixel is 65,535 and the maximum of the color scale in Fig. 4.4 is set to only 20,000 to enhance the visibility of the peaks. In general, only a handful of transitions are apparent during the current-free portion of the discharge. In the current-driven portions, many lines appear and in some cases saturate one or more pixels.

4.5   X-Ray Filtering

As the magnetic fields in the device are relatively high ($B \leq 0.7$ T), the electrons in the plasma produce significant synchrotron radiation. To combat this, the
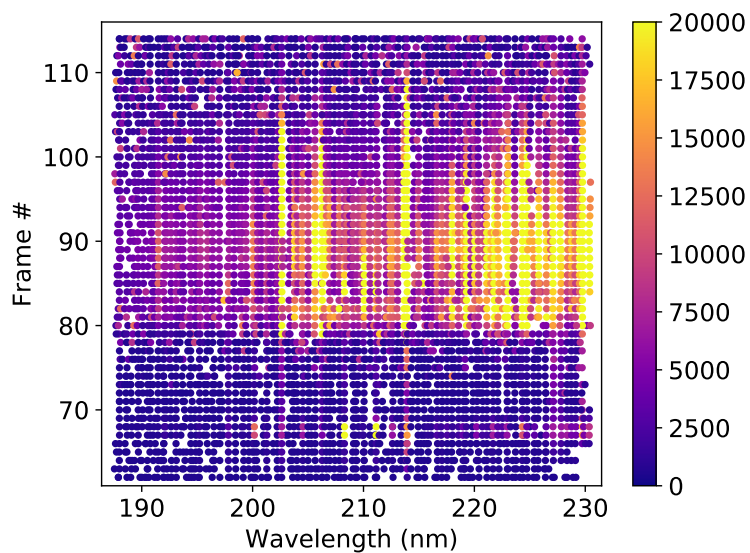
Figure 4.4 A plot of peak intensities as a function of wavelength and frame number for a sample Au(2) discharge. Each peak is plotted as a circle at the appropriate position. The intensities (0 - 65,535) are mapped on a 0 - 20,000 scale to increase contrast and visibility.
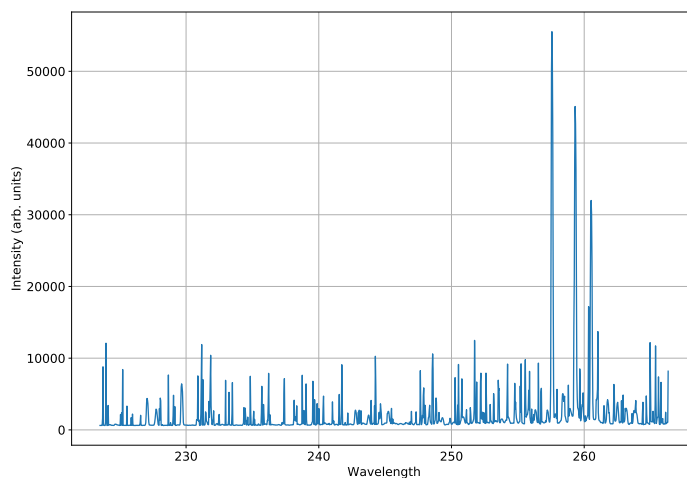
Figure 4.5 Counts versus wavelength for an ohmic heated discharge with the second gold probe Au(2).

spectrometer is surrounded by a thick layer of lead bricks. When a synchrotron x-ray makes it through the lead shielding and strikes the CCD, it produces erroneous transient peaks that are narrow and change from frame-to-frame. These x-rays can severely skew the profile of a real peak. Figure 4.5 shows a sample of x-ray contaminated spectra from the current-driven portion of the discharge. If a peak-finding code were used on this data, many of the x-rays would register as peaks. A custom x-ray filter was written in Python to remove the counts from the x-ray contaminated pixels. Within the spectra, the contaminated pixels may be identified by either or both of the following behaviors:

1. The frame-to-frame count values for a single pixel are inconsistent with a peak gradually changing intensity through the discharge,

2. Compared to the neighboring pixels, count values are unusually high.

Comparing the nearest neighbors in wavelength for a real peak, the ratio of a pixel's value to it's neighbor(s) rarely exceeds 2.0. For x-rays, this ratio well exceeds this value. A similar comparison may be made in time, and the frame-to-frame change in value for a single pixel rarely exceeds a similar value (2.0).

A 2-D representation of x-ray contaminated data is shown in Fig. 4.6. Typical background count values are around 600 - 1000, and three x-rays (shown in red) are present. Using the sample values in Fig. 4.6, the x-ray removal process proceeds as follows. Let us take for example the pixel with value '2540' and identify it by the index i in the wavelength direction and by the index j in the frame (time) direction. By comparing to the values at $(i, j-1)$ and $(i, j+1)$, we find ratios exceeding two. Comparing the neighbors in the wavelength direction $(i-1, j)$ and $(i+1, j)$ we find a similar ratio exceeding 2 for the comparison with pixel $(i-1, j)$. Either of these conditions flags the pixel as x-ray contaminated. In the event that the pixels on either

Figure 4.6 A 2-D representation of x-ray contamined spectra. The count values within each wavelength and time bin are shown as numbers. X-ray counts are shown in red.

side are not x-rays, the x-ray is removed by replacing the value at pixel (i, j) by the average of the two neighboring pixels. In this case, pixel $(i + 1, j)$ has a value of 3240 and would also be flagged as an x-ray. Therefore the appropriate value would instead be the average of the two neighboring non-x-ray values 984 and 921. If one is looping in order of increasing i and j, pixel (i, j) (initial value 2540) would be replaced with the average of the neighboring non-x-ray values $(984 + 921)/2 = 952.5$. When i iterates to $(i + 1, j)$ (value 3240), the resulting pixel $(i + 1, j)$ would be corrected to the value $(952.5 + 921)/2 = 936.8$.

In some cases, a single pixel may be contaminated in consecutive frames (times j and $j + 1$). In this case, the nearest wavelength neighbors are used to correct the pixel value. In cases where x-rays are present for more than 2 consecutive frames or wavelength bins, one iteration of the averaging procedure may not be sufficient for sufficiently correcting the height of the affected pixel. Therefore, the thresholding and averaging procedure is carried out several times to ensure that any large x-rays are

105
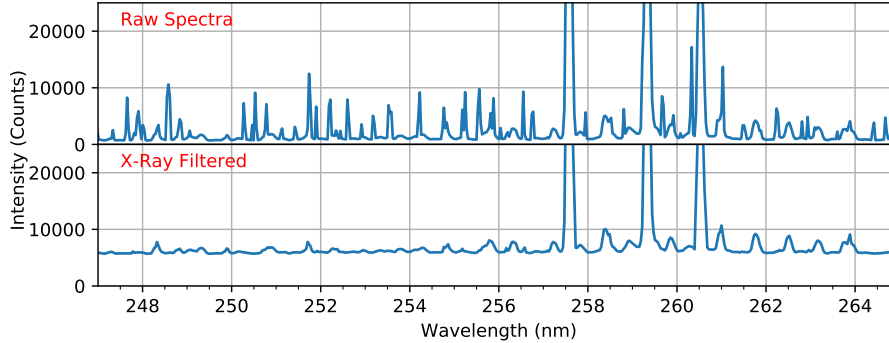
Figure 4.7 Sample spectra from a 1.25 ms exposure of using the Au(2) probe inserted 6cm past the last closed flux surface during an ohmic discharge. (*Top*) Zoom-in of raw data between 248 - 264 nm. (*Bottom*) Zoom-in of the same raw data cleaned of x-rays using the x-ray removal procedure.

sufficiently reduced to the interpolated background values. A sample spectra showing both the raw data and the x-ray filtered data is shown in Fig. 4.7. As shown, this procedure successfully removes x-rays on top of peaks while maintaining the integrity of each line profile. This x-ray removal procedure was used to clean all spectra, and a version of the x-ray filtering code is available in Appendix D.

4.6 Peak Finding and Identification

For each probe and depth in the experimental program, the list of peaks within each discharge was generated using the PeakUtils [120] and SciPy [121] packages. First, the PeakUtils **baseline** function estimates the 'background' contribution at each pixel via a polynomial fit. Within the function, pixels with values far from the average (e.g. peaks) are given a low weighting. Second, the PeakUtils function **indexes** estimates the approximate peak positions by searching for local maxima above a user-defined threshold value. For this analysis, the minimum distance between peaks was set to 2 pixels and the minimum peak height was set at 200 counts above the baseline

at each pixel. Finally, the central wavelengths of each peak are refined by the PeakU-tils **interp_peaks** function, which interpolates the central wavelength via a Gaussian fit at the estimated peak positions from the **indexes** function. Using this procedure, a master line list is generated for each probe and depth by summing the peak lists for each frame and binning the resulting list (**scipy.stats.binned_statistic**) with bin size 0.05 nm. In this way, all values within ± 0.025 nm of each peak position are included, and the experimental uncertainty is simply taken as the standard deviation of the peak values within each bin.

For each line in the second gold probe line list, it is desirable to look for each peak in the other gold probe spectra and the nickel spectra. For this purpose a code was written to generate 'Intensity Scatter Plots' for each observed peak. To summarize, this 'ISP' code carries out the following tasks

1. For each frame within a discharge, locate the peak positions.

2. For each peak, store the peak heights as a function of frame number.

3. Loop over all discharges (all probes and depths)

4. Plot the intensity of each peak as a function of depth and plating.

The output plots (and height vs frame data in .csv format) are saved for each entry of a user-defined peak list.

In the wavelength range 187 - 800 nm there are thousands of possible E1 transitions from both Fe I and Fe II. In many cases, transitions matching the level structure of gold overlap with Fe lines which are present in both the gold and nickel spectrums. The spectra also contains many lines from background gases and other plasma-facing materials (Cr, Ni) which can change quite dramatically with time. For example, Fig. 4.8 shows the ISP of the 486 nm Balmer line of neutral hydrogen

107
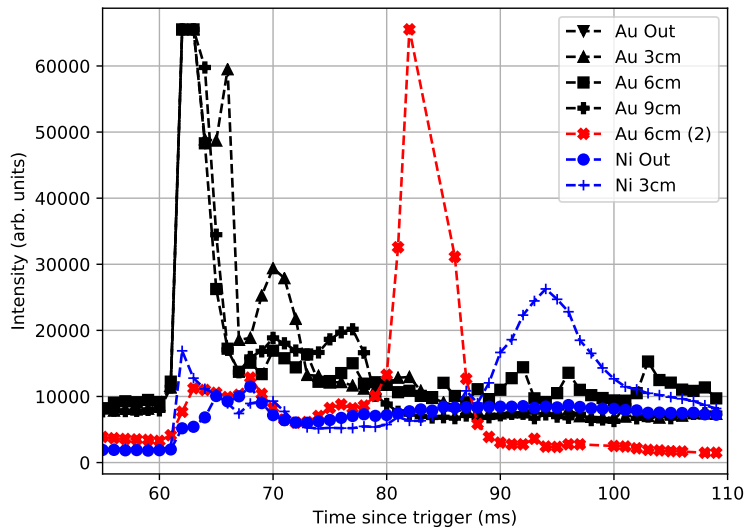
Figure 4.8 Time dependence of the 486 nm H I line (CTH shot numbers in descending legend order: 18112724, 18112745, 18112759, 18112765, 18113017, 18112910, 18112922). The spectral line height is plotted as a function of time for the first gold probe at insertion depths of 0 cm (upside-down triangles), 3 cm (triangles), 6 cm (squares), and 9 cm (+). Line heights from the second gold probe at 6 cm insertion (red ×) and the nickel probe at 0 cm (circles) and 3 cm (thin, blue +) are shown. Data is shown for both the current-free ($t < 70$ ms) and current-driven portions ($t > 70$ ms).

through a single discharge. As H is the working gas, the line is present in both the current-free ($t < 70$ ms) and current-driven ($t > 70$ ms) portions of the discharge. As shown, the peak is present for all probe platings and depths which is indicative that the transition may not be assigned to gold.

Figure 4.9 shows an ISP for a strong transition of Au I. As shown, the intensity increases with increasing depth and the peak is unobserved in the nickel spectra. Depending on the upper level, we find that lines belonging to the most highly excited levels are generally only present during the current-driven portion of the discharge. Though many suspected Au lines follow a similar trend as in Fig. 4.9, a good number are contaminated by possible overlapping transitions in Fe, Cr, or background gases.
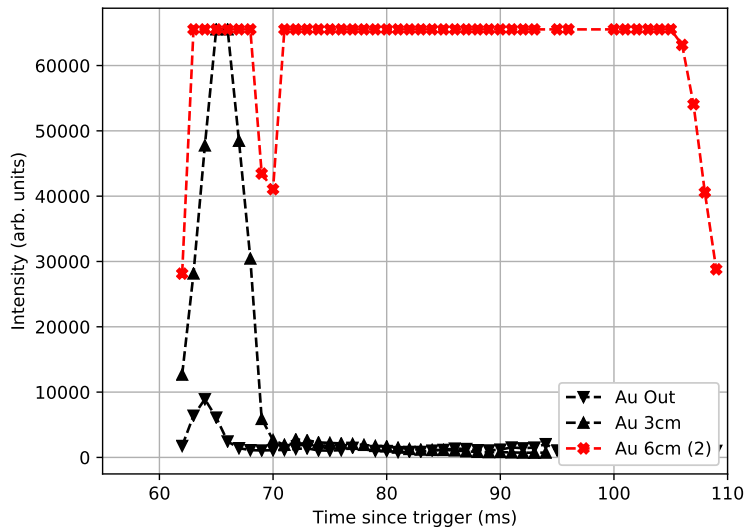
Figure 4.9 Time dependence of the intense 267.54 nm Au I line. The spectral line height is plotted as a function of time for the first gold probe tip at an insertion depth of 0 cm (upside-down triangles, shot 18112718) and 3 cm (triangles, shot 18112739), and a second gold probe tip at an insertion depth of 6 cm (red ×, shot 18113008). The emission at 267.54 nm is below the noise floor when the nickel probe tip was inserted.

By comparing nickel and gold spectra at similar plasma conditions, a list of gold candidate lines may be generated. As the Au(2) spectra were taken at a higher temperature than the first gold probe, it is possible that each peak could also be caused by the change in plasma conditions. To rule out possible non-gold transitions, the following tools were utilized. Efforts were taken to model the spectra with the collisional-radiative code ColRady [122] developed at Auburn University. The code is capable of utilizing the **adf04** data files found in the OPEN-ADAS (Atomic Data and Analysis Structure) database [123]. Given a set of energy levels, A values for the transitions, and electron impact excitation rates of the levels as a function of density and temperature, ColRadPy calculates the resulting spectrum and level populations as a function of density and temperature. However, for many of the elements relevant
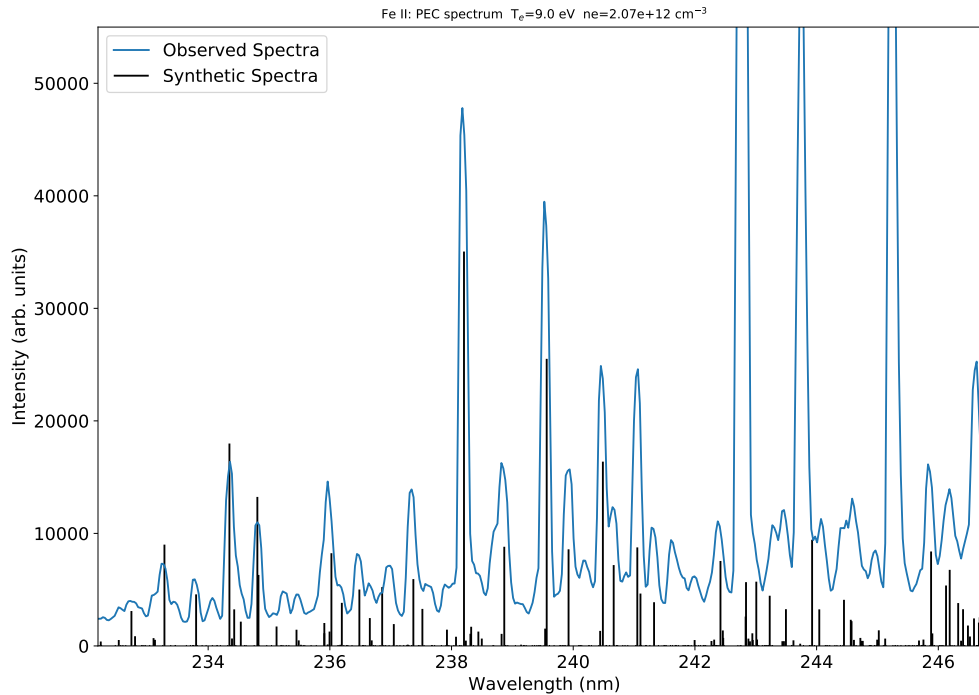
Figure 4.10 Synthetic Fe II spectra calculated with ColRadPy compared to gold spectra from the Au(2) probe.

to the CTH plasma, the available datafiles in the ADAS database contain incorrect level energies or have levels missing altogether.

The most success was had for the most-recent Fe II data (file 'chv6_ic#fe1.dat'), which allows for estimating the plasma conditions at the probe tip. While the datafile contains many levels, some of which are slightly different than NIST values, the level energies are of high enough quality to match some of the observed spectra. Using ColRadPy, Fe II synthetic spectra were generated across a dense grid of temperatures and densities and compared to the observed spectra. Within each single wavelength range, the spectra were normalized to the gold spectra by scaling the entire Fe II spectrum to closely match the peak heights in the gold spectra. Figure 4.10 shows

the best agreement between the Fe II synthetic spectrum and the observed spectra from Au(2) measurements within a single wavelength range. At this time in the current-driven portion of the discharge, the plasma conditions at the probe location, as given by ColRadP $n_e = 2 \times 10^{12}$ cm^{-3} and $T_e = 9$ eV, are close to the values calculated in the previous W I measurements at the CTH by Ref. [119]. It is noted that pointing the fiber to the sides of the probe significantly reduces the counts of known Au I lines, indicating that most of the emission from the eroded materials is close to the probe surface. With the plasma conditions at the surface approximately known, the spectra of common contaminants (C, N, O, Fe, etc.) may be generated with the NIST Local Thermodynamic Equilibrium (LTE) spectra tool and compared to the gold spectra. LTE spectra of H I, C I-III, N I-III, O I-III, Fe I-II, Cr I-II, and Ni I-II were compared to the gold spectra. These spectral comparisons were used to rule out gold-candidate lines.

Lastly, we may study each peak across all discharges. As each discharge develops in time in a similar but not identical matter, it is necessary to choose the right time at which to compare nickel and gold spectra. Figure 4.11 shows the plasma conditions (electron density, plasma current) for two similar but different discharges. Electron densities are line-of-sight averages from microwave interferometry at 244 GHz [118]. Using these data, the the most-similar frames in the gold and nickel data may be compared, and the list of gold candidates may be further narrowed. Significantly higher counts in the Au(2) probe data at 6cm compared to Ni probe data at 6cm indicates a strong likelihood of a gold transition. This method is independent of the available ADAS datafiles or data availability in the NIST database. However, judgment of an addition or removal from the gold candidate list must be made with each consistency check (plasma conditions, spectra comparisons, ISPs, and LTE comparisons) in mind.
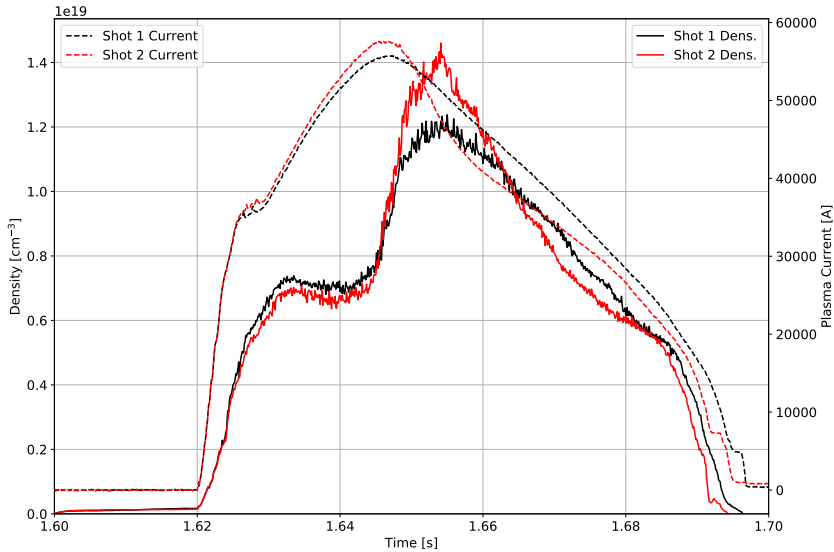
Figure 4.11 Line-of-sight averaged electron densities (solid line) and plasma currents (dashed lines) for two samples discharges. Plasma current values are displayed on the right y-axis. The spectrometer trigger is set to 1.6 s.

With these methods, the list of possible gold peaks was reduced. To assign energy levels to each transition, the following method was adopted. A list of all possible allowed E1 transitions ($\Delta J = 0, \pm 1$ and changes in parity) was generated from the known levels of Au and Au$^+$ in the literature. We note that in Au I and II pure LS coupling selection rules, i.e. the additional constraints $\Delta S = 0$, $\Delta L = 0, \pm 1$, are not obeyed as the core-valence coupling is not insignificant [107]. This is illustrated by transitions between levels with different core configurations such as $5d^{10}5f$ ($^2F^\circ_{5/2}$) $\rightarrow$ $5d^96s^2$ ($^2D_{3/2}$) of Au I at 217.08 nm [110].

The list of calculated Ritz wavelengths is converted from vacuum to air wavelengths with the IAU standard conversion from [124]. The list of air wavelengths is compared to the list of peaks in the spectra, and matches are restricted to within the typical uncertainty of the observed wavelengths, i.e. $|\lambda_{\text{obs.}} - \lambda_{\text{ritz}}| < 0.06$ nm. To

confirm the assignment of energy levels to each transition, the match list was used to perform a least-squares level energy optimization with the code 'LOPT' [125]. Only lines whose behavior strongly indicates a gold transition were used. As the spectra are lower resolution than the previous work in the literature, the optimization is used to aid the identification of new lines and to check for consistency against the available literature. In the level optimization, lines that have large discrepancies with the Ritz wavelengths, as calculated from the optimized level energies, were removed from consideration. Where necessary, level energies were fixed w.r.t. the ground state to improve the agreement between the optimized energies, Ritz wavelengths, and the available literature. The details regarding our final choice of fixed levels and their effects on the relevant quantities are discussed in Sections 4.7 and 4.8.

The calculation of the reported intensities needs to consider two aspects: (1) each discharge develops in time in a similar but not identical manner, and (2) the instrument response, as a function of wavelength, is not known. To (1), we chose to report line intensities from the same single time in 17 different discharges where the plasma conditions are most similar. In the choice of exposures, central densities are on average $n_e = 1.0 \pm 0.5 \times 10^{19}$ cm^{-3} and plasma currents are 59 ± 6 kA. At the location of the probe, the conditions are similar to those quoted previously ($n_e \sim 10^{12}$ cm^{-3}, $T_e \sim 10$ eV).

For (2), no external calibration source was available. Therefore, we have modified the relative intensity calibration procedure from [126], where argon branching fractions were employed to compare spectra on the same (relative) intensity scale. Consider two transitions from the same upper level with wavelengths λ_1 and λ_2. If

the A values are known, the branching fraction may be written

$$BR_{1,2} = \frac{A_1}{A_2} = \frac{I_1/\epsilon(\lambda_1)}{I_2/\epsilon(\lambda_2)} \tag{4.15}$$

where the intensities I_1 and I_2 are found by integrating over the spatial extent of the peak, and the photon detection efficiencies ϵ are functions of wavelength [126]. If several such transitions from the same upper level with known branching fractions are observed, the photon detection efficiencies $\epsilon(\lambda)$ can be calculated and used to place the overlapping spectra on the same relative intensity scale. In our spectra, the observed transitions of Fe I, Fe II, and background gases are insufficient for performing the procedure outlined by [126].

Using the integrated heights of peaks within the spectral overlap of neighboring discharges, the present intensity calibration is adapted from [126]. Consider two discharges, labeled i and $i+1$, with a several nm overlap in wavelength coverage. At a time where the plasma conditions (electron density, plasma current) are similar, the change in peak heights may be attributed to the change in instrument response between the two grating positions. The conversion factor for intensities in range $i+1$ to the scale of range i may be calculated by

$$S_{i,i+1} = \frac{1}{N} \sum_{j=1}^{N} \frac{I_j^{(i+1)}}{I_j^{(i)}} \tag{4.16}$$

where the sum is over the number of peaks N within the overlap region, and the intensities $I^{(i)}$ and $I^{(i+1)}$ are calculated by numerical integration of a Gaussian fit to each peak in the respective wavelength regions. The factors $S_{i,i+1}$, when expanded across all wavelengths, mimics the photon detection efficiency $\epsilon(\lambda)$ in Eq. 4.15. For the 16 overlap regions, between 1 - 11 peaks (4 on average) were used to place the entire 187 - 800 nm wavelength range on the same intensity scale using Eq. 4.16. This
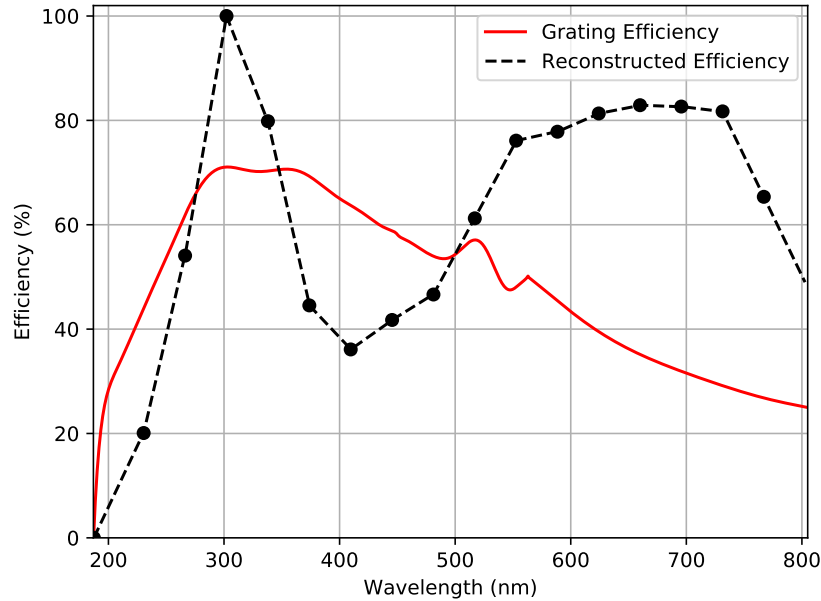
Figure 4.12 Manufacturer-stated photon detection efficiency of the grating (solid red) and the reconstructed photon detection efficiency (dashed black). The profiles are not directly comparable (see text). Locations of the overlap regions used to reconstruct the photon detection efficiency are shown as black circles.

procedure provides intensity scaling factors at the overlap wavelengths. The values between these small overlap regions are calculated by linear interpolation, and the edge cases are considered as follows. In the first wavelength range, the conversion factor is interpolated from 0% efficiency at the UV-cutoff in air ($\sim$187 nm) to the efficiency at the first overlap region (227 nm). The last overlap region at 767 nm contains no peaks, and the values in the final wavelength window are extrapolated from the previous region. The final intensity correction factors S are plotted alongside the manufacturer-stated photon detection efficiency of the grating in Fig. 4.12. Though plotted on the same scale, the reconstructed and grating efficiencies cannot be directly compared. The reconstructed efficiency is a convolution of the transmission efficiencies of all optical elements, including the grating.

The sharp rise in detection efficiency around the blaze wavelength (300 nm) is consistent with the expected grating behavior. The up-tick in the reconstructed efficiency above 400 is unexpected but consistent with the discharges used for the comparisons above 400 nm. These plasmas experienced disruptions during ohmic heating, and the calculation of the efficiency factor S for their overlap regions may be skewed by low counts in the comparable portions of the discharges.

The intensity calibration may be checked with known branching ratios, the intensity response S substituted for $\epsilon(\lambda)$, and integrated intensities with Eq. 4.16. Only 1 pair of the observed Au I transitions share the same upper level and have previously reported A values: the 242.79 nm and 312.28 nm transitions from $5d^{10}6p$ ($^2\mathrm{P}^\circ_{3/2}$). Both transitions are possibly blended with transitions from Au II and a nearby transition of Fe II. At the time specified above, calculation of the ratio $I(243)/I(312) = 5$ is unaffected by the intensity calibration. Despite the ratio being an underestimate due to saturation of the peak at 242.79 nm, the ratio is within a factor of ~ 2 of the known value (10.4) [43].

As an additional check on this procedure, we identified Fe I and Fe II lines in our spectra for which A values are available in the NIST database [43]. Three pairs of lines in Fe II and 9 pairs of lines in Fe I were found which share the same upper levels and are present in the same current-driven portion of the discharge as used to report gold intensities. Without the efficiency correction applied, the intensity ratios are within a factor of 7 of the known A value ratios. With the correction applied, the ratios are within a factor of 3 of the known A value ratio. As the gold lines reported in this work were observed close to the order they are listed, it is also possible that degradation of the gold plating reduced the observed Au counts as the wavelength range increased. Considering these complications, the reported gold intensities are sufficient for a qualitative discussion of the lines but should not be used to calculate

A value ratios of high quality.

Lastly, the intensities of Au I and Au II lines were normalized on the same 0 - 100 relative scale such that the strongest lines post-correction are set to 100. When gold wavelengths may be affected by neighboring transitions from other species, the element and charge state of the species contributing to the blended line is indicated, e.g. Bl. (Fe I). Labels 'Broad' and 'Obscured' indicate when an observed line is noticeably wider than other similar transitions or when a line is partially obscured by the strength of a nearby transition. Additionally, horizontal lines separate the wavelength ranges observed by the spectrometer in Tables 4.8 and 4.8. Though all three probes were used in the line identification process, all gold wavelengths and intensities reported in the following sections are taken from the spectra of the second gold probe at a position 6 cm inside the edge of the plasma (CTH shot numbers 18113008 - 18113025).

4.7   Au I Results

In total, 86 Au I lines are attributed to 90 possible transitions (Table 4.8) involving 62 levels (Table 4.8). The total uncertainties in the line positions are given in parentheses, and levels of odd parity are denoted by the '°' symbol. Where available, a reference to previous detections of each line with the conventions [110] (PS), [107] (ED), [127] (BG), and [108] (RW) are provided. In both PS and ED, L and S information of the $6s6d$ levels is unavailable, and the authors adopted independent numeric labeling schemes. Where applicable, labels from both PS and ED are listed, with the lower of the two numbers corresponding to the label from Platt & Sawyer [110]. Forty-five Au I lines were unobserved by the references compiled here and are labeled (New). For both Au I and Au II, lines longer than 550 nm are considered tentative

as nickel measurements at a 6 cm probe tip depth were not collected in this range.

As a check on the identifications in Table 4.8, level energies are re-calculated using the level assignments available in the literature and the measured wavelengths. We used the level optimization code 'LOPT' [125], which optimizes the level energies given a set of observed wavelengths. The uncertainty in the level energies is derived from the experimental uncertainties in the associated transitions. The re-calculated level energies are collected in Table 4.8 and compared to the available literature. All calculated energies are reported with respect to the ground state of the system, $5d^{10}6s$ ($^2S_{1/2}$), which is fixed at both 0 energy and 0 uncertainty. Using the ground state as the only constraint, the uncertainties in the level energies are on average ± 6.4 cm^{-1} from LOPT and the average difference between the experimental and literature energies is 4.2 cm^{-1}. By fixing the level $6s6d$ $34_{3/2}$ ($86,507.68 \pm 0.005$ cm^{-1}), the average uncertainty and energy difference are reduced to 5.2 cm^{-1} and 1.5 cm^{-1} respectively. Using both the literature and the calculated level energies the average difference between the observed and Ritz wavelengths is 0.02 nm.

In Au I, the observed transitions involve the following single-electron valence configurations: ns ($n = 6, 7, 9, 11, 14$), np ($n = 6, 7$), and 1 - 2 J levels from each of the nd ($n = 6$ - 9, 11 - 14) configurations. No transitions involving the ns ($n = 8, 10, 12, 13$) levels from PS and ED were observed. For transitions involving the nd ($n = 6-9$) configurations, the splitting between the $J = \frac{3}{2}$ and $J = \frac{5}{2}$ is large enough that transitions from individual nd (^2D_J) levels are resolvable. For $n = 11 - 14$, the splitting between the two levels is smaller than the resolution of the spectrometer; however, the line profiles do not indicate contributions from decays of both the $J = \frac{3}{2}$ and $J = \frac{5}{2}$ levels.

For the $5d^9$ core, transitions were observed to originate from one of the $6s7s$ levels, 16 $6s6d$ levels, and 18 $6s6p$ levels of PS [110] and ED [107]. It is interesting

that the transitions involve many of the $6s6p$ levels that were *not* seen by Ehrhardt & Davis [107]: $^4D^{\circ}_{5/2}$, $^4F^{\circ}_{3/2}$, $^4D^{\circ}_{1/2}$, $^4D^{\circ}_{3/2}$, $^2F^{\circ}_{5/2}$, and $^2P^{\circ}_{3/2}$. For the $6s6d$ configuration, 16 of the 18 known levels each involve 1 - 4 transitions. No lines involving the levels $6s6d$ 7 $(28)_{11/2}$ or $6s6d$ 9 $(32)_{9/2}$ were observed.

The original studies of these systems used hollow cathodes or spark discharges, and intensities of lines originating from the $6s6d$ levels in the literature were typically small. In the present work, the intensities of lines from these levels are often comparable to one-electron transitions between low-lying levels during the current-driven portion of the discharge. From the 33 transitions involving the $6s6d$ configuration, 15 were unobserved by both PS and ED. Ten of these newly observed transitions, originating from the $J = \frac{3}{2}, \frac{5}{2}$ levels of the $6s6d$ configuration, decay to the $6s6p$ configuration. The remaining 5 (new) transitions from $6s6d$ decay to the $6p^2$ and $7p$ configurations and follow a similar trend in their intensities.

In total, the newly identified lines are spread across a wide array of upper levels. Four originate from levels of the $6s7s$ configuration, 4 occur between low-lying $6s6p$ and $6s^2$ levels, 15 involve the (primarily) $J = \frac{3}{2}, \frac{5}{2}$ levels of $6s6d$ (see above), and 22 transitions are decays from various ns and nd levels. Of these last 22 lines, 2 are one-electron transitions to the $6p$ ($^2P_{1/2}$) level, and the remaining 20 decay to various levels in the $6p$ configuration. These transitions, $5d^9(...) \rightarrow 5d^{10}(...)$, expected to be weak by Ehrhardt & Davis [107] and mostly absent from their data, were not uncommon in the tables of Platt & Sawyer [110]. However, this difference may be explained, as even though PS and ED utilized hollow cathodes, comparison of their line lists suggests vastly different plasma conditions in the two experiments.

4.8 Au II Results

In Au II, 76 unique lines arising from 81 possible transitions are reported, 51 of which are unreported in the literature, involving a total of 69 levels. The lines and levels are collected in Tables 4.8 and 4.8 and follow the same conventions as previously discussed for Au. The level energies are taken from the work of RW [108]. For some of the Au$^+$ levels, L and S information is unavailable due to the low purity of the levels, and the numerical labels are adopted from RW [108]. Where possible, the level labels have been updated according to the designations in the NIST database [43].

Au$^+$ contains considerably more levels than Au, and nearly 40% of the known levels are missing representation in the present work. Additionally, as shown in Table 4.8, many of the levels are defined by only a single transition. The transitions linking the excited states to ground are in the UV shortward of 187 nm, so the level optimization proceeds as follows. We define the ground state ($E = 0 \pm 0$ cm^{-1}) and connect the observed transitions to ground using the minimum number of levels: $6s$ ($^3D_3$) (15,039.572 cm^{-1}), $6s^2$ ($^1D_4$) (65,307.005 cm^{-1}), $6s6p$ ($^3D_1$) (93,830.264 cm^{-1}), and $7p$ (5/2, 1/2)$_2$ (119,446.496 cm^{-1}) with the uncertainty quoted by Rosberg & Wyart (0.005 cm^{-1}). Using only these four levels as constraints, the re-calculated level energies have an average uncertainty of 20.3 cm^{-1} and the average difference between the calculated and literature energies is 7.3 cm^{-1}. As many of the levels are poorly constrained, some of the differences between the optimized and literature energies are larger than the corresponding uncertainties. Additional constraints were provided by fixing 9 additional levels (denoted by an uncertainty of 0.005 cm^{-1} in Table 4.8) with respect to the ground state.

Using these constraints the recalculated (average) level energy uncertainty of the free levels is reduced from 20.3 cm^{-1} to 6.1 cm^{-1}. The average difference

between the observed wavelengths and the Ritz wavelengths, calculated from the literature values of the level energies, is 0.03 nm. Using the optimized energies from the procedure above and excluding lines from levels defined by a single transition, a similar average of 0.02 nm is found. While the uncertainties of the level energies for the Au^+ optimization are larger than that of Au, the agreement between the literature values and the optimized energies is good. On average, the difference between these energies is 2.8 cm^{-1}, which corresponds to a wavelength uncertainty of ± 0.04 nm at 400 nm.

In many cases expected transitions of Au III are co-incident in wavelength with peaks in the spectra. Two peaks are possibly the known Au III transitions at 208.28 nm (Au II blend) and 322.8 nm from Ref. [128]. RW explicitly stated that no Au III emission was present in their Fourier transform spectra, and only very weak lines in the UV were observed in their grating spectra. RW asserts that this may be explained by charge state loss via charge exchange with the helium gas in their hollow cathode. Alternatively, it is possible that collisional de-excitation limited their detections to the strongest transitions in the UV for many of their levels. Given the possible Au III in our spectra, the high temperature ($\sim$ 10 eV), and the low pressure compared to hollow cathodes operating at several mTorr, the intensities and level assignments of the observed lines may be attributed to significantly different level populations compared to RW [108]. In this work, it is expected that the levels did not suffer from collisional de-excitation and thus visible transitions from the same levels were observable.

Almost half of the observed transitions of Au II are at wavelengths longer than 300 nm, and 38 of the previously unobserved transitions are in this region. This is in stark contrast to previous works which focused shortward of 300 nm. These 38 transitions stem from the $6d$, $6p$, $7p$, $7s$, and $8s$ levels at primarily high energies

121

$(E > 100,000 \text{ cm}^{-1})$.

The 51 newly observed transitions are spread over a large number of upper levels. Five originate from the $J = 2$ and $J = 3$ fine structure levels in the $7s$ and $8s$ configurations. Seven transitions connect the $6p$ and $7p$ configurations to the $6s^2$ and $6d$ configurations. Thirty transitions connect the $6d$ levels to 4 of the $6p$ and 26 of the $6s6p$ fine structure levels. We note that these two-electron transitions, $6d \rightarrow 6s6p$, are forbidden under normal LS coupling but may be allowed in Au II as the configuration interaction is non-neglible (see the calculations of RW [108]). Just as in Au I, the two-electron transitions are often similar in intensity to one-electron transitions during current-driven plasmas. Lastly, 9 transitions connect the $6s6p$ levels to low-lying levels in the $6s^2$ configuration. These transitions, $5d^8 6s6p \rightarrow 5d^8 6s^2$, are extremely common in RW's grating spectra where over 70% of their transitions involve a $6s6p$ level.

It is not unexpected that the majority of the newly observed lines are between terms with different core configurations. Transitions of this type, e.g. $5d^7(...) \rightarrow 5d^8(...)$ or $5d^8(...) \rightarrow 5d^9(...)$, constitute $\sim$50% of the lines in RW's grating spectra. The lines of this nature are generally absent from the current-free portion of the discharge and typically strong during current-driven portions. Presence during only the hottest portions of the discharge is consistent with the energies of the upper levels and lends confidence to the assignments of the levels in these transitions.

We undertook a systematic study of the Au I and Au II systems by studying spectra from eroding a gold-plated target inside the Compact Toroidal Hybrid experiment at Auburn University. The unique set of plasma conditions in CTH allows for significant excitation of the levels of interest. The use of both gold-plated and nickel-plated probe tips makes it possible to isolate emission lines unique to the surface plating of the probe tips. The procedure developed is applicable to a wide variety of

elements. For elements that are not plate-able, targets of pure metal may be used as was the case in [119]. Collisional-radiative modeling of Fe II emission suggests that plasma conditions at the probe tips ($T_e \sim 10$ eV, $n_e \sim 10^{12}$ cm^{-3}) are comparable to those found in previous experiments at the CTH [119]. The spectra suggest the presence of some Au III emission.

Eighty-six unique emission lines attributed to Au I are observed, 45 of which were previously unobserved. In Au, 18 $6s6p$ levels are identified and all but two of the $6s6d$ levels proposed by PS [110] and ED [107] are observed. In Au II, 76 unique lines were found, 51 of which were previously unobserved. Over half of the newly observed lines from Au II are in the visible longward of 300 nm. The line classifications in both systems are corroborated by a least-squares level optimization, and the resulting level energies and their uncertainties are consistent with the resolution of the spectrometer.

Using the peaks within the overlaps of neighboring wavelength windows, observed intensities are placed on the same relative scale. For both Au I and II, two-electron transitions between levels with different core configurations are found and are similar in intensity to LS-allowed one-electron transitions. Compared to previous work, which primarily focused on UV transitions, the CTH experiments revealed new emission lines in both the UV and visible spectra. When combined with the previous line surveys of Platt & Sawyer, Ehrhardt & Davis, and Rosberg & Wyart, this work provides useful benchmarks for future atomic structure calculations of these systems.

Table 4.3. Observed transitions in Au I. Air wavelengths and uncertainties (in parentheses) are reported in nm. The intensities are normalized to a 0 - 100 scale. Level labels are taken from the most recent literature in the NIST database [43], and Ritz wavelengths are calculated from the experimental level energies in Table 4.8. Wavelength ranges are indicated by the additional horizontal bars.

Int.	λ_{exp}	λ_{Ritz}	$\Delta\lambda$	Lower Level	J_l	Upper Level	J_u	Note	Ref.
0	201.26(06)	201.22	0.04	$5d^96s^2$ ^{2}D	5/2	$5d^96s6p$ ^{2}P°	3/2		PS
0	212.68(05)	212.67	0.01	$5d^{10}6s$ ^{2}S	1/2	$5d^96s6p$ ^{4}P°	3/2		PS
1	217.09(05)	217.09	0.0	$5d^96s^2$ ^{2}D	3/2	$5d^{10}5f$ ^{2}F°	5/2	Broad	PS
0	229.11(06)	229.07	0.04	$5d^96s^2$ ^{2}D	5/2	$5d^96s6p$ ^{2}F°	7/2	Bl. (Fe II)	New
1	235.24(05)	235.27	-0.03	$5d^96s^2$ ^{2}D	5/2	$5d^96s6p$ ^{2}D°	5/2	Bl. (Fe II)	PS
0	236.17(05)	236.21	-0.04	$5d^96s^2$ ^{2}D	5/2	$5d^96s6p$ ^{4}F°	3/2		New
1	237.58(06)	237.63	-0.05	$5d^96s^2$ ^{2}D	5/2	$5d^96s6p$ ^{2}D°	3/2		PS
1	238.81(05)	238.78	0.03	$5d^96s^2$ ^{2}D	5/2	$5d^96s6p$ ^{4}D°	7/2		PS
18	242.76(05)	242.8	-0.04	$5d^{10}6s$ ^{2}S	1/2	$5d^{10}6p$ ^{2}P°	3/2	Bl. (Au II, Fe II)	PS
1	252.54(06)	252.49	0.05	$5d^{10}6p$ ^{2}P°	3/2	$5d^96s6d$ 15	5/2		New
18	253.49(05)	253.52	-0.03	$5d^{10}6p$ ^{2}P°	1/2	$5d^96s6d$ 31	3/2		New
1	256.85(05)	256.88	-0.03	$5d^{10}6p$ ^{2}P°	1/2	$5d^96s6d$ 5	3/2		New
19	258.93(05)	258.96	-0.03	$5d^96s6p$ ^{4}P°	5/2	$5d^96s6d$ 15	5/2		PS
21	263.76(05)	263.74	0.02	$5d^{10}6p$ ^{2}P°	3/2	$5d^96s7s$ 33	5/2	Bl. (Fe II)	New
30	266.61(05)	266.64	-0.03	$5d^{10}6p$ ^{2}P°	3/2	$5d^96s6d$ 12	5/2	Bl. (Fe I)	New
42	267.23(05)	267.24	-0.01	$5d^96s^2$ ^{2}D	3/2	$5d^96s6p$ ^{2}P°	3/2		New
57	267.54(05)	267.59	-0.05	$5d^{10}6s$ ^{2}S	1/2	$5d^{10}6p$ ^{2}P°	1/2		PS
74	280.06(06)	280.1	-0.04	$5d^{10}6p$ ^{2}P°	1/2	$5d^{10}12d$ ^{2}D	3/2	Bl. (Fe II, N III)	PS
57	301.76(05)	301.75	0.01	$5d^96s6p$ ^{4}F°	7/2	$5d^96s6d$ 12	5/2		PS
76	302.91(05)	302.91	0.0	$5d^96s^2$ ^{2}D	5/2	$5d^96s6p$ ^{4}P°	5/2		PS
58	304.46(05)	304.46	0.0	$5d^96s6p$ ^{4}F°	5/2	$5d^96s6d$ 14	3/2		New
76	306.22(05)	306.23	-0.01	$5d^96s6p$ ^{4}F°	5/2	$5d^96s6d$ 13	3/2	Broad	New
59	308.19(05)	308.18	0.01	$5d^96s6p$ ^{4}D°	5/2	$5d^96s6d$ 13	3/2		New
84	312.29(05)	312.29	0.0	$5d^96s^2$ ^{2}D	5/2	$5d^{10}6p$ ^{2}P°	3/2		PS

124

Table 4.3 (cont'd)

Int.	λ_{exp}	λ_{Ritz}	$\Delta\lambda$	Lower Level	J_l	Upper Level	J_u	Note	Ref.
59	312.5(05)	312.53	-0.03	$5d^{10}6p$ ^{2}P°	3/2	$5d^{10}14s$ ^{2}S	1/2	Bl. (N III)	PS
84	313.66(05)	313.61	0.05	$5d^{10}6p$ ^{2}P°	3/2	$5d^{10}12d$ ^{2}D	3/2	Bl. (Fe I, Fe II)	PS
59	314.8(05)	314.78	0.02	$5d^96s^2$ ^{2}D	3/2	$5d^96s6p$ ^{4}P°	1/2	Bl. (Fe I)	New
85	323.08(05)	323.08	0.0	$5d^96s6p$ ^{4}F°	7/2	$5d^96s6d$ 25	9/2	Bl. (Fe I)	ED
59	323.7(05)	323.67	0.03	$5d^96s6p$ ^{4}P°	5/2	$5d^{10}12d$ ^{2}D	3/2	Bl. (Fe II)	New
88	324.75(06)	324.75	0.0	$5d^96s6p$ ^{4}F°	5/2	$5d^96s6d$ 11	5/2		New
59	325.33(06)	325.31	0.02	$5d^96s6p$ ^{4}F°	5/2	$5d^96s6d$ 10	3/2	Bl. (Fe I)	PS
88	326.46(05)	326.5	-0.04	$5d^96s6p$ ^{4}F°	5/2	$5d^96s6d$ 31	3/2		ED
88	331.18(07)	331.18	0.0	$5d^96s6p$ ^{4}D°	5/2	$5d^96s6d$ 6 (26)	5/2		New
88	331.18(07)	331.18	0.0	$5d^96s6p$ ^{4}D°	5/2	$5d^96s6d$ 27	3/2		New
59	332.05(05)	332.01	0.04	$5d^{10}6p$ ^{2}P°	1/2	$5d^{10}7d$ ^{2}D	3/2		New
61	338.21(07)	338.2	0.01	$5d^96s6p$ ^{4}P°	3/2	$5d^96s6d$ 6 (26)	5/2	Bl. (Fe I, O III)	PS
61	338.21(07)	338.2	0.01	$5d^96s6p$ ^{4}P°	3/2	$5d^96s6d$ 27	3/2	Bl. (Fe I, O III)	PS
90	342.2(05)	342.19	0.01	$5d^96s6p$ ^{4}P°	5/2	$5d^{10}9d$ ^{2}D	5/2		PS
61	353.59(05)	353.58	0.01	$5d^96s6p$ ^{2}F°	7/2	$5d^96s6d$ 16	5/2		PS
90	362.28(05)	362.29	-0.01	$5d^96s6p$ ^{4}F°	3/2	$5d^96s7s$ 33	5/2		New
61	368.09(05)	368.09	0.0	$5d^96s6p$ ^{4}F°	7/2	$5d^{10}11d$ ^{2}D	5/2	Broad	New
62	368.61(07)	368.63	-0.02	$5d^96s6p$ ^{4}D°	5/2	$5d^{10}14d$ ^{2}D	3/2	Broad	New
62	368.61(07)	368.58	0.03	$5d^96s6p$ ^{4}D°	5/2	$5d^{10}14d$ ^{2}D	5/2	Broad	New
90	370.05(05)	370.06	-0.01	$5d^96s6p$ ^{2}D°	5/2	$5d^96s6d$ 12	5/2	Bl. (Fe I)	PS
62	371.24(05)	371.25	-0.01	$5d^96s6p$ ^{4}D°	5/2	$5d^{10}13d$ ^{2}D	3/2	Bl. (O III)	New
92	379.58(05)	379.58	0.0	$5d^{10}6p$ ^{2}P°	3/2	$5d^{10}7d$ ^{2}D	5/2		PS
62	380.15(05)	380.17	-0.02	$5d^{10}6p$ ^{2}P°	3/2	$5d^{10}7d$ ^{2}D	3/2	Broad	PS
92	380.47(05)	380.47	0.0	$5d^96s6p$ ^{2}F°	7/2	$5d^96s7s$ 33	5/2	Obscured	New

Table 4.3 (cont'd)

Int.	λ_{exp}	λ_{Ritz}	$\Delta\lambda$	Lower Level	J_l	Upper Level	J_u	Note	Ref.
62	386.53(05)	386.52	0.01	$5d^96s6p$ ^{2}F$^\circ$	7/2	$5d^96s6d$ 12	5/2	Bl. (Fe I)	PS
92	389.81(05)	389.82	-0.01	$5d^96s6p$ ^{4}P$^\circ$	5/2	$5d^96s7s$ ^{4}D	7/2	Bl. (Fe I)	PS
62	392.78(06)	392.77	0.01	$5d^96s6p$ ^{4}D$^\circ$	7/2	$5d^96s6d$ 25	9/2	Bl. (Fe I)	ED
93	398.67(05)	398.67	0.0	$5d^96s6p$ ^{2}D$^\circ$	5/2	$5d^96s6d$ 8 (29)	7/2	Bl. (Fe II)	PS
93	399.12(08)	399.12	0.0	$5d^96s6p$ ^{4}F$^\circ$	5/2	$5d^96s7s$ ^{2}D	5/2	Broad	PS
93	399.12(08)	399.16	-0.04	$5d^96s6p$ ^{2}D$^\circ$	3/2	$5d^96s6d$ 5	3/2	Broad	PS
65	404.1(05)	404.11	-0.01	$5d^96s^2$ ^{2}D	3/2	$5d^96s6p$ ^{4}F$^\circ$	5/2	Bl. (Fe I)	PS
94	404.6(05)	404.6	0.0	$5d^96s6p$ ^{4}P$^\circ$	3/2	$5d^{10}11s$ ^{2}S	1/2	Bl. (Fe I)	New
69	406.46(05)	406.46	0.0	$5d^{10}6p$ ^{2}P$^\circ$	1/2	$5d^{10}6d$ ^{2}D	3/2	Bl. (Fe I)	New
95	408.4(05)	408.4	0.0	$5d^96s6p$ ^{4}F$^\circ$	5/2	$5d^96s7s$ ^{4}D	3/2	Bl. (Fe I)	PS
69	429.47(06)	429.47	0.0	$5d^96s6p$ ^{4}D$^\circ$	1/2	$5d^96s6d$ 14	3/2		PS
95	431.53(05)	431.53	0.0	$5d^96s6p$ ^{4}F$^\circ$	7/2	$5d^96s7s$ ^{4}D	5/2		PS
69	433.34(05)	433.36	-0.02	$5d^96s6p_{1/2}$ ^{2}F$^\circ$	5/2	$5d^96s6d$ 17	3/2		PS
95	448.96(06)	448.93	0.03	$5d^96s6p$ ^{2}D$^\circ$	3/2	$5d^{10}14d$ ^{2}D	3/2	Bl. (Fe I)	New
69	452.82(05)	452.82	0.0	$5d^96s6p$ ^{2}D$^\circ$	3/2	$5d^{10}13d$ ^{2}D	3/2		New
95	455.83(06)	455.84	-0.01	$5d^96s6p$ ^{2}D$^\circ$	3/2	$5d^{10}14s$ ^{2}S	1/2	Bl. (Cr II)	New
69	472.16(06)	472.17	-0.01	$5d^96s6p$ ^{4}D$^\circ$	1/2	$5d^96s6d$ 10	3/2	Bl. (Fe I)	PS
99	479.26(05)	479.25	0.01	$5d^{10}6p$ ^{2}P$^\circ$	3/2	$5d^{10}6d$ ^{2}D	5/2	Obscured	PS
69	482.93(05)	482.94	-0.01	$5d^96s6p$ ^{2}F$^\circ$	7/2	$5d^{10}14d$ ^{2}D	5/2		New
99	486.62(05)	486.6	0.02	$5d^96s6p$ ^{4}D$^\circ$	1/2	$5d^96s6d$ 5	3/2	Broad	New
70	493.63(06)	493.63	0.0	$5d^96s6p$ ^{2}F$^\circ$	7/2	$5d^{10}12d$ ^{2}D	5/2	Bl. (Cr I)	New
99	495.75(05)	495.75	0.0	$5d^96s6p$ ^{2}P$^\circ$	3/2	$5d^96s6d$ 14	3/2	Bl. (Fe I)	PS
70	506.77(05)	506.77	0.0	$5d^96s6p$ ^{2}D$^\circ$	5/2	$5d^{10}9d$ ^{2}D	5/2	Bl. (Fe II)	New
99	523.01(05)	523.01	0.0	$5d^96s6p$ ^{4}F$^\circ$	9/2	$5d^96s7s$ ^{4}D	7/2		PS

Table 4.3 (cont'd)

Int.	λ_{exp}	λ_{Ritz}	$\Delta\lambda$	Lower Level	J_l	Upper Level	J_u	Note	Ref.
70	549.99(05)	549.97	0.02	$5d^96s6p_{1/2}$ ^{2}F°	5/2	$5d^96s6d$ 31	3/2		New
70	550.56(07)	550.55	0.01	$5d^96s6p$ ^{4}P°	1/2	$5d^{10}9d$ ^{2}D	3/2	Broad	New
70	550.56(07)	550.56	0.0	$5d^96s6p_{1/2}$ ^{2}F°	5/2	$5d^96s6d$ 30	5/2	Broad	New
100	553.18(05)	553.18	0.0	$5d^96s6p$ ^{2}P°	3/2	$5d^96s6d$ 16	5/2		PS
70	572.91(05)	572.91	0.0	$5d^96s6p$ ^{2}D°	3/2	$5d^{10}9s$ ^{2}S	1/2		New
100	586.15(06)	586.13	0.02	$5d^96s6p$ ^{4}D°	3/2	$5d^{10}14s$ ^{2}S	1/2		New
71	589.82(05)	589.83	-0.01	$5d^96s6p$ ^{4}D°	3/2	$5d^{10}12d$ ^{2}D	5/2	Bl. (Fe II)	New
100	595.7(05)	595.69	0.01	$5d^96s6p$ ^{4}D°	7/2	$5d^96s7s$ ^{4}D	7/2		PS
71	621.93(05)	621.93	0.0	$5d^96s6p$ ^{2}P°	3/2	$5d^96s7s$ 33	5/2	Bl. (Fe I)	New
100	623.03(05)	623.03	0.0	$5d^{10}7p$ ^{2}P°	3/2	$5d^96s6d$ 30	5/2		New
71	627.78(05)	627.77	0.01	$5d^96s^2$ ^{2}D	3/2	$5d^{10}6p$ ^{2}P°	1/2		PS
100	639.96(05)	639.97	-0.01	$5d^96s6p$ ^{4}D°	1/2	$5d^{10}9d$ ^{2}D	3/2	Bl. (Fe I, N II)	New
71	721.01(05)	721.01	0.0	$5d^96s6p$ ^{4}D°	3/2	$5d^{10}8d$ ^{2}D	3/2		New
100	735.35(06)	735.35	0.0	$5d^96s6p_{3/2}$ ^{2}F°	5/2	$5d^{10}13d$ ^{2}D	3/2		New
71	749.34(05)	749.33	0.01	$5d^96s6p_{3/2}$ ^{2}F°	5/2	$5d^{10}12d$ ^{2}D	5/2		New
100	749.53(05)	749.53	0.0	$5d^96s6p_{3/2}$ ^{2}F°	5/2	$5d^{10}12d$ ^{2}D	3/2	Obscured	PS
72	751.08(05)	751.08	0.0	$5d^{10}6p$ ^{2}P°	3/2	$5d^{10}7s$ ^{2}S	1/2		PS
100	753.24(05)	753.24	0.0	$5d^96s6p$ ^{2}P°	3/2	$5d^96s6d$ 5	3/2	Broad	New

Table 4.4. Energy levels in Au I. Level energies and experimental uncertainties are reported in units of cm^{-1}, and the literature values are taken from the listed references. Where possible, level labels have been updated according to the NIST database [43]. All energies and uncertainties presented with respect to the ground term. Levels fixed in the level optimization are denoted by an uncertainty of 0.005 cm^{-1}.

Level	E_{exp}	E_{lit}	$(E_{exp} - E_{lit})$	Number of Lines	Reference
$5d^{10}6s\ ^2S_{1/2}$	0.0	0.0	0.0	3	ED
$5d^96s^2\ ^2D_{5/2}$	9161 ± 5	9161.3	-0.3	8	ED
$5d^96s^2\ ^2D_{3/2}$	21435 ± 4	21435.19	-0.6	4	ED
$5d^{10}6p\ ^2P^\circ_{1/2}$	37360 ± 4	37358.9	0.6	6	ED
$5d^{10}6p\ ^2P^\circ_{3/2}$	41174 ± 4	41174.61	-0.9	8	ED
$5d^96s6p\ ^4P^\circ_{5/2}$	42164 ± 5	42163.53	0.6	5	ED
$5d^96s6p\ ^4F^\circ_{7/2}$	45537 ± 6	45537.19	-0.2	2	ED
$5d^96s6p\ ^4F^\circ_{5/2}$	46173 ± 4	46174.98	-1.9	5	ED
$5d^96s6p\ ^4D^\circ_{5/2}$	46380 ± 5	46379.0	0.5	6	PS
$5d^96s6p\ ^4P^\circ_{3/2}$	47006 ± 7	47007.43	-1.4	3	ED
$5d^96s6p\ ^4F^\circ_{9/2}$	48695 ± 6	48697.15	-2.5	1	ED
$5d^96s6p\ ^4D^\circ_{7/2}$	51027 ± 6	51028.89	-1.8	3	ED
$5d^96s6p\ ^2D^\circ_{3/2}$	51230 ± 5	51231.53	-1.2	5	ED
$5d^96s6p\ ^4F^\circ_{3/2}$	51484 ± 6	51485.0	-1.0	2	PS
$5d^96s6p\ ^2D^\circ_{5/2}$	51652 ± 5	51653.46	-1.8	3	ED
$5d^96s6p\ ^2F^\circ_{7/2}$	52802 ± 4	52802.1	0.0	6	ED
$5d^96s6p\ ^4P^\circ_{1/2}$	53194 ± 5	53196.32	-2.4	2	BG
$5d^{10}7s\ ^2S_{1/2}$	54484 ± 4	54485.24	-1.1	1	ED
$5d^96s6p\ ^4D^\circ_{1/2}$	55731 ± 4	55732.61	-1.5	4	ED
$5d^96s6p\ ^4D^\circ_{3/2}$	56105 ± 5	56105.75	-0.7	2	ED
$5d^96s6p_{1/2}\ ^2F^\circ_{5/2}$	58615 ± 2	58616.76	-1.9	2	ED
$5d^96s6p\ ^2P^\circ_{3/2}$	58843 ± 5	58845.41	-2.3	3	ED
$5d^96s6p_{3/2}\ ^2F^\circ_{5/2}$	59713 ± 4	59713.2	-0.4	3	PS
$5d^{10}7p\ ^2P^\circ_{1/2}$		60032.85		0	BG

128

Table 4.4 (cont'd)

Level	E_{exp}	E_{lit}	$(E_{exp} - E_{lit})$	Number of Lines	Reference
$5d^{10}7p\ ^2\text{P}^\circ_{3/2}$	60727 ± 4	60728.49	-1.6	1	BG
$5d^96s6p\ ^2\text{D}^\circ_{5/2}$		61255.57		0	ED
$5d^96s6p\ ^2\text{D}^\circ_{3/2}$		61563.3		0	PS
$5d^{10}6d\ ^2\text{D}_{3/2}$	61955 ± 5	61951.89	3.1	1	ED
$5d^{10}6d\ ^2\text{D}_{5/2}$	62034 ± 5	62034.36	-0.8	1	ED
$5d^96s6p\ ^2\text{P}^\circ_{3/2}$	63004 ± 4	63005.1	-1.4	3	PS
$5d^{10}8s\ ^2\text{S}_{1/2}$		64742.9		0	ED
$5d^{10}8p\ ^2\text{P}^\circ_{1/2}$		66605.3		0	PS
$5d^{10}8p\ ^2\text{P}^\circ_{3/2}$		66910.3		0	PS
$5d^{10}7d\ ^2\text{D}_{3/2}$	67470 ± 5	67469.68	0.3	2	ED
$5d^{10}5f\ ^2\text{F}^\circ_{7/2}$		67485.3		0	PS
$5d^{10}5f\ ^2\text{F}^\circ_{5/2}$	67485 ± 11	67490.0	-5.0	1	PS
$5d^{10}7d\ ^2\text{D}_{5/2}$	67511 ± 6	67510.6	0.4	1	ED
$5d^96s7s\ ^4\text{D}_{7/2}$	67810 ± 6	67811.33	-1.7	2	ED
$5d^{10}9s\ ^2\text{S}_{1/2}$	68680 ± 5	68680.63	-0.3	1	ED
$5d^96s7s\ ^4\text{D}_{5/2}$	68704 ± 7	68705.05	-1.1	1	ED
$5d^{10}8d\ ^2\text{D}_{3/2}$	69971 ± 5	69971.42	-0.8	1	ED
$5d^{10}8d\ ^2\text{D}_{5/2}$		70007.98		0	ED
$5d^{10}10s\ ^2\text{S}_{1/2}$		70617.73		0	ED
$5d^96s7s\ ^4\text{D}_{3/2}$	70652 ± 5	70653.25	-1.2	1	ED
$5d^96s7s\ ^2\text{D}_{5/2}$	71221 ± 7	71222.93	-1.9	1	ED
$5d^{10}9d\ ^2\text{D}_{3/2}$	71353 ± 4	71354.95	-2.3	2	ED
$5d^{10}9d\ ^2\text{D}_{5/2}$	71379 ± 6	71380.71	-1.7	2	ED
$5d^{10}11s\ ^2\text{S}_{1/2}$	71715 ± 7	71714.39	0.6	1	ED

129

Table 4.4 (cont'd)

Level	E_{exp}	E_{lit}	$(E_{exp} - E_{lit})$	Number of Lines	Reference
$5d^{10}10d$ $^2\mathrm{D}_{3/2}$		72163.35		0	ED
$5d^{10}10d$ $^2\mathrm{D}_{5/2}$		72170.99		0	ED
$5d^{10}12s$ $^2\mathrm{S}_{1/2}$		72395.9		0	PS
$5d^{10}11d$ $^2\mathrm{D}_{3/2}$		72690.1		0	PS
$5d^{10}11d$ $^2\mathrm{D}_{5/2}$	72696 ± 7	72694.8	1.6	1	PS
$5d^{10}13s$ $^2\mathrm{S}_{1/2}$		72847.5		0	PS
$5d^{10}12d$ $^2\mathrm{D}_{3/2}$	73051 ± 4	73050.9	-0.1	4	ED
$5d^{10}12d$ $^2\mathrm{D}_{5/2}$	73054 ± 4	73054.8	-0.4	3	PS
$5d^{10}14s$ $^2\mathrm{S}_{1/2}$	73162 ± 5	73162.1	-0.6	3	PS
$5d^{10}13d$ $^2\mathrm{D}_{3/2}$	73308 ± 4	73308.98	-0.9	3	ED
$5d^{10}13d$ $^2\mathrm{D}_{5/2}$		73312.6		0	PS
$5d^{10}14d$ $^2\mathrm{D}_{3/2}$	73499 ± 5	73500.4	-1.4	2	PS
$5d^{10}14d$ $^2\mathrm{D}_{5/2}$	73503 ± 5	73502.5	0.5	2	PS
$5d^9 6s6d$ $5_{3/2}$	76276 ± 4	76278.0	-2.0	4	PS
$5d^9 6s6d$ $25_{9/2}$	76480 ± 6	76481.95	-1.9	2	ED
$5d^9 6s6d$ 6 $(26)_{5/2}$	76566 ± 7	76566.22	-0.2	2	ED
$5d^9 6s6d$ $27_{3/2}$	76566 ± 7	76568.07	-2.1	2	ED
$5d^9 6s6d$ 7 $(28)_{11/2}$		76569.73		0	ED
$5d^9 6s6d$ 8 $(29)_{7/2}$	76728 ± 6	76731.99	-4.0	1	ED
$5d^9 6s6d$ $30_{5/2}$	76773 ± 3	76774.6	-1.5	1	ED
$5d^9 6s6d$ $31_{3/2}$	76793 ± 3	76793.11	-0.5	3	ED
$5d^9 6s6d$ 9 $(32)_{9/2}$		76829.8		0	ED
$5d^9 6s6d$ $10_{3/2}$	76904 ± 5	76906.4	-2.4	2	PS
$5d^9 6s6d$ $11_{5/2}$	76957 ± 7	76955.0	2.0	1	PS

Table 4.4 (cont'd)

Level	E_{exp}	E_{lit}	$(E_{exp} - E_{lit})$	Number of Lines	Reference
$5d^9 6s6d\ 12_{5/2}$	78667 ± 5	78667.8	-0.9	4	PS
$5d^9 6s6d\ 13_{3/2}$	78819 ± 5	78819.9	-0.9	2	PS
$5d^9 6s6d\ 14_{3/2}$	79009 ± 5	79010.2	-1.3	3	PS
$5d^9 6s7s\ 33_{5/2}$	79078 ± 4	79080.3	-2.1	4	ED
$5d^9 6s6d\ 15_{5/2}$	80768 ± 7	80772.7	-4.7	2	PS
$5d^9 6s6d\ 16_{5/2}$	81076 ± 5	81076.8	-0.8	2	PS
$5d^9 6s6d\ 17_{3/2}$	81684 ± 0.005	81683.7	0.0	1	PS
$5d^9 6s7s\ 34_{3/2}$		86507.68		0	ED

Table 4.5.   Observed transitions in Au II. Air wavelengths and uncertainties (in parentheses) are reported in nm. The intensities are normalized to a 0 - 100 scale. Level labels are taken from [108] and where possible are updated by those in the NIST ASD [43]. Ritz wavelengths are calculated from the experimental level energies in Table 4.8. Wavelength ranges are indicated by the additional horizontal bars.

Int.	λ_{exp}	λ_{Ritz}	$\Delta\lambda$	Lower Level	J_l	Upper Level	J_u	Note	Ref.
1	197.8(05)	197.77	0.03	$5d^86s^2$ ^{3}F	3	$5d^8(^3$P$)6s6p$ ^{5}P°	3		New
0	200.11(05)	200.1	0.01	$5d^96s$ ^{3}D	3	$5d^96p$ $(5/2,1/2)°$	3	Bl. (Fe II)	RW
1	204.06(05)	204.04	0.02	$5d^86s^2$ ^{3}P	0	$5d^86s6p$ $5°$	1		RW
0	204.29(05)	204.29	0.0	$5d^86s^2$ ^{1}G	4	$5d^8(^3$F$)6s6p$ ^{1}G°	4	Bl. (O II)	New
1	204.48(05)	204.46	0.02	$5d^96s$ ^{3}D	1	$5d^96p$ $(3/2,1/2)°$	2	Broad	RW
1	208.27(05)	208.21	0.06	$5d^96s$ ^{3}D	3	$5d^96p$ $(5/2,1/2)°$	2	Bl. (Au III)	RW
1	219.04(05)	219.05	-0.01	$5d^96s$ ^{3}D	1	$5d^96p$ $(5/2,3/2)°$	1		PS
1	228.3(07)	228.32	-0.02	$5d^86s^2$ ^{3}P	2	$5d^86s6p$ $2°$	3		RW
1	228.3(07)	228.3	0.0	$5d^96s$ ^{1}D	2	$5d^96p$ $(5/2,3/2)°$	1		RW
1	229.11(08)	229.09	0.02	$5d^8(^3$F$)6s6p$ ^{5}D°	3	$5d^96d$ $(3/2,5/2)$	2	Bl. (O II, C III)	PS
1	229.11(08)	229.1	0.01	$5d^96p$ $(5/2,1/2)°$	3	$5d^97s$ $(5/2,1/2)$	2	Bl. (O II, C III)	PS
1	230.45(07)	230.48	-0.03	$5d^96p$ $(5/2,3/2)°$	3	$5d^96d$ $(5/2,5/2)$	4		RW
1	230.45(07)	230.48	-0.03	$5d^8(^3$F$)6s6p$ ^{5}D°	3	$5d^96d$ $(3/2,5/2)$	4		RW
2	230.75(05)	230.75	0.0	$5d^86s^2$ ^{1}D	2	$5d^8(^3$P$)6s6p$ ^{5}S°	2	Bl. (Fe II)	New
2	234.05(07)	234.0	0.05	$5d^96p$ $(5/2,3/2)°$	3	$5d^96d$ $(5/2,3/2)$	3	Broad	RW
2	234.05(07)	234.02	0.03	$5d^96p$ $(3/2,3/2)°$	2	$5d^96d$ $(3/2,3/2)$	1	Broad	RW
2	236.45(05)	236.48	-0.03	$5d^96p$ $(5/2,3/2)°$	3	$5d^96d$ $(5/2,3/2)$	2		RW
2	237.35(05)	237.35	0.0	$5d^86s^2$ ^{3}F	2	$5d^8(^3$P$)6s6p$ ^{5}P°	1		New
18	242.76(05)	242.76	0.0	$5d^86s6p$ $2°$	3	$5d^98s$ $(5/2,1/2)$	3	Bl. (Au I, Fe II)	New
2	245.84(05)	245.84	0.0	$5d^86s^2$ ^{3}P	1	$5d^86s6p$ $5°$	2		New
19	249.29(05)	249.25	0.04	$5d^86s^2$ ^{3}F	2	$5d^8(^3$P$)6s6p$ ^{5}D°	1	Bl. (Fe II)	RW
2	253.35(05)	253.36	-0.01	$5d^96p$ $(3/2,1/2)°$	1	$5d^97s$ $(3/2,1/2)$	2	Broad	RW
19	253.8(05)	253.78	0.02	$5d^96p$ $(3/2,1/2)°$	2	$5d^96d$ $(5/2,3/2)$	1	Broad	PS
2	255.14(05)	255.14	0.0	$5d^8(^3$P$)6s6p$ ^{5}P°	2	$5d^96d$ $(3/2,3/2)$	3		PS

132

Table 4.5 (cont'd)

Int.	λ_{exp}	λ_{Ritz}	$\Delta\lambda$	Lower Level	J_l	Upper Level	J_u	Note	Ref.
19	256.85(05)	256.87	-0.02	$5d^8(^3P)6s6p\ ^5P^\circ$	2	$5d^96d\ (3/2,3/2)$	1		New
4	258.93(05)	258.94	-0.01	$5d^96p\ (3/2,1/2)^\circ$	1	$5d^96d\ (5/2,5/2)$	0		RW
44	260.95(05)	260.97	-0.02	$5d^86s^2\ ^3P$	2	$5d^8(^3F)6s6p\ ^5D^\circ$	3	Bl. (Fe I)	New
19	261.76(05)	261.76	0.0	$5d^86s^2\ ^3F$	3	$5d^8(^3P)6s6p\ ^5P^\circ$	2	Bl. (Fe II)	New
59	262.5(05)	262.5	0.0	$5d^86s^2\ ^1G$	4	$5d^86s6p\ 4^\circ$	4	Bl. (Fe II)	New
22	262.76(05)	262.73	0.03	$5d^86s^2\ ^3P$	2	$5d^96p\ (3/2,3/2)^\circ$	2	Bl. (Fe II)	RW
62	272.15(06)	272.15	0.0	$5d^8(^1D)6s6p\ ^3F^\circ$	2	$5d^96d\ (3/2,3/2)$	2		New
31	277.51(05)	277.52	-0.01	$5d^8(^1D)6s6p\ ^3F^\circ$	2	$5d^96d\ (3/2,3/2)$	3		New
62	278.11(06)	278.11	0.0	$5d^86s^2\ ^3F$	3	$5d^8(^3F)6s6p\ ^5G^\circ$	4	Bl. (Fe I, N II)	RW
38	280.9(06)	280.9	0.0	$5d^8(^3F)6s6p\ ^5D^\circ$	2	$5d^96d\ (3/2,5/2)$	3	Broad	New
65	282.41(06)	282.4	0.01	$5d^96p\ (3/2,1/2)^\circ$	1	$5d^96d\ (5/2,3/2)$	2		New
38	291.39(05)	291.39	0.0	$5d^86s^2\ ^3F$	4	$5d^96p\ (5/2,3/2)^\circ$	3	Broad	RW
69	292.96(05)	292.96	0.0	$5d^8(^3F)6s6p\ ^5D^\circ$	2	$5d^96d\ (3/2,3/2)$	1	Bl. (Fe I)	New
38	306.6(05)	306.6	0.0	$5d^86s6p\ 5^\circ$	3	$5d^98s\ (5/2,1/2)$	3		New
69	307.04(05)	307.04	0.0	$5d^86s6p\ 4^\circ$	3	$5d^96d\ (3/2,5/2)$	2		New
38	307.96(05)	307.95	0.01	$5d^96p\ (3/2,3/2)^\circ$	3	$5d^96d\ (5/2,5/2)$	4		New
69	308.96(06)	308.96	0.0	$5d^86s6p\ 4^\circ$	3	$5d^96d\ (3/2,3/2)$	2	Broad	New
38	310.84(05)	310.81	0.03	$5d^8(^3P)6s6p\ ^5D^\circ$	1	$5d^96d\ (3/2,5/2)$	2		New
78	312.29(05)	312.29	0.0	$5d^86s^2\ ^3F$	4	$5d^96p\ (5/2,3/2)^\circ$	4		RW
38	317.3(05)	317.3	0.0	$5d^96p\ (3/2,1/2)^\circ$	2	$5d^97s\ (5/2,1/2)$	3		RW
79	323.08(05)	323.08	0.0	$5d^96p\ (3/2,3/2)^\circ$	2	$5d^96d\ (5/2,3/2)$	3		PS
38	325.11(05)	325.1	0.01	$5d^8(^3P)6s6p\ ^5P^\circ$	2	$5d^97s\ (3/2,1/2)$	2		RW
79	325.33(05)	325.33	0.0	$5d^96p\ (3/2,3/2)^\circ$	2	$5d^96d\ (5/2,5/2)$	1		New
38	327.84(06)	327.83	0.01	$5d^96p\ (3/2,3/2)^\circ$	2	$5d^96d\ (5/2,3/2)$	2	Obscured	New

Table 4.5 (cont'd)

Int.	λ_{exp}	λ_{Ritz}	$\Delta\lambda$	Lower Level	J_l	Upper Level	J_u	Note	Ref.
79	330.6(05)	330.6	0.0	$5d^8(^3F)6s6p\ ^5D^\circ$	3	$5d^96d\ (5/2,3/2)$	2	Bl. (Fe I)	New
38	338.72(05)	338.71	0.01	$5d^86s^2\ ^1D$	2	$5d^8(^3P)6s6p\ ^5P^\circ$	1		New
79	356.47(05)	356.48	-0.01	$5d^86s6p\ 5^\circ$	2	$5d^96d\ (3/2,5/2)$	2	Bl. (Fe I)	New
38	362.09(05)	362.09	0.0	$5d^8(^3P)6s6p\ ^5P^\circ$	2	$5d^96d\ (5/2,5/2)$	3		New
79	363.06(05)	363.04	0.02	$5d^8(^3P)6s6p\ ^5P^\circ$	3	$5d^96d\ (3/2,3/2)$	2	Bl. (Fe I)	New
39	363.4(05)	363.39	0.01	$5d^86s^2\ ^3F$	2	$5d^96p\ (3/2,3/2)^\circ$	3	Bl. (Fe I)	PS
79	363.6(05)	363.58	0.02	$5d^86s6p\ 5^\circ$	2	$5d^96d\ (3/2,5/2)$	1		New
39	363.88(05)	363.86	0.02	$5d^8(^3P)6s6p\ ^5P^\circ$	3	$5d^96d\ (3/2,5/2)$	4		New
79	374.37(06)	374.38	-0.01	$5d^8(^3P)6s6p\ ^5D^\circ$	4	$5d^96d\ (3/2,3/2)$	3		New
80	386.53(07)	386.55	-0.02	$5d^86s6p\ 2^\circ$	3	$5d^96d\ (5/2,5/2)$	4	Bl. (Fe I)	New
80	386.53(07)	386.49	0.04	$5d^8(^3F)6s6p\ ^5G^\circ$	2	$5d^96d\ (3/2,5/2)$	2	Bl. (Fe I)	New
39	394.83(05)	394.85	-0.02	$5d^8(^3F)6s6p\ ^5G^\circ$	2	$5d^96d\ (3/2,5/2)$	1		New
80	404.89(05)	404.89	0.0	$5d^8(^3F)6s6p\ ^5G^\circ$	2	$5d^96d\ (3/2,3/2)$	1		New
40	406.15(05)	406.15	0.0	$5d^8(^3F)6s6p\ ^5F^\circ$	1	$5d^96d\ (3/2,5/2)$	2	Obscured	New
81	408.36(05)	408.37	-0.01	$5d^86s^2\ ^3F$	3	$5d^96p\ (3/2,1/2)^\circ$	2		ED
40	411.15(05)	411.15	0.0	$5d^86s^2\ ^1G$	4	$5d^96p\ (3/2,3/2)^\circ$	3		PS
81	432.58(05)	432.59	-0.01	$5d^86s^2\ ^3P$	0	$5d^96p\ (3/2,1/2)^\circ$	1	Bl. (Fe I, O II)	New
40	435.96(05)	435.96	0.0	$5d^96p\ (3/2,3/2)^\circ$	3	$5d^97s\ (5/2,1/2)$	2		New
81	446.96(05)	446.95	0.01	$5d^86s6p\ 5^\circ$	1	$5d^96d\ (3/2,5/2)$	1	Bl. (Fe I)	New
40	484.43(05)	484.42	0.01	$5d^86s6p\ 9^\circ$	3	$5d^96d\ (3/2,5/2)$	4		New
81	492.06(05)	492.06	0.0	$5d^86s^2\ ^3F$	3	$5d^96p\ (5/2,3/2)^\circ$	4	Bl. (Fe I)	New
41	501.29(05)	501.3	-0.01	$5d^96d\ (5/2,3/2)$	1	$5d^97p\ (3/2,3/2)^\circ$	2	Broad	New
81	506.71(05)	506.71	0.0	$5d^8(^3P)6s6p\ ^5D^\circ$	1	$5d^96d\ (5/2,5/2)$	2		New
41	540.93(05)	540.93	0.0	$5d^96d\ (5/2,3/2)$	3	$5d^97p\ (3/2,3/2)^\circ$	2		New

Table 4.5 (cont'd)

Int.	λ_{exp}	λ_{Ritz}	$\Delta\lambda$	Lower Level	J_l	Upper Level	J_u	Note	Ref.
81	541.34(05)	541.34	0.0	$5d^86s^2$ ^{3}F	2	$5d^96p$ $(3/2,1/2)^\circ$	2		PS
41	578.09(05)	578.09	0.0	$5d^96d$ $(5/2,3/2)$	1	$5d^97p$ $(3/2,1/2)^\circ$	1		New
82	612.19(05)	612.19	0.0	$5d^86s6p$ 2°	3	$5d^97s$ $(5/2,1/2)$	2		New
41	623.03(05)	623.02	0.01	$5d^96d$ $(5/2,5/2)$	1	$5d^97p$ $(3/2,1/2)^\circ$	1		New
82	660.47(05)	660.47	0.0	$5d^86s6p$ 12°	3	$5d^96d$ $(3/2,5/2)$	2		New
41	703.21(05)	703.21	0.0	$5d^97p$ $(5/2,1/2)^\circ$	2	$5d^98s$ $(5/2,1/2)$	2		New
82	717.23(05)	717.22	0.01	$5d^86s6p$ 12°	2	$5d^96d$ $(3/2,3/2)$	1		New
41	733.4(05)	733.4	0.0	$5d^86s6p$ 5°	2	$5d^96d$ $(5/2,3/2)$	1		New
83	764.66(05)	764.66	0.0	$5d^96d$ $(5/2,5/2)$	0	$5d^97p$ $(3/2,1/2)^\circ$	1	Bl. (Fe II)	New

Table 4.6. Energy levels in Au II. Level energies and experimental uncertainties are reported with respect to the ground term in units of cm^{-1} , and the literature energies and labels are taken from [108]. Where possible, the level labels have been updated according to the NIST database [43]. Levels fixed in the level optimization are denoted by an uncertainty of 0.005 cm^{-1}.

Level	E_{exp}	E_{lit}	$(E_{exp} - E_{lit})$	Number of Lines
$5d^{10}$ $^1S_0$	0.0	0.0	0.0	0
$5d^96s$ $^3D_3$	15040 ± 0.005	15039.57	0.0	3
$5d^96s$ $^3D_2$		17640.62		0
$5d^96s$ $^3D_1$	27766 ± 0	27765.76	0.0	3
$5d^96s$ $^1D_2$	29615 ± 14	29621.25	-6.25	1
$5d^86s^2$ $^3F_4$	40483 ± 6	40478.75	4.25	2
$5d^86s^2$ $^3P_2$	48519 ± 6	48510.89	8.11	3
$5d^86s^2$ $^3F_3$	52178 ± 3	52176.51	1.99	4
$5d^86s^2$ $^3F_2$	58192 ± 0.005	58191.63	0.0	3
$5d^86s^2$ $^3P_0$	58554 ± 6	58550.23	3.77	2
$5d^86s^2$ $^1G_4$	61387 ± 5	61384.0	3.0	1
$5d^86s^2$ $^3P_1$	61756 ± 9	61749.42	6.58	1
$5d^96p$ $(5/2,1/2)^\circ_2$	63053 ± 0.005	63053.32	0.0	2
$5d^96p$ $(5/2,1/2)^\circ_3$	64998 ± 10	65003.59	-5.59	2
$5d^86s^2$ $^1G_4$	65307 ± 0.005	65307.0	0.0	0
$5d^86s^2$ $^1D_2$	70795 ± 11	70797.19	-2.19	1
$5d^96p$ $(5/2,3/2)^\circ_4$	72496 ± 4	72495.13	0.47	2
$5d^96p$ $(5/2,3/2)^\circ_2$	73178 ± 0.005	73178.29	0.0	0
$5d^96p$ $(5/2,3/2)^\circ_1$	73404 ± 0.005	73403.84	0.0	2
$5d^96p$ $(5/2,3/2)^\circ_3$	74791 ± 6	74791.48	-0.48	4
$5d^96p$ $(3/2,1/2)^\circ_2$	76659 ± 2	76659.7	-0.5	4
$5d^96p$ $(3/2,1/2)^\circ_1$	81664 ± 5	81659.83	4.27	4
$5d^96p$ $(3/2,3/2)^\circ_0$		82613.78		0
$5d^96p$ $(3/2,3/2)^\circ_3$	85702 ± 4	85700.2	2.0	3

Table 4.6 (cont'd)

Level	E_{exp}	E_{lit}	$(E_{exp} - E_{lit})$	Number of Lines
$5d^9 6p\ (3/2,3/2)^\circ{}_1$		85707.57		0
$5d^9 6p\ (3/2,3/2)^\circ{}_2$	86570 ± 4	86565.67	4.33	5
$5d^8(^3F)6s6p\ ^5D^\circ{}_3$	86826 ± 6	86821.34	4.66	4
$5d^8(^3F)6s6p\ ^5G^\circ{}_4$	88125 ± 8	88126.5	-1.5	1
$5d^8(^3P)6s6p\ ^5P^\circ{}_2$	90370 ± 5	90371.0	-0.8	4
$5d^8 6s6p\ 2^\circ{}_3$	92303 ± 4	92301.33	2.07	3
$5d^8(^1D)6s6p\ ^3F^\circ{}_2$	93529 ± 8	93531.21	-2.21	2
$5d^8(^1D)6s6p\ ^3D^\circ{}_1$	93830 ± 0.005	93830.26	0.0	0
$5d^8(^3F)6s6p\ ^5D^\circ{}_2$	95164 ± 8	95160.92	3.08	1
$5d^8(^3F)6s6p\ ^5F^\circ{}_4$		96346.88		0
$5d^8(^3F)6s6p\ ^5G^\circ{}_3$		97155.64		0
$5d^8 6s6p\ 4^\circ{}_3$	97905 ± 5	97904.9	0.1	2
$5d^8(^3P)6s6p\ ^5D^\circ{}_1$	98300 ± 5	98298.7	1.3	2
$5d^8 6s6p\ 4^\circ{}_4$	99471 ± 9	99474.27	-3.27	1
$5d^8(^3P)6s6p\ ^5P^\circ{}_1$	100310 ± 10	100316.97	-6.87	1
$5d^8 6s6p\ 5^\circ{}_3$	100878 ± 11	100883.84	-5.84	1
$5d^8(^3F)6s6p\ ^5F^\circ{}_2$		101637.14		0
$5d^8 6s6p\ 5^\circ{}_2$	102420 ± 3	102418.67	1.53	3
$5d^8(^3P)6s6p\ ^5P^\circ{}_3$	102725 ± 6	102726.7	-1.7	3
$5d^8(^3P)6s6p\ ^5D^\circ{}_4$	102849 ± 9	102857.48	-8.48	1
$5d^8(^3F)6s6p\ ^5G^\circ{}_2$	104598 ± 4	104596.85	0.85	3
$5d^8(^3F)6s6p\ ^5F^\circ{}_1$	105850 ± 3	105846.56	3.44	1
$5d^8 6s6p\ 6^\circ{}_4$		106569.47		0
$5d^8(^3P)6s6p\ ^5D^\circ{}_3$		106713.41		0

Table 4.6 (cont'd)

Level	E_{exp}	E_{lit}	$(E_{exp} - E_{lit})$	Number of Lines
5d^8(^{3}F)6s6p ^{5}F$^\circ_3$		107238.04		0
5d^8(^{3}F)6s6p ^{1}D$^\circ_2$		107239.34		0
5d^{8}6s6p 5$^\circ_1$	107549 $\pm$ 4	107551.05	-2.05	2
5d^{9}7s (5/2,1/2)$_3$	108166 $\pm$ 5	108172.95	-6.95	1
5d^{9}7s (5/2,1/2)$_2$	108634 $\pm$ 4	108631.44	2.16	3
5d^{8}6s6p 9$^\circ_3$	109563 $\pm$ 7	109560.95	1.75	1
5d^8(^{3}P)6s6p ^{5}D$^\circ_2$		109565.33		0
5d^{8}6s6p 9$^\circ_2$		110273.09		0
5d^{8}6s6p 8$^\circ_4$		110645.77		0
5d^8(^{3}P)6s6p ^{1}P$^\circ_1$		111170.45		0
5d^8(^{1}G)6s6p ^{3}F$^\circ_4$		112010.36		0
5d^{8}6s6p 7$^\circ_1$		112164.17		0
5d^8(^{1}D)6s6p ^{3}D$^\circ_3$		112424.94		0
5d^8(^{3}P)6s6p ^{5}S$^\circ_2$	114119 $\pm$ 15	114121.13	-2.13	1
5d^8(^{1}G)6s6p ^{3}F$^\circ_3$		114147.21		0
5d^8(^{3}F)6s6p ^{1}G$^\circ_4$	114241 $\pm$ 12	114245.88	-4.88	1
5d^{8}6s6p 8$^\circ_1$		114256.2		0
5d^{8}6s6p 11$^\circ_2$		114286.01		0
5d^{8}6s6p 12$^\circ_3$	115328 $\pm$ 1	115327.55	0.35	1
5d^{8}6s6p 12$^\circ_2$	115350 $\pm$ 5	115348.49	1.31	1
5d^{9}6d (5/2,3/2)$_1$	116052 $\pm$ 3	116050.55	1.05	4
5d^{8}6s6p 13$^\circ_2$		116722.52		0
5d^{9}6d (5/2,3/2)$_4$		116946.33		0
5d^{9}6d (5/2,3/2)$_2$	117065 $\pm$ 5	117065.63	-0.63	4

Table 4.6 (cont'd)

Level	E_{exp}	E_{lit}	$(E_{exp} - E_{lit})$	Number of Lines
$5d^96d$ $(5/2,5/2)_1$	117299 ± 4	117297.68	1.22	2
$5d^96d$ $(5/2,5/2)_5$		117346.06		0
$5d^96d$ $(5/2,3/2)_3$	117513 ± 4	117512.0	0.7	3
$5d^86s6p$ 13°_3		117661.73		0
$5d^86s6p$ 9°_1		117686.44		0
$5d^96d$ $(5/2,5/2)_3$	117980 ± 7	117983.17	-3.17	1
$5d^96d$ $(5/2,5/2)_2$	118030 ± 5	118029.27	0.53	1
$5d^96d$ $(5/2,5/2)_4$	118166 ± 5	118168.02	-2.02	3
$5d^86s6p$ 14°_3		118817.85		0
$5d^86s6p$ 10°_1		119365.19		0
$5d^97p$ $(5/2,1/2)^\circ_2$	119446 ± 0	119446.5	0.0	0
$5d^8(^3P)6s6p$ $^1D^\circ_2$		119891.66		0
$5d^97p$ $(5/2,1/2)^\circ_3$		120257.12		0
$5d^96d$ $(5/2,5/2)_0$	120271 ± 3	120269.51	1.59	2
$5d^97s$ $(3/2,1/2)_1$		120822.93		0
$5d^8(^1G)6s6p$ $^3F^\circ_2$		120951.33		0
$5d^97s$ $(3/2,1/2)_2$	121121 ± 6	121118.78	2.22	2
$5d^86s6p$ 11°_1		121862.08		0
$5d^86s6p$ 16°_2		121870.4		0
$5d^97p$ $(5/2,3/2)^\circ_4$		122656.19		0
$5d^86s6p$ 17°_2		122814.46		0
$5d^8(^1G)6s6p$ $^3G^\circ_4$		123062.9		0
$5d^97p$ $(5/2,3/2)^\circ_3$		123344.76		0
$5d^97p$ $(5/2,3/2)^\circ_2$		123605.66		0

Table 4.6 (cont'd)

Level	E_{exp}	E_{lit}	$(E_{exp} - E_{lit})$	Number of Lines
$5d^97p$ $(5/2,3/2)^\circ_2$		123605.66		0
$5d^86s6p$ 16°_3		124012.18		0
$5d^8(^1D)6s6p$ $^3D^\circ_2$		125103.78		0
$5d^86s6p$ 12°_1		125156.47		0
$5d^86s6p$ 17°_3		125241.2		0
$5d^7(^4F)6s^26p$ $^5D^\circ_4$		126661.8		0
$5d^86s6p$ 13°_1		127567.36		0
$5d^86s6p$ 19°_2		128001.87		0
$5d^86s6p$ 14°_1		128146.04		0
$5d^86s6p$ 18°_3		128317.31		0
$5d^96d$ $(3/2,3/2)_1$	129289 ± 4	129287.88	0.72	3
$5d^96d$ $(3/2,3/2)_3$	129552 ± 8	129560.54	-8.24	2
$5d^96d$ $(3/2,5/2)_1$	129916 ± 4	129918.2	-1.8	3
$5d^96d$ $(3/2,5/2)_4$	130200 ± 7	130198.66	1.34	2
$5d^96d$ $(3/2,3/2)_2$	130262 ± 6	130266.09	-4.09	3
$5d^86s6p$ 20°_2		130388.83		0
$5d^96d$ $(3/2,5/2)_2$	130464 ± 0.005	130464.45	0.0	5
$5d^96d$ $(3/2,5/2)_3$	130753 ± 11	130749.25	3.75	1
$5d^96d$ $(3/2,3/2)_0$		131563.73		0
$5d^8(^1G)6s6p$ $^1F^\circ_3$		132009.57		0
$5d^86s6p$ 15°_1	132511 ± 0.005	132510.92	0.0	0
$5d^97p$ $(3/2,1/2)^\circ_2$		132923.53		0
$5d^97p$ $(3/2,1/2)^\circ_1$	133345 ± 3	133344.72	0.48	3
$5d^98s$ $(5/2,1/2)_3$	133484 ± 10	133490.3	-6.3	1

Table 4.6 (cont'd)

Level	E_{exp}	E_{lit}	$(E_{exp} - E_{lit})$	Number of Lines
$5d^98s$ $(5/2,1/2)_2$	133663 ± 1	133663.79	-0.79	1
$5d^97p$ $(3/2,3/2)^{\circ}_2$	135994 ± 4	135993.77	0.53	2

Chapter 5

Conclusions and Outlook

5.1 Laboratory Studies of Charge Exchange

There remain open questions in astrophysics as to the density, temperature, and constituents of astrophysical plasmas. The bulk of astrophysical environments contain plasmas of ions, electrons, and neutrals. Interactions between the ions, electrons, and neutrals produce light, and the interpretation of astrophysical observations of this light can be enhanced by comparison with the available laboratory data of the relevant processes. For environments where charge exchange occurs, understanding the spectra requires charge exchange cross sections (relative or absolute, depending on context) for each combination of ion and neutral. The differing velocity dependence of these cross sections allows astrophysicists to understand the physical conditions found in the observed astrophysical plasmas. Knowing the energy, i.e. temperature, dependence allows one to extrapolate (or interpolate) to regions not tested in the laboratory. This improves astrophysical models.

Generally, *total* CX cross sections are measured using a gas cell where the density and extent of the target gas are well defined. However, such cells limit access to the interaction region for detecting photons or collision products. For *relative* cross sections, gas jets are often employed as both the collision products and photon yields are measurable. These two experimental approaches, gas cells and gas jets, were

developed for future use with the Clemson University EBIT. Two gas cell designs for measuring charge exchange cross sections of ion-neutral reactions were presented. The first gas cell, the "Manipulator Gas Cell" (MGC), is well suited for measuring charge exchange cross sections with large magnitudes typical of multi- to highly-charged ion projectiles. The design is centered around the use of an UHV manipulator for precisely aligning the axis of the cell with an incoming ion beam. The dimensions of the cell ensure a measurable decrease in ion beam current at reasonable target densities for CX reactions with large cross sections ($\sigma_{cx} > 10^{-15}$ cm^2).

We measured the total charge exchange cross sections for the symmetric reactions $A^+ + A \rightarrow A + A^+$ (A = He, Ne, Ar, Kr) between 0.2 - 5.0 keV [61, 62]. The measured cross sections are in agreement with previous experimental measurements and two theories [20, 21] in the literature. The absolute agreement in these experiments suggests that the target thickness PL, the product of the pressure and the effective path length of the neutral target, is well defined. The cross sections for the same ions and energies with molecular nitrogen (N$_2$) targets were also measured [63]. Assuming that the total scattering cross section may be written $\sigma_{scatter} = \sigma_{CX} + \sigma_{elastic} + \sigma_{inelastic}$, the contribution of non-CX scatter is inferred by comparing to the available literature. The collection angle of the ions in the MGC design ($\pm 13°$) and comparison to experiments with much greater collection angles in the literature suggests that both elastic and inelastic scatter are non-negligible at the energies studied here.

A second gas cell, referred to as the "(electrically) Floating Gas Cell" (FGC) was described which reduces the length of the experimental procedure for measuring CX cross sections. This gas cell is identical in size to the MGC design; however, the components of the cell are electrically isolated and can be floated between 0 - 2 kV. By setting the ion beam energy at the source high, the energy of the ion beam as it enters the target gas is adjusted by a single high voltage supply. The energy of the incoming ion beam is controlled by raising the deceleration voltage of the cell: $E_{ion} = |e|(V_{\text{source}} - V_{\text{decel}})$. Using this scheme, the total measurement duration is improved by a factor of 4 (1 hr $\rightarrow$ 15 min.), and a single ion-neutral combination may be measured in a single day.

When using multicharged ions from CUEBIT, the MGC would provide accu-

rate measurements of the total charge exchange cross sections for ions relevant to solar wind physics. In the literature, most experiments have focused on H_2 or He targets, and the total cross sections for some of the ion-neutral combinations are known. However, cross sections for atomic H, which are the simplest to calculate, are one of the most difficult to measure experimentally and remain of interest. In recent years, interest in collisions with water vapor targets (H_2O) has also grown following the discovery of H_2O around comets (see Ref. [4] and the references therein) but are difficult to measure in the laboratory.

In current form, the MGC design could be used for all commercially available gaseous targets. With modifications, the MGC design could also be used to measure CX cross sections for the difficult H or H_2O targets. When supplied by an external source (hydrogen cracker, water vapour source, etc.) it is unclear if these elements would survive the long journey to the interaction region. However, the gas connection could be moved to the flange at the underside of the CF cross (see Figs. 2.2 - 2.3), and the distance that gas would travel before entering the interaction region is significantly reduced. Such a modification would retain the use of the manipulator for beam alignment while possibly enabling the measurement of cross sections involving traditionally difficult target gases.

To measure relative cross sections, i.e. the fraction of the total cross section for each photon decay pathway, a gas jet may be used. For this purpose, two gas jets are presented to aid future experiments with CUEBIT. The first design operates at relatively low pressures ($\sim$ 1 - 10 mbar) and is intended for loading volatile organic compounds containing metal atoms into CUEBIT. Such a jet would enable CUEBIT to produce beams of multicharged metals, e.g. Mg^{12+} or Fe^{16+}.

The second gas jet design operates at a much higher pressure ($\sim$ 100 - 1000 mbar) and is designed for crossed-beam experiments downstream from the CUEBIT source. A simple model approximates the neutral density at the ion-jet intersection of $n > 10^{10}$ cm^{-3}, and the design of a jet dump has been completed which minimizes gas leakage into the CUEBIT beamline. Using the original leak valve, any commercially available target gas (He, H_2, CO_2, CO, etc.) may be purchased and used to generate a cold neutral target in the interaction chamber.

The most exciting use for this high pressure design is for studying interactions with traditionally difficult target gases. A small, separate chamber housing a hydrogen cracker or water vapour source may be connected to the nozzle gas line to produce cold target beams of H or H_2O. When used for COLTRIMS measurements, these targets need not be of high purity as the events from different targets may be separated out by the coincidence (in time) measurements of the COLTRIMS apparatus. Therefore, only some H or H_2O is needed, and problems related to optimizing the H/H_2 yields or contamination from dissolved gases in the water source are inconsequential.

A new COLTRIMS experiment at CUEBIT is coming on-line. The use of gas jets, similar to those described in Chapter 3, will enable the generation of multicharged metal ion beams relevant to studies of the solar wind. Downstream, the second gas jet will enable relative charge exchange cross section measurements for neutral targets of H, H_2, He, and possibly H_2O. The technique may also be used to study collisions with other molecules of interest such as CO, CO_2, and N_2.

5.2 Experiments in Heavy Element Spectroscopy

Experimental efforts are often motivated by recent discoveries. With the recent detection of the neutron star merger GW170817, laboratory studies of heavy elements have received increased interest. When studying the merger events, interpretation of the observed spectra requires knowledge of the strength of each possible emission line. For heavy elements ($Z > 26$) the available laboratory measurements are low in number. In Chapter 4, new measurements of the emission spectra of Au I and II were discussed. The experimental measurements were carried out at the Compact Toroidal Hybrid (CTH) plasma apparatus at Auburn University. Python codes were developed for analyzing the resulting spectra including an x-ray filter, peak finding, and peak tracking codes. Using the known levels in the literature, a list of possible E1 transitions was derived and checked against the observed spectra. Matches were restricted to within the total uncertainty (0.06 nm), and the behavior of each line is checked against nickel spectra for consistency.

In total, we found 86 emission lines (90 possible transitions) in Au I and

76 lines (81 possible transitions) in Au II. From the observed spectra, the general level structures reported in the literature were confirmed. In particular for Au I, 18 $6s6p$ terms and all but two of the $6s6d$ terms proposed by Platt & Sawyer [110] and Ehrhardt & Davis [107] were found. In Au II, 51 of the transitions are newly observed, and over half of these lines are in the visible ($\lambda > 300$ nm). For both Au I and II, we conditions at the probe tip, $n_e \sim 10^{12}$ cm^{-3} and $T_e \sim 10$ eV, produce similar intensities for both one- and two-electron transitions. Two-electron transitions are typically forbidden, but the low purity of the levels leads to deviations from LS selection rules. The line classifications are corroborated by a least-squares level energy optimization, and the resulting energies and their uncertainties are consistent with the resolution of our spectrometer.

The line and level lists of Au I and II are being shared with collaborators at Auburn University and University of Georgia. The calculations are expected to yield A values that may be incorporated into calculations of other properties (e.g. photoionization cross sections or opacities) necessary for studying neutron star merger ejecta. In an effort to aid their calculations, we reported relative intensities for all observed Au I and Au II lines. Using the peaks within the spectral overlap of neighboring discharges, emission lines of Au I and Au II were placed on the same relative intensity scale. Intensities were reported for a single time in the discharge where the plasma conditions, across all gold probe discharges, were most similar.

The unique plasma conditions within the CTH allow for significant excitation of the levels of interest. Use of both gold- and nickel-plated probes allows for isolating emission lines unique to the surface plating of the probes. For future experiments with other heavy elements, plated targets may again be used. However, the significant contamination of Fe I and II lines would warrant new measurements with a pure iron probe. Alternatively, using a target of pure metal would significantly reduce the strength and number of iron lines in the spectra.

For the other elements of interest, platinum (Pt), iridium (Ir), rhenium (Re), and osmium (Os), solid targets may be a necessity as the plate-ability of these elements is unknown and, in the case of osmium, potentially hazardous to attempt. Targets of pure metal, e.g. solid disks, are commercially available for Pt, Ir, and

146
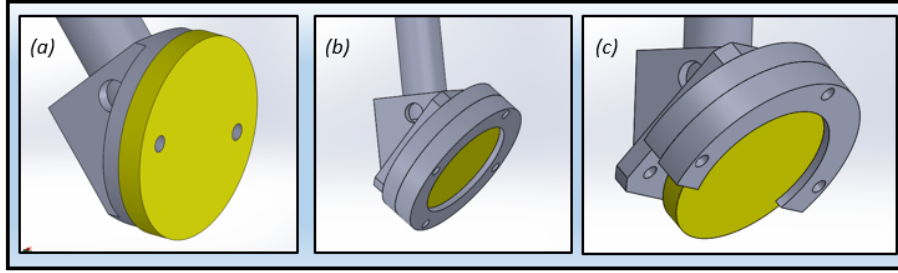
Figure 5.1 Three iterations of a solid target mount design for CTH experiments.

Re. Several iterations of a design to mount such a disk inside the CTH, shown in Fig. 5.2.1, are under consideration. In all three cases, the target is held at a 45° angle w.r.t. the support rod by a triangular mounting plate which maximizes both the plasma exposure and the collected photons. In case (a), the disk is directly attached to the mounting plate via two tapped holes in the target. However, the machinability of (or difficulty in machining) Ir and Re limit this design to Pt targets. In case (b), the disk is held between a backing plate, attached to the triangular mounting plate, and an annular recess in the plasma-facing plate. Such a design is expected to exhibit similar Fe contamination as the plated designs utilized in this work. Design (c) limits the effect of plasma-facing iron components by simply removing the lower $\sim$30% of the steel in the two circular plates. Consideration of a solid holder design is under discussion with our collaborators.

In future experiments, spectra from the neutral and ion of these elements is achievable from plated or solid targets inside the CTH. For higher charge states, e.g. Au IV or Au V, a different source, such as CUEBIT, must be used. It is hoped that these measurements will serve as useful benchmarks for atomic structure calculations and, possibly, enable new studies of r-process nucleosynthesis in both NSM ejecta and the atmospheres of chemically peculiar stars.

Appendices

Appendix A   Gas Jet Code

The gas jet model by Schmidt *et al.* [101] has been coded in Python for easy calculation of gas jet conditions. The code is broken into two pieces: input (geometry, pressure, temperature), and output.

Listing 1 : 'Jet Model.py'

```
"""
SJB
Gas Jet Code
"""
import numpy as np
import math
from scipy import integrate
import scipy
import matplotlib.pyplot as plt

def find_nearest(array, value):
    idx = (np.abs(array - value)).argmin()
    return idx


#%%
##########################
######## Inputs ########
##########################
#Nozzle geometry:
r_noz = .007 * .0254 # (radius (in) * conversion to meter)
A_nozz = np.pi * (r_noz)**2
#Nozzle-skimmer separation
sep = .25 * .0254 # inches (0.25) converted to meters
z_skim = sep
#Skimmer radius
delta_r = .012 * 0.0254 #in to meter
k_b = 1.38064852e-23 #m^2 kg s^-2 K^-1
M = 6.6464764e-27#[kg] for H
#Temperature of gas reservoir:
T_o = 300# [K]
#Temp. at throat of nozzle
T_T = 0.75 * T_o
#Estimated background pressure
P_B = 9e-3
#Gas Reservoir Pressure in Pascals:
P_o = 75000
#Gas reservoir density assuming an ideal gas:
n_o = P_o / (k_b * T_o)
#current design:
#Mach Disk location:
```

```
mach = 2 * r_noz * 0.67 * math.sqrt(P_o / P_B)


#########################
######## Output ########
#########################
#Number leaving the nozzle per second:
N_nozz = (3*P_o*A_nozz / 16) * math.sqrt(15/(k_b*T_o*M))
#Jet Velocity
v_jet = math.sqrt(5*k_b * T_o / M)
#%Maximum allowed transverse temp:
v_perp = (v_jet * (delta_r)/ z_skim)s
T_max = M * (v_perp * v_perp) /(k_b*T_o)
#Velocity distribution at Nozzle exit
v_func = lambda x: 4*np.pi * x**2 * (M/(2*np.pi*k_b*T_T))**(3/2) * math.e**(-M*x**2 / (2*k_b*T_T))
#Calculate Number that pass through nozzle
chi = scipy.integrate.quad(v_func,0,v_perp)[0]
alpha = np.arctan(1/math.sqrt(chi))
#on-axis density as a function of distance:
z = np.linspace(0.0001,1,1000)
#Number exiting skimmer per sec
N_skim = delta_r * delta_r * chi * N_nozz/ (sep * sep)
A_z = np.pi * z**2 * (1/chi)
nz = (n_o * 3 * math.sqrt(3)/16 * A_nozz * chi/ (np.pi * (z*z)))
z_skim = .57*.0254 #converted to meters
nz_int_skim = (n_o * 3 * math.sqrt(3)/16 * A_nozz * chi/ (np.pi * (z_skim*z_skim)))
#Downstream (~7" away) density:
z_interaction = 7 * 0.0254 # [m]
nz_interaction = (n_o * 3 * math.sqrt(3)/16 * A_nozz * chi/ \
(np.pi * (z_interaction*z_interaction))) #[cubic m.]

print('Interaction Density: {:e}'.format(nz_interaction * 1e-6)) #[per cubmic cm]
print('Number leaving the Nozzle per second: {:e}'.format(N_nozz))
print('Percent passing through skimmer: {:}'.format(100*chi))
print('Half-Angle Divergence: {:}'.format(round(alpha,3)))
print('Number leaving skimmer per second: {:e}'.format(N_skim))
print('Transverse Jet Temp.: {:} K'.format(T_max))
print('Skimmer Exit Density: {:e}'.format(nz_int_skim * 1e-6))
```

Appendix B   Low Pressure Jet Design Drawings

The low-pressure jet in Sec. 3.2 is housed inside of standard 2-3/4" CF vacuum components. However, several components were machined separately from the commercially available components. SOLIDWORKS drawings of these unique components are provided below. All units are displayed in inches.
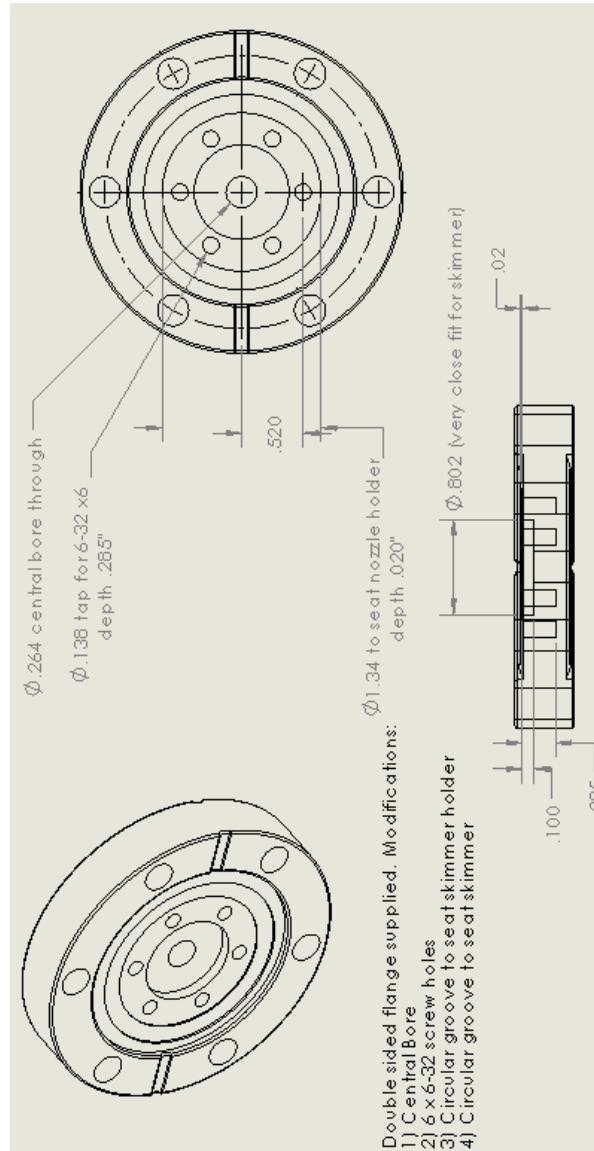
Figure B1 Machine drawing of the double-sided flange holding the skimmer (black) in Fig. 3.4.
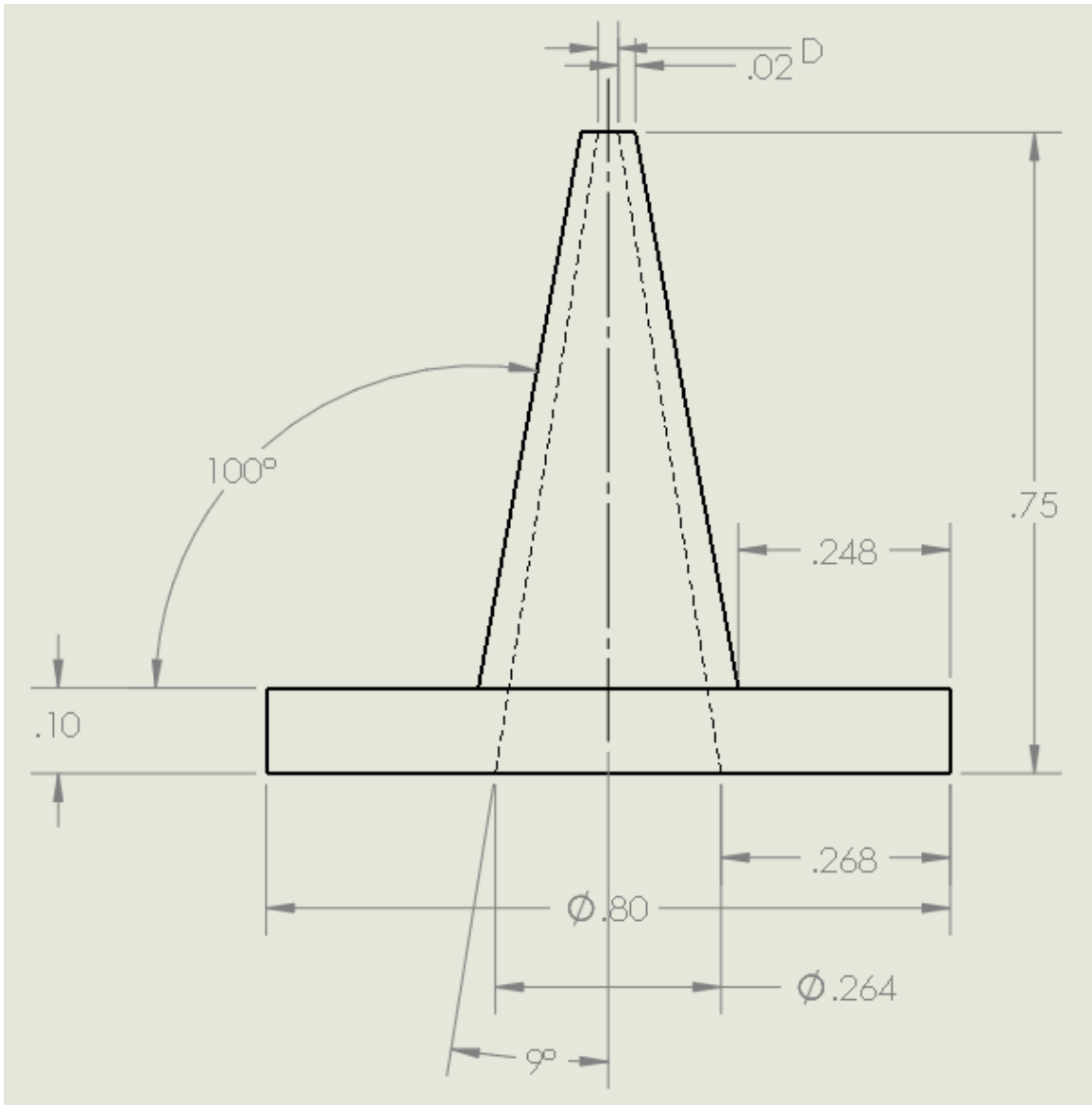
Figure B2 Machine drawing of the nozzle ($D = 0.014''$) and skimmer ($D = 0.023''$).
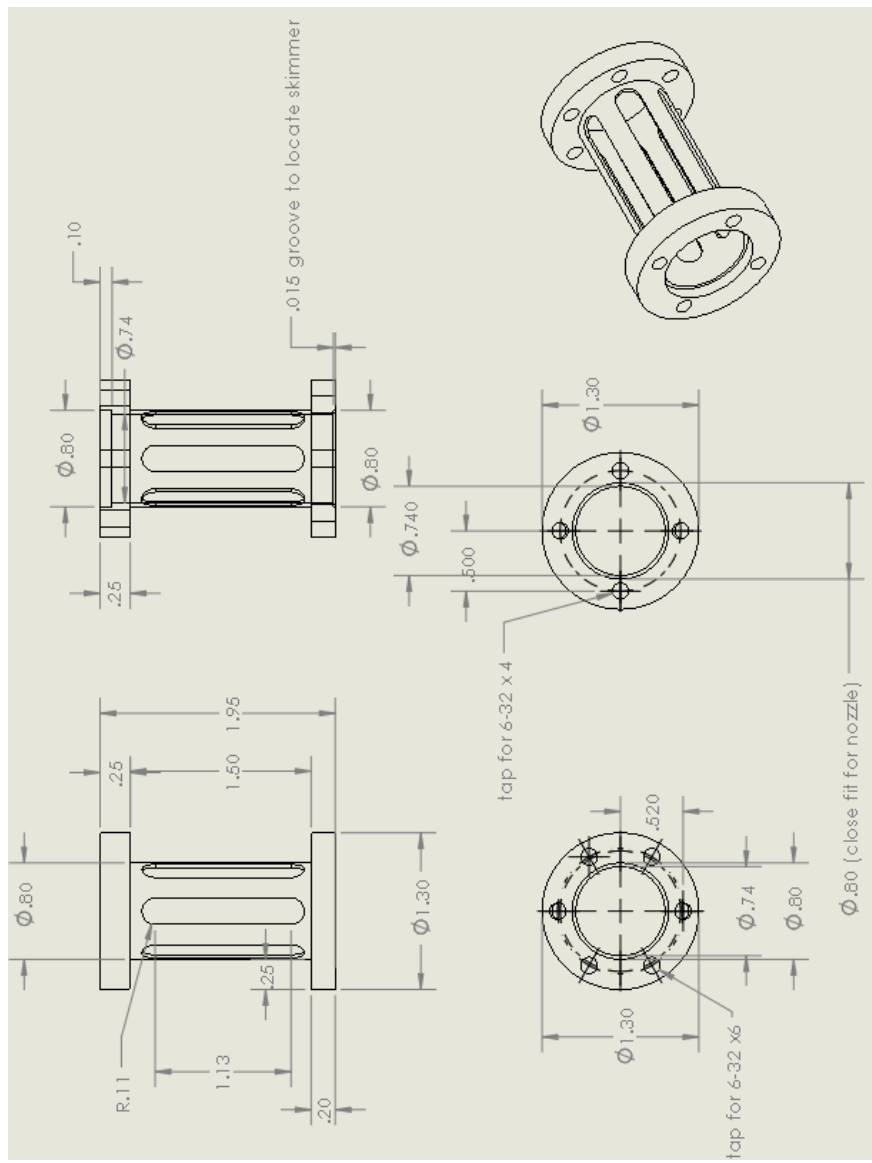
Figure B3 Machine drawing of the nozzle and skimmer holder in Fig. 3.4.
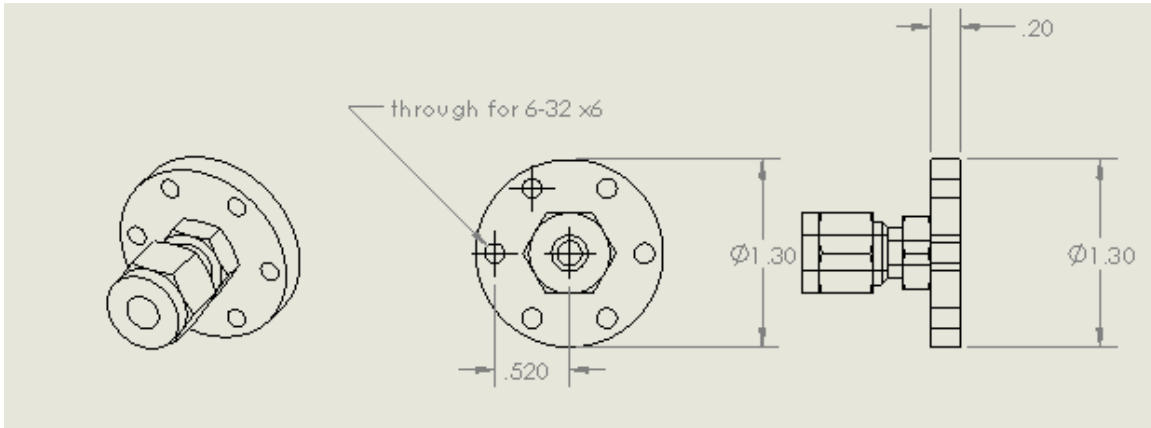
Figure B4 Machine drawing of the two plates holding 1/4" Swagelok connectors on either side of the gas tubing in Fig. 3.4.
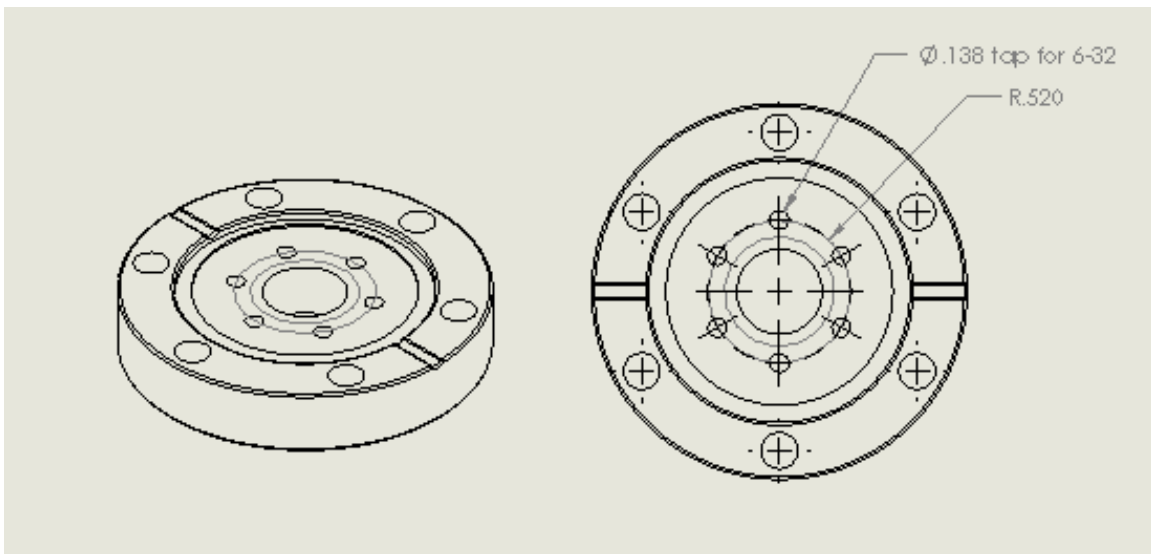
Figure B5 Machine drawing of the 2-3/4"-to-1.33" CF flange with custom bolt pattern on the far left side of Fig. 3.4.

Appendix C   High Pressure Jet Design Drawings

The high pressure jet design utilizes the same nozzle and skimmer as the low pressure jet design. However, several unique components were constructed for the high pressure design. Below, the machine drawings for the gas jet extension and mounting flange are displayed. All dimensions are shown are in inches.
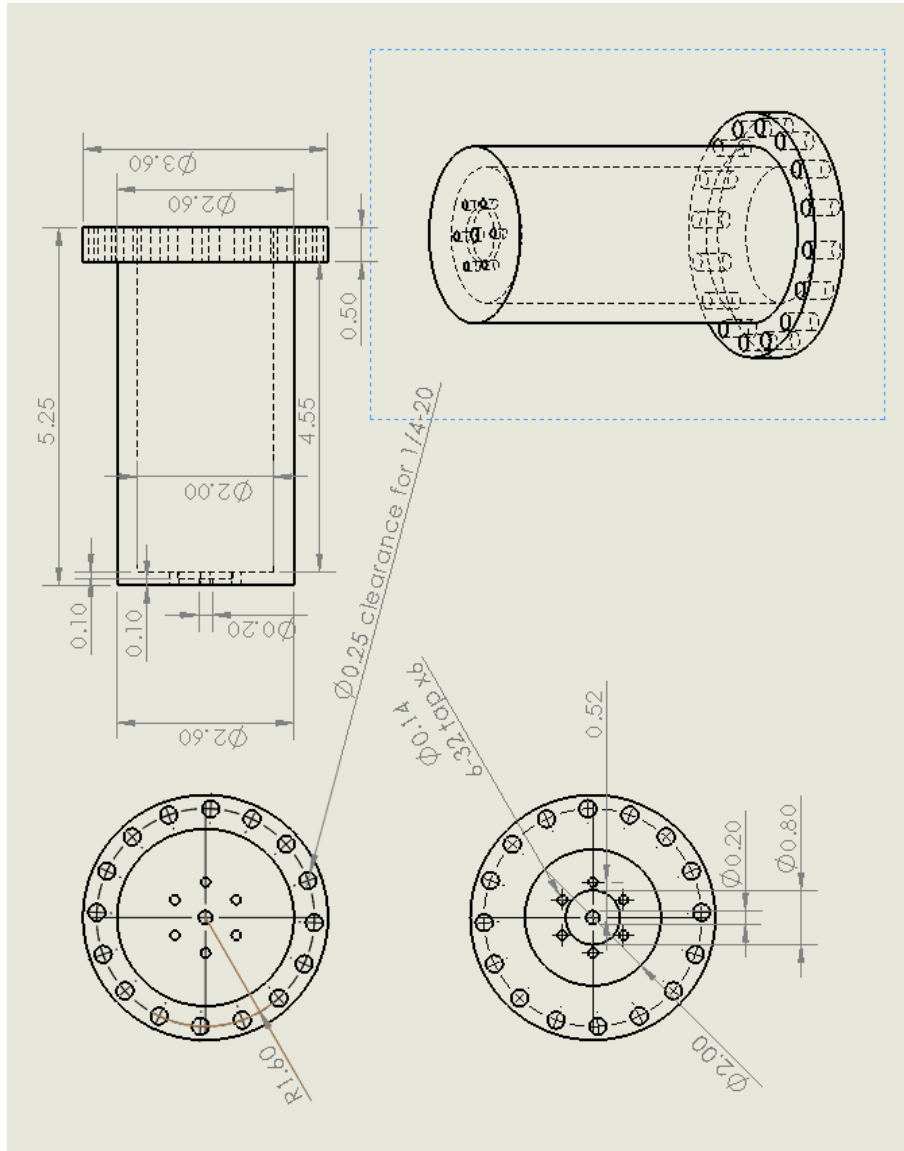
Figure C1 Machine drawing of the extended housing for the nozzle/skimmer in Fig. 3.7.
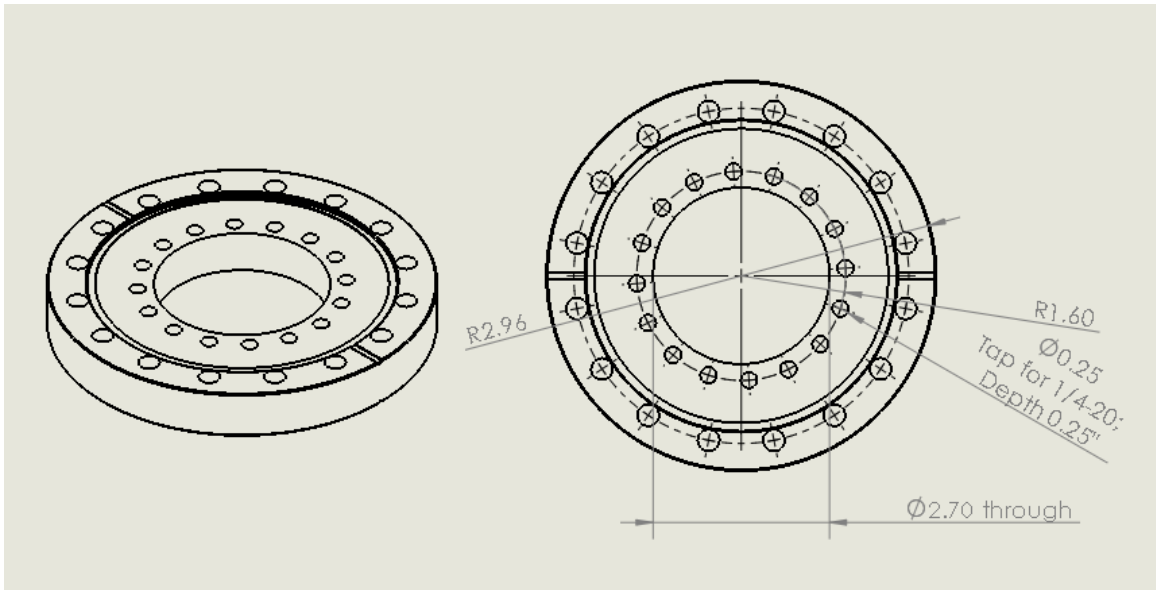
Figure C2 Machine drawing of the double-sided 6" CF flange holding the skimmer (black) in Fig. 3.7.

Appendix D Gold Data Analysis Codes

This Appendix contains various scripts used for the data analysis in Chapter 4. In many cases, these codes have been centralized in the library "steve_lib.py" are accessible in the GitHub repository by clicking here.. However, simplified versions have been provided here. These scripts include a simple x-ray filter, a peak-finding script using the PeakUtils package, a "position scatter plot" code, and sample input files for running the code "LOPT" [125].

D.1 X-Ray Filter

The following script "x-ray_filter.py" is available in the Github repository linked above. The script searches the directory "data_path" for all .csv files (if using glob.glob("*.csv")) or a list of user-defined file names in the variable "manual_input" and performs the x-ray filtering on all files within that directory. Note that this script uses the "read_prin" function (see script) to read in the raw data files. These files contain wavelength versus counts in two column format, and the successive frames of data are stacked vertically. To use this script on files with the format Row 1 (Wavelengths), Rows 2 - ... (Counts), simply replace the function in the definition of variable "pin" from "read_prin" to "np.genfromtxt."

The resulting output files are saved such that the first row is the list of increasing wavelengths, and the subsequent rows are the count values at those wavelengths.

Listing 2 : 'x-ray_filter.py'

```
"""
Steve  Bromley
10-30-19
X-Ray  filter  for  CCD  Data
"""
import os
import numpy as np
import csv
import glob
from numpy import genfromtxt
#Function  for  reading  standard  .csv  form  of  .spe  data
#I.e.  stacked  frames  in  2  column  format  with
```

```python
#Col 1 (Wavelength \ pixel) | Col 2 (Counts)
def read_prin(fil):
    f = open(fil)
    data = np.loadtxt(f,delimiter=',')
    inten = np.reshape(data[:,1],(-1,1340))
    return np.vstack([data[0:1340,0],inten])
##############################################

#Max/min lambda for binning later; bounds will be adjusted depending on input
global_max_lambda = 0
global_min_lambda = 1000
#Threshold for an x-ray being real, i.e. an x-ray contaminated pixel
#has a ratio exceeding the threshold when compared to neighboring pixels
xray_thresh = 2.0
#Save main working directory:
cwd = os.getcwd()
#Number of bins for later:
data_path = 'C:/Users/steve_000/raw_data'
os.chdir(data_path)
manual_input = glob.glob("*.csv")
#Loop over ALL data files of interest in "manual_input" variable:
for data_in in manual_input: #glob.glob('*.csv'):
    os.chdir(data_path)
    pin = read_prin(data_in)
    #Total Number of Frames in data file:
    frames = len(pin[:,0])
    #Final peak output array from gaussian fits
    #Select range of frames for analysis:
    frame1 = 65
    frame2 = 110
    for frame in range(2,len(pin[:,0])-2):#range(frame1,frame2):
        ######################################
        ########      BEGIN      ########
        ########   X-RAY FILTER   ########
        ########  ON EACH FRAME   ########
        ######################################
        for k in range(0,3):
            for i in range(2,len(pin[0,:]) - 3):
#Check for each type of x-ray, i.e. 1 pixel, 2 pixel, 3 pixel
                inp = pin[frame,i]
                #2 pixel x-ray, or two side by side (common in later frames):
                if(((inp / pin[frame,i-1])>xray_thresh) and \
                    ((pin[frame,i+1]/pin[frame,i+2])>xray_thresh)):
                    pin[frame,i] = (pin[frame,i-1] + pin[frame,i+2]) / 2
                    pin[frame,i+1] = (pin[frame,i-1] + pin[frame,i+2]) / 2
                #3 pixel x-ray or 3 side by side (common toward end of shot):
                if ((inp/pin[frame,i-1] > xray_thresh) and \
                    (pin[frame,i+1]/pin[frame,i-1] > xray_thresh) and \
                    (pin[frame,i+2]/pin[frame,i+3] > xray_thresh)) :
                    pin[frame,i] = (pin[frame,i-1] + pin[frame,i+3]) / 2
                    pin[frame,i+1] = (pin[frame,i-1] + pin[frame,i+3]) / 2
                    pin[frame,i+2] = (pin[frame,i-1] + pin[frame,i+3]) / 2
```

159

```python
#1 pixel x-ray:
#Check to see if x-ray is transient, i.e. an x-ray and not a peak:
if ((inp > pin[frame-1,i]) or (inp > pin[frame+1,i])):
    #Remove x-ray by comparing to pixels on either side:
    if (pin[frame,i]/pin[frame,i+1] > xray_thresh):
        pin[frame,i] = (pin[frame,i+1] + pin[frame,i-1]) / 2
    if (pin[frame,i]/pin[frame,i-1] > xray_thresh):
        pin[frame,i] = (pin[frame,i+1] + pin[frame,i-1]) / 2
    if (((inp/pin[frame-1,i]) > xray_thresh) and \
        ((inp/pin[frame+1,i]) > xray_thresh)):
        pin[frame,i] = (pin[frame-1,i] + pin[frame+1,i]) / 2
    #check small, transient in time x-rays:
    #Check based on change in amplitude in time:
    if ((inp/pin[frame-1,i] > 1.4) and (inp/pin[frame+1,i] > 1.4)):
        pin[frame,i] = (pin[frame-1,i] + pin[frame+1,i]) / 2
    #We can compare to pixels on either side for smaller x-rays
    if ((inp/pin[frame,i-1] > 1.4) and (inp/pin[frame,i+1] > 1.4)):
        pin[frame,i] = (pin[frame,i-1] + pin[frame,i+1]) / 2
#Save as the same file name in the working directory:
os.chdir(cwd)
shot_num = re.findall("(\d+)",data_in)
shot_num_int = int(shot_num[0])
np.savetxt('{:}.csv'.format(shot_num_int), pin,delimiter =',')
```

D.2   Peak Finding

The peak lists in this work were generated with the PeakUtils package. To install PeakUtils for the Spyder Python IDE, execute the following code:

```
conda install override -channels -c conda-forge/label/cf201901 peakutils
```

The PeakUtils package has several functions used for peak finding. First, the "background" counts are estimated by a polynomial fit of variable degree. Peaks far from the estimated background counts are assigned a low weighting during the background fit. Second, the peak locations are approximated by searching for local maxima in the raw data. Lastly, the peak locations are refined via a gaussian fit around each peak. The following script executes the peak finding for a list of input files. The peak lists from all input files are combined and binned. The final output is in a four-column format with the following order: Wavelength — Summed Counts —# Detections — Standard Deviation.

These scripts are intended to run with files with numbered names,

160

e.g "18113010.csv." Therefore, if running these scripts for different file names, several lines must be edited. In particular, the variables "shot_num" and "data_files" must be edited to properly reflect the name structure of the input file list.

Listing 3 : 'peak_find.py'

```
"""
Steve Bromley
10-30-19
Peak finding code for CCD data
"""
import os
import numpy as np
import scipy
from scipy import stats
import peakutils
import time
import csv
import glob
import re
from numpy import genfromtxt


def stdev(y):
    return(np.std(y))


def quad_std(x):
    sum = 0
    for i in range(0,len(x)):
        sum = sum + (x[i])**2
    mean = np.sqrt(sum)
    return(mean)
#Max/min lambda for binning later; bounds will be adjusted depending on input
global_max_lambda = 0
global_min_lambda = 1000
#Save main working directory:
cwd = os.getcwd()
data_path = 'C:/Users/steve_000/Desktop/filtered_data'
os.chdir(data_path)
manual_input = glob.glob("*.csv")
#Loop over ALL data files of interest in "manual_input" variable:
for data_in in manual_input:
    os.chdir(data_path)
    pin = genfromtxt(data_in,delimiter = ',')
    #Total Number of Frames in data file:
    frames = len(pin[:,0])
    #Final peak output array from gaussian fits
    all_peaks_out = np.empty((1340,200,2))
```

```
frame1 = 65
frame2 = 110
for frame in range(frame1,frame2):#range(frame1,frame2):
    baseline = peakutils.baseline(pin[frame,:], deg=3, max_it=100, tol=1e-5)
    indexes = peakutils.peak.indexes(pin[frame,:], thres=baseline + 100,\
                                    min_dist=2, thres_abs='true')
    interp_peaks = peakutils.peak.interpolate(pin[0,:],pin[frame,:],indexes,width = 1)


#Save output in 2 column format:
#Peak Wavelength    Peak Counts
    numPeaks = len(indexes[:])
    all_peaks_out[0,frame,0] = frame
#Get local max/min lambda from data and adjust globals:
    min_lambda = pin[0,0]
    max_lambda = pin[0,1339]
    if min_lambda < global_min_lambda:
        global_min_lambda = min_lambda
    if max_lambda > global_max_lambda:
        global_max_lambda = max_lambda
    for i in range(0,numPeaks):
        all_peaks_out[i+1,frame,0] = interp_peaks[i]
        all_peaks_out[i+1,frame,1] = pin[frame,indexes[i]] - baseline[i]
        if (interp_peaks[i] > max_lambda or interp_peaks[i] < min_lambda):
                all_peaks_out[i+1,frame,0] = 0
#For each row in output, save wavelength and counts in 2 column format
output = all_peaks_out[0:numPeaks,frame1:frame2,:]
output = np.transpose(output)
#Array for storing 2d data used in next loop:
output_2d = np.zeros((0,2))
for j in range(0,len(output[0,:,0])):
#For a given row (j), add in all values from 0 -> end of frames data
    output_temp = np.zeros((len(output[0,0,1:]),2))
    for k in range(0,len(output[0,0,1:])):
        output_temp[k,0] = output[0,j,k+1]
        output_temp[k,1] = output[1,j,k+1]
    output_2d = np.append(output_2d,output_temp, axis=0)
#Sort:
output_2d= output_2d[np.argsort(output_2d[:,0])]
#Remove nan:
output_2d = output_2d[output_2d.all(1)]
#38.2 nm / 764 bins = .05nm bins; I used to use 390
num_Bins = 764
#Mean peak positions:
peaks_binned = scipy.stats.binned_statistic(output_2d[:,0],output_2d[:,0], statistic='mean', \
                                    bins = num_Bins, range=(min_lambda,max_lambda))
#Number of counts (intensity) in each bin
counts_binned = scipy.stats.binned_statistic(output_2d[:,0],output_2d[:,1], statistic='sum', \
                                    bins = num_Bins , range=(min_lambda,max_lambda))
#Number of peaks used to calculate the positions and counts in each bin
pks_per_bin = scipy.stats.binned_statistic(output_2d[:,0],output_2d[:,1], statistic='count', \
                                    bins = num_Bins , range=(min_lambda,max_lambda))
```

```python
#Calculate FINAL stdev (add stdev in quadrature):
peaks_stdev = scipy.stats.binned_statistic(output_2d[:,0],output_2d[:,0], statistic=stdev,\
                                             bins = num_Bins, range= (min_lambda,max_lambda))
os.chdir(cwd)
##Export the avg peak and count to csv file
a = peaks_binned[0][:]
b = counts_binned[0][:]
c = pks_per_bin[0][:]
d = peaks_stdev[0][:]
#Get shot # to save to output
shot_num = re.findall("(\d+)",data_in)
shot_num_int = int(shot_num[0])
#Ex: output will be 18113026_500_540.csv -> 500- 540nm, shot num ...
with open('{:3}_{:3}_{:3}.csv'.format(shot_num_int,min_lambda,max_lambda), 'w') as f:
    writer = csv.writer(f, delimiter='\t')
    writer.writerows(zip(a,b,c,d))
f.close()


###Import all output CSV files and store in 2-D, sorted array
all_peak_data = np.empty((0,4))
#Grab all of the .csv's
data_files = glob.glob('1811*')
#Remove NaN entries from binning carried out previously and then sort
for data_file in data_files:
    data_in = genfromtxt(data_file, delimiter = '\t')
    data_in = data_in[~np.isnan(data_in).any(axis=1)]
    all_peak_data = np.append(all_peak_data,data_in, axis=0)
all_peak_data_sorted = all_peak_data[np.argsort(all_peak_data[:,0])]


###Rebinning the peaked data for all files
bin_size = .05
num_Bins = round((global_max_lambda - global_min_lambda)/bin_size)
testing2 = scipy.stats.binned_statistic(all_peak_data_sorted[:,0],all_peak_data_sorted[:,0],\
                                         statistic='mean', bins = num_Bins, range= \
                                         (global_min_lambda,global_max_lambda))
testing_count2 = scipy.stats.binned_statistic(all_peak_data_sorted[:,0],\
        all_peak_data_sorted[:,1], statistic='sum',\
        bins = num_Bins, range = (global_min_lambda, global_max_lambda))
testing2_pks_per_bin = scipy.stats.binned_statistic(all_peak_data_sorted[:,0],\
        all_peak_data_sorted[:,2], statistic='sum', bins = num_Bins , \
        range=(global_min_lambda,global_max_lambda))
testing_stdev = scipy.stats.binned_statistic(all_peak_data_sorted[:,0],\
        all_peak_data_sorted[:,3], statistic=quad_std, bins = num_Bins,\
        range= (global_min_lambda,global_max_lambda))
#%%
a1 = np.asarray(testing2[0][:])
b1 = np.asarray(testing_count2[0][:])
c1 = np.asarray(testing2_pks_per_bin[0][:])
d1 = np.asarray(testing_stdev[0][:])
abc1 = np.vstack((a1,b1,c1,d1))
#%%
final_lines_out = np.transpose(abc1)
```

```
final_lines_out = final_lines_out[~np.isnan(final_lines_out).any(axis=1)]
#
std_min = 0
final = np.empty((0,4))
final = np.vstack((final,final_lines_out[final_lines_out[:,3] > std_min]))
#Output FINAL line positions
np.savetxt('final_output.txt',final,fmt='%.7f',delimiter=',')
#%%
#Remove the temporary .csv's made from peak-finding of each input file
files_to_delete = glob.glob("1811*")
for f in files_to_delete:
    os.remove(f)
```

D.3   Peak Intensities

After finding the peaks within each frame, it may be useful to pick out intensities within a given frame. Rather than simply reporting the peak height, the total counts within a given peak are spread over some profile. For the spectrometer resolution in this work, $\approx$0.04 nm, the line profiles are decidedly gaussian. The script "peak_intensity.py" returns peak intensities by carrying out the following. This script relies on functions found in "steve_lib.py," but for the sake of this script were copied into a separate file. First, the background is fit to an n-degree polynomial (user specified n). A gaussian is fit to each peak in the input line list, and the spatial extent (i.e. in wavelength) is found by calculating the intersections of the background polynomial and gaussian. Second, the difference between the gaussian and the polynomial of the background is integrated between the two intersection points.

The functions take several inputs. The variable "regions" contains an array of information about the 17 wavelength ranges between 187 - 800 nm. The array of information is stored in a file with the format: Numerical Label — Lower Wavelength — Upper Wavelength — Frame — Poynomial Degree. If the user wants to use a frame separate from that listed in this input file, change the variable "frame_source" in the function call from "file" to "frame", and the function will use the value in the variable "frame_in" in the function call. The file used for the Au I analysis is shown below.

164

Listing 4 : 'regions.txt'

0	187.3811523	230.5	88	10
1	230.5	266.3261812	82	10
2	266.3261812	302.1682958	71	10
3	302.1682958	337.999377	79	10
4	337.999377	373.8192882	82	10
5	373.8192882	409.6278729	88	3
6	409.6278729	445.4249536	90	3
7	445.4249536	481.2103301	87	3
8	481.2103301	516.983778	86	3
9	516.983778	552.7450461	86	3
10	552.7450461	588.4938546	80	3
11	588.4938546	624.2298921	80	3
12	624.2298921	659.9528121	86	3
13	659.9528121	695.6622297	83	6
14	695.6622297	731.3577164	83	3
15	731.3577164	767.0387956	83	3
16	767.0387956	802.7049356	86	6

The "method" refers to the normalization of the lines. If using "absolute," the lines are normalized to the height, relative to the strongest line within the whole wavelength range. The strongest line is set to the intensity in the variable "scale_max." Alternatively, the method "relative" normalizes to the peak heights to the strongest line (again, set to "scale_max") *within each wavelength range.*

Listing 5 : 'peak_intensity.py'

```
"""
SJB
Peak Intensity Code
"""
import os
import numpy as np
import scipy
from scipy import stats
from scipy.optimize import curve_fit
from numpy import inf
import peakutils
import csv
import glob
import re
from numpy import genfromtxt
from scipy.integrate import *
from math import erf
from math import *
#############################################
```

```
#Peak Finding Function
def peak_find(frame1,frame2,array):
    array2 = np.zeros((121,1340,2))
    for frame in range(frame1,frame2):#range(frame1,frame2):
        min_lambda = array[0,0]
        max_lambda = array[0,1339]
        #Estimate background counts
        baseline = peakutils.baseline(array[frame,:], deg=3, max_it=100, tol=1e-5)
        #Approximate peak positions
        indexes = peakutils.peak.indexes(array[frame,:], thres=baseline + 100,\
                                           min_dist=2, thres_abs=True)
        #Refine peak positions
        interp_peaks = peakutils.peak.interpolate(array[0,:],array[frame,:],indexes,width = 1)
        numPeaks = len(interp_peaks[:])
        array2[0,frame,0] = frame
        k=0
        for j in range(0,numPeaks):
            if (min_lambda < interp_peaks[j] < max_lambda):
                array2[frame,k,0] = interp_peaks[j]
                array2[frame,k,1] = array[frame,indexes[j]]
                k = k +1
    return(array,array2)


def intensity_search_v3(array,frame_in,normalize,scale_max,method,regions, \
                        data_directory,frame_source,calib,correct):
    ##################################################################################
    #####################  Explanation of the parameters   ##########################
    #
    #   array: input array of line positions
    #   frame: frame you want the intensities from
    #   normalize: boolean; if 'True', normalize the largest value to scale_max
    #   scale_max: absolute maximum by which the found line intensities are normalized
    #   method: select either 'relative' or 'absolute'
    #          'relative': normalizes to scale_max within each wavelength region
    #          'absolute': normalizes to scale_max over all wavelength ranges (not reliable)
    #   regions: array containing the wavelength regions from the raw data. Ex:
    #              Format: (region #) (lower lambda) (upper lambda) (frame for intensities)
    #              (deg. for baseline polynomial)
    #   frame_source: 'user' uses the value of 'frame' in the function call, or 'file'
    #    uses the col #4 from regions array
    #   calib: intensity response of detector on 0 - 100 scale; 2 col format:
    #   Wavelength (nm) | Response. (defined 0 as first element)          #
    #   correct: boolean controlling whether or not to re-calibration with the above calib file
    ##################################################################################
    cwd = os.getcwd()
    #define the data directory (probe2), output dir. for plots (frame plots), and
    #shot_list (wav. regions)
    shot_list = genfromtxt('shots.csv',delimiter = ',')
    lines = array
    os.chdir(cwd)
    temp = np.empty((1))
    #initial output of intensity search is  intensity is intens_arr
```

```python
intens_arr = np.empty((0,4))
for countr in range(0,17):
    #load the data for the shot in wavelength range defined by countr:
    os.chdir(data_directory)
    probe2_6cm = str(int(shot_list[countr,4])) + '.csv'
    probe2_6cm_dat = genfromtxt(probe2_6cm,delimiter=',')
    probe2_6cm_shot = str(int(shot_list[countr,4]))
    probe2_6cm_num = int(probe2_6cm_shot)
    data_in = probe2_6cm_dat
    x_min = data_in[0,0]
    x_max = data_in[0,1339]
    lines_in_region = np.empty((0))
    #temp arr for holding lines
    temp1 = np.empty((1))
    #grab the lines within this wavelength window
    for i in range(0,len(lines)):
        if (x_min < lines[i] < x_max):
            temp1 = lines[i]
            lines_in_region = np.append(lines_in_region,temp1)
    lines_in_region = lines_in_region[lines_in_region[:].argsort()]
    #%Find the peaks using my standard peak finding function:
    #frame1 = 60
    #frame2 = 120
    #peak list from peak finding code. Do for all frames from frame1 -frame2
    if (frame_source == 'user'):
        deg = int(6)
        frame = int(frame_in)
    if (frame_source =='file'):
        deg = int(regions[countr,4])
        frame = int(regions[countr,3])
    peak_ls = peak_find(frame,frame+1,data_in)
    #loop over all frames :)
    #Find the baseline values & initialize values for the total gaussian and
    #the spectra function
    total_gauss = 0
    #modified the peakutils baseline function to return the coefficients too :)
    baseline_tot = baseline_mod(data_in[frame,:], deg, max_it=100, tol=1e-5)
    baseline = baseline_tot[0]
    #define an array of coefficients for poly1d function:
    #fit our x values to a 'deg' degree polynomial for the baseline y values; return coeffs
    poly_params = np.polyfit(data_in[0,:], baseline, deg)
    #define a polynomial with the resulting coeffs. Use the function 'poly' below
    #for integrating
    poly = np.poly1d(poly_params)
    poly_dat = poly(data_in[0,:])
    #the baseline acts as the starting point for constructing the 'synthetic spectra'
    synthetic_spec = baseline
    for i in range(0,len(lines_in_region)):
        #open up an output file for troubleshooting if need be:
        #file = open('testfile_frame_{:}.txt'.format(lines_in_region), 'w')
        #tempa array to hold each peaks data before saving:
        temp = np.empty((1,4))
```

```python
#only look for the peak & fit IF the peak is in this wavelength region:
location = find_nearest_index(data_in[0,:], lines_in_region[i])
for j in range(0,len(data_in[0,:])):
    #check to make sure the peak finding found the peak in this frame:
    if (abs(lines_in_region[i] - peak_ls[1][frame,j,0]) < .04):
        #make sure the peak isn't at the borders:
        if (5 < location < 1334):
            #try to fit; otherwise throw an error and go to next peak:
            try:
                #Set the initial parameters for height, center, and width
                #location = 1057
                A_0 = data_in[frame,location]
                #mu_0 = data_in[0,location]
                mu_0 = peak_ls[1][frame,j,0]
                sigma_0 = 0.1
                p0 = [A_0,mu_0,sigma_0] #C_0]
                #changed from .03 to .04 on 10-02-19
                c1 = .04#c1 control the constraint on the line center
                #limit the peak height unless the peak is saturated
                if (data_in[frame,location] == 65535):
                    count_wiggle = 200000
                else:
                    count_wiggle = 100
                bounds_init = ((data_in[frame,location] - 100 , \
                                peak_ls[1][frame,j,0] - c1,0), \
                                (data_in[frame,location] + count_wiggle , \
                                peak_ls[1][frame,j,0] + c1, 0.14))
                #fit to a gaussian using the curve_fit module:
                coeff, var_matrix = curve_fit(gaussian, data_in[0,:], \
                    data_in[frame,:], p0=p0, \
                    bounds = bounds_init)
                fit = gaussian(data_in[0,:],*coeff)
                #intersections between gaussian and baseline
                intersections = \
                            np.argwhere(np.diff(np.sign(fit - baseline))).flatten()
                #new x limits are the intersections between baseline
                                            #and gaussian functions
                lower_x = data_in[0,intersections[0]]
                upper_x = data_in[0,intersections[1]]
                #background counts for this peak:
                bkg_counts = quad(poly,lower_x,upper_x)
                #numerically integrated intens:
                int_intens = quad(gaussian, lower_x , upper_x, \
                                            args = (coeff[0],coeff[1],coeff[2]))
                #analytically integrated intensity; save both later
                analytic_intens = \
                            analytic_counts(lower_x, upper_x, coeff[0],coeff[1],coeff[2])
                #save wavelength, numerical intens, analytic intens,
                                            #and frame # for each peak
                temp[0,0] = lines_in_region[i]
                temp[0,1] = int_intens[0] - bkg_counts[0]
                if (temp[0,1] < 0):
```

```python
                        temp[0,1] = 0
                    temp[0,2] = analytic_intens - bkg_counts[0]
                    temp[0,3] = frame
                    intens_arr = np.append(intens_arr,temp,axis=0)
                except RuntimeError:
                    print('Error - curve_fit failed for peak at {:}'.format(
                            lines_in_region[i]))
                    print('Peak {:} added to output with intensity 0'.format(
                            lines_in_region[i]))

                    #Add in a 0 intensity entry for the failed peak
                    #Added on 1-7-19
                    temp = np.empty((1,4))
                    temp[0,0] = lines_in_region[i]
                    temp[0,1] = 0
                    temp[0,2] = 0
                    temp[0,3] = frame
                    intens_arr = np.append(intens_arr,temp,axis=0)
                except IndexError:
                    print('Error - No Intersections (peak {:} DNE)'.format(
                            round(lines_in_region[i],5)))
intensity_out = np.empty((0,2))
os.chdir(cwd)
#sort the output and return the integrated intensities
for i in range(0,len(lines[:])):
    temp_intens = np.empty((1,2))
    temp_intens[0,0] = lines[i]
    for j in range(0,len(intens_arr[:,0])):
        if (intens_arr[j,0] == lines[i]):
            temp_intens[0,1] = temp_intens[0,1] + intens_arr[j,1]
    intensity_out = np.append(intensity_out, temp_intens, axis=0)
#Added on 01-06-20 to incorporate spectrometer response calibration
if ('correct' == True):
    for p in range(0,len(intensity_out[:,0])):
        #find the correction factor needed to apply the calibration
        #search in the calib (column 0) for nearest index of the entry which has the same
        #wavelength as the intensity_out array value
        calib_val = calib[find_nearest_index(calib[:,0],intensity_out[p,0]),1]
        intensity_out[p,1] = intensity_out[p,1] * 100 / calib_val
if ((normalize == 'True') and (method == 'absolute')):
    max_val = np.amax(intensity_out[:,1])
    intensity_out[:,1] = scale_max * intensity_out[:,1] / max_val
intensity_out_temp = intensity_out
#Not working
if ((normalize == 'True') and (method == 'relative')):
    for r in range(0,len(regions[:,0])):
        lower_x = regions[r,1]
        upper_x = regions[r,2]
        region_list = np.empty((0,2))
        #find the lines within each wavelength region:
        for i in range(0,len(intensity_out_temp[:,0])):
            temp = np.empty((1,2))
```

```
        if (lower_x < intensity_out_temp[i,0] < upper_x):
            temp[0,0] = intensity_out_temp[i,0]
            temp[0,1] = intensity_out_temp[i,1]
            region_list = np.append(region_list,temp, axis = 0)
    if (r == 10):
        np.savetxt('region_list_test.txt', region_list)
    #find the maximum for lines in this wavelength region
    try:
        max_val = np.amax(region_list[:,1])
        #normalize to the maximum value in this region
        region_list[:,1] = scale_max * region_list[:,1] / max_val
        #replace the intensities in the master list with the normalized values:
        for i in range(0,len(intensity_out_temp[:,0])):
                j_max = len(region_list)
                for j in range(0,len(region_list)):
                    #Added on 10-15-19 to fix issue with blend intensity
                    if (region_list[j,0] == intensity_out_temp[i,0]):
                        if (len(region_list) < 2):
                            intensity_out_temp[i,1] = region_list[j,1]
                        if (region_list[j,0] != region_list[j-1,0]):
                            intensity_out_temp[i,1] = region_list[j,1]
    except ValueError:
        print('No_Peaks_in_wavelength_range_{:}_:_{:}_-_{:}_nm'.format(countr,
                regions[r,1],regions[r,2]))
intensity_out = intensity_out_temp
return intensity_out
```

D.4   LOPT Scripts

This work utilized the "LOPT" code from Ref. [125]. The code is freely available online. While the program is executed in Perl, it may be called from a regular command line or Windows Powershell terminal. The LOPT code takes in a set of observed wavelengths and level labels and performs a least-squares fitting to recover the level energies. The choice of labels is completely arbitrary, and the output gives no information on the level structure, configurations, etc. It is simply a least-squares fitting of the level energies from a set of wavelengths. While the choice of level labels is arbitrary, it is necessary that the labels be correct and consistent. I developed my own system for keeping track of the labels. The known levels in the literature were assembled in a .csv file in order of increasing energy, and the levels are assigned a numerical label. The configuration label, J value, energy, and reference are also

170

stored. The configuration labels are shown with LaTeX formatting characters as this file is used to generate tables of lines and levels from the LOPT output. This step is not neccessary to run LOPT, but it makes it easier to post-process the LOPT output.

A sample of the level file format is shown below for Au I:

Listing 6 : Levels File Format

```
Num.  Config.                                               J        Energy (cm^-1)    Reference
0        5$$d$$$^{10}$6$s$ $^2$S                            1/2      0                       ED
1        5$d$$^{9}$6$s$$^2$ $^2$D                           5/2      9161.3                  ED
2        5$d$$^{9}$6$s$$^2$ $^2$D                           3/2      21435.191               ED
3        5$d$$^{10}$6$p$ $^2$P$^{\circ}$                    1/2      37358.9                 ED
4        5$d$$^{10}$6$p$ $^2$P$^{\circ}$                    3/2      41174.613               ED
5        5$d$$^{9}$6$s$6$p$ $^4$P$^{\circ}$                 5/2      42163.53                ED
6        5$d$$^{9}$6$s$6$p$ $^4$F$^{\circ}$                 7/2      45537.195               ED
7        5$d$$^{9}$6$s$6$p$ $^4$F$^{\circ}$                 5/2      46174.979               ED
8        5$d$$^{9}$6$s$6$p$ $^4$D$^{\circ}$                 5/2      46379                   PS
9        5$d$$^{9}$6$s$6$p$ $^4$P$^{\circ}$                 3/2      47007.433               ED
10       5$d$$^{9}$6$s$6$p$ $^4$F$^{\circ}$                 9/2      48697.147               ED
...
...
```

The LOPT code requires several input files. The first is the ".fix" file. This file contains a list of fixed level energies and uncertainties. When LOPT is ran, the levels listed in the .fix file will be held constant during the level energy optimization, and the associated uncertainties will be propagated to other derived quantities, e.g. other level energies and Ritz wavelengths. The minimal requirement to run is a ground state (defined as 0 energy and 0 uncertainty), and though additional levels may be fixed they must have a non-zero uncertainty. A sample of this file format is shown:

Listing 7 : LOPT - lines.fix file format

```
Label Energy (cm^-1)   Uncert. (cm^-1)
00  0.0              0.0
35  67490            0.005
50  72694.8          0.005
```

Note that we have specified the level label of the ground state as '00' rather

than '0.' This is necessary for LOPT to run properly, and a single '0' will result in useless output files. All single-digit labels must be double digits. This is not stated in the LOPT manual, but this has been observed to be true for numerical level labels. Though non-numeric labels may be used, they have been avoided as it complicates the post-processing of the LOPT output files.

LOPT requires a list of observed transitions. These are stored in the ".lin" file in the format: Wavelength (Angstroms) — Uncertainty (Angstroms) — Lower Level — Upper Level. A sample of this format is shown below. Note that the extra 0s are necessary to maintain the column widths. The LOPT code reads in the .fix and .lin files with fixed column widths, and a lack of the necessary decimals will lead to useless output files.

Listing 8 : LOPT - lines.lin file format

```
1978.180000       0.2600000       01      22
2012.600000       0.2500000       01          21
2035.000000       0.2300000       03          80
...
```

Lastly, LOPT requires a master ".par" file that contains the instructions for running LOPT. Using the above file formats, the following .par file would execute an LOPT calculation for the three transitions listed above with the fixed levels from the .fix file.

Listing 9 : LOPT - lines.par

```
au_I_.lin        ; Transitions input file name
au_I.fix         ; Fixed levels input file name
au_I_levels_out.txt   ; Levels output file name
au_I_lines_out.txt   ; Transitions output file name
N                ; OMIT calc. wavelengths in ANGSTROMS in the output (Y/N)?
Y                ; TUNE single-line levels (Y/N)?
N                ; Print listing of correlated-lines uncert. effects (Y/N)?
Y       ; Calculate predicted line uncertainties (Y/N)?
Y       ; Write virtual lines (Y/N)?
Y       ; Divide levels into independent groups?
1900.0  ; Min. wavenumber for air wavelength
```

```
100000.0 ; Max. wavenumber for air wavelength
25.0     ; Round−off threshold for output levels
25.0     ; Round−off threshold for output lines
   31    ; first column of line intensity in the transitions−input file
   47    ; last column of line intensity in the transitions−input file
1        ; first column of wavelength in the transitions−input file
12       ; last column of wavelength in the transitions−input file
       ; first column of wavelength units in the transitions−input file (width=4 chars)
  14     ; first column of wavelength uncertainty in the transitions−input file
  23     ; last column of wavelength uncertainty in the transitions−input file
  95     ; first column of line weight in the transitions−input file
 103     ; last column of line weight in the transitions−input file
24       ; first column of lower level label in the transitions−input file
28       ; last column of lower level label in the transitions−input file
  30     ; first column of upper level label in the transitions−input file (same width)
104      ; 1st column for LINE FLAGS (See LOPT Manual)
Y        ; tab−delimited output [Y/N]?
```

With the .par, .fix, and .lin files in the same directory as the LOPT source files (see Ref. [125] and the discussion therein), the LOPT code is executed with a single line in the directory of the files:

```
perl Lopt.pl lopt.par
```

The output of LOPT consists of two files: the levels, and the transitions. A sample of the levels file is shown below. The outputs follow the same convention as the level labels in the lines (.lin) file, and the energy (cm^{-1}), uncertainty with respect to the ground term (D2, cm^{-1}) and number of lines involving the level are shown. The uncertainty D3 is the uncertainty w.r.t. the lowest term in the group of levels. In this case, all levels are connected to ground, so D3 is equivalent to D2 and not shown. In the event that a group of levels has no fixed connection to ground, the output reports the energies with respect to the lowest level within the group (which is set to '0') and level energies with respect to this term are denoted by the text '[level label]' in the output. For example, "30 [5]" indicates the energy is 30 cm^{-1} above the energy of level 5. The lines output file is also shown.

Listing 10 : LOPT - levels output

Designation	Energy	D1	D2	D3	N_lines	Comments
G0	0	0.004	0	_	3	fixed by user

1	9161	3	4	_	8	
2	21435.8	1.1	4	_	"6, 1D"	
3	37360.6	1.2	4	_	6	
4	41174.34	2.27	4	_	8	
5	42163.6	2.1	3	_	6	
6	45536	3	3	_	3	
7	46174.5	2.1	4	_	5	
8	46380.4	2.1	4	_	"6, 4D"	
9	47008	4	5	_	"4, 3D"	
10	48694.3	1.8	4	_	1	
11	51026.6	1.3	4	_	3	

D.5   LOPT Processing

While the output files are easily handled in Python, it may also be desirable to convert the lines and levels to a more readable format. Scripts were written to port the .txt outputs of LOPT into compile-ready LaTeX code. The script reads in the previously discussed table of level energies, configurations, J values, and references. The script reads in the LOPT output levels, and generates a compile-ready LaTeX string with the column ordering (for the level table): Label — Energy (experimental; LOPT output) — Energy (literature value) — Difference in Energies — Number of Lines — Ref. (if necessary). The scripts detailed here were used to generate the bodies of the data tables in Chapter 4. However, the user must manually configure the remainder of the table in LaTeX, i.e. the column headings, caption, etc.

The lines script is similar. The script reads in the LOPT output, the level labels file, and a separate file of lines with references (file format: Wavelength — Lower Level — Upper Level — Reference; e.g. 200.4 nm 01 10 ED). The intensity is calculated with the same function discussed earlier, i.e. an integrated intensity with background subtraction. The Ritz wavelength may be toggled between two options: "experimental" and "theoretical." The "theoretical" option calculates the Ritz wavelengths and the difference between the Ritz and observed wavelengths from the *literature* values of the level energies. The "experimental" option calculates these quantities using the optimized energies from LOPT. Lastly, a comment may be placed

Listing 11 : LOPT - lines output

Iobs	W_obs	uncW_o	wn_o	uncWnO	W_c_air	W_c_vac	S	uncW_c	Wn_c	uncWnC	dWO-C	dEO-C	L1	L2	E1	E2	Weight	Unit
1	2012.6	0.6	49671	15	2012.11	2012.76		0.18	49683	5	0.5	−12	1	21	9161	58844.1	1	A
9	2126.8	0.5	47004	11	2126.63	2127.3		0.24	47008	5	0.2	−4	G0	9	0	47008	1	A
5	2170.9	0.5	46050	11	2170.67	2171.35		0.17	46054	4	0.2	−4	2	35	21435.8	67490	1	A
5	2291.1	0.6	43634	11	2290.67	2291.38		0.18	43642	3	0.4	−8	1	15	9161	52802.9	1	A

175

next to the reference in the compiled table. The comments are organized in a .txt file with two column format: Col. 1 (Wavelength), Col. 2 (Comment). The final table takes the form: Relative Intensity — Wavelength (Exp.) — Wavelength (Ritz) — Wavelength Difference — Lower Level Configuration — Lower level J — Upper Level Configuration — Upper Level J — Comment — Reference.

Listing 12 : LOPT Post-Processing: Compiling Levels into LaTeX Tables

```python
# -*- coding: utf-8 -*-
"""
SJB
06-17-19
script for turning data files into latex text
"""
#######################################
import sys
#define path for steve_lib.py
sys.path.insert(0, 'C:/Users/steve_000/Desktop/Research_Files/PRA_gold_spectroscopy')
#IMPORT EVERYTHING
from steve_lib import *
import math
from math import floor
def round_to_1(x):
    return round(x, -int(floor(math.log10(abs(x)))))
#######################################
paper_path = 'C:/Users/steve_000/Desktop/paper_path'
LOPT_folder = 'C:/Users/steve_000/Desktop/AuI_LOPT'
cwd = os.getcwd()
os.chdir(LOPT_folder)
output = ''
levels_dat = glob.glob('au_I_levels*.txt')
data_in = np.genfromtxt(levels_dat[0],delimiter='\t', dtype = str, skip_header = 1)
os.chdir(cwd)
level_labels = np.genfromtxt('table_auI_level_info.txt',skip_header = 1, delimiter ='\t',\
                             dtype = str)
for i in range(0,len(data_in[:,0])):
    data_in[i,5] = (data_in[i,5]).split(",")[0]
#%%
for i in range(0,len(level_labels[:,0])):
    output_temp = ''
    config = str(level_labels[i,1])
    total_j = level_labels[i,2]
    energy_l = str(round(float(level_labels[i,3]),2))
    energy_e = ''
    diff = ''
    uncert = ''
    no_lines = '0'
    if (i==0):
```

```
                energy_e = '0.0'
                diff = '0.0'
                uncert = '0.0'
                no_lines = data_in[0,5]
        if (i > 0):
            for j in range(1,len(data_in[:,0])):
                if (str(round(float(level_labels[i,0]))) == str(round(float(data_in[j,0])))):
                    energy_e = str(round(float(data_in[j,1])))+str('~$\pm$~')+str(data_in[j,3])
                    diff = round(float(data_in[j,1]) - float(energy_l),1)
                    #uncert = data_in[j,3]
                    no_lines = data_in[j,5]
        ref = str(level_labels[i,4])

        output_temp = str(config)+str('$_{')+str(total_j)+str('}$')+str('&')+str(energy_e)+str('&') \
        +str(energy_l)+str('&')+str(diff)+str('&') \
        + str(no_lines)+str('&')+str(ref)+str('\\\\')+str('\n')
        output = output + output_temp


text_file = open('AuI_levels_table.txt', "w")
text_file.write('%s' % output)
text_file.close()


os.chdir(paper_path)
text_file = open('AuI_levels_table.txt', "w")
text_file.write('%s' % output)
text_file.close()
os.chdir(cwd)
```

Listing 13 : LOPT Post-Processing: Compiling Wavelengths into LaTeX Tables

```
# -*- coding: utf-8 -*-
"""
SJB
06-17-19
script for turning data files into latex text
"""
##########################################
import sys
#define path for steve_lib.py
sys.path.insert(0, 'C:/Users/steve_000/Desktop/Research_Files/PRA_gold_spectroscopy')
#IMPORT EVERYTHING
from steve_lib import *
import math
from math import floor
def round_to_1(x):
    return round(x, -int(floor(math.log10(abs(x)))))
##########################################
paper_path = 'C:/Users/steve_000/Desktop/Research_Files/PRA_gold_spectroscopy/text'
```

```python
LOPT_folder = 'C:/Users/steve_000/Desktop/Research_Files/PRA_gold_spectroscopy/09-02-19/AuI_LOPT'

cwd = os.getcwd()

#%%
os.chdir(LOPT_folder)
au_I_lines_dat = glob.glob('au_I_lines*.txt')
data_in = np.genfromtxt(au_I_lines_dat[0], delimiter ='\t', dtype = str,skip_header=1)
levels_dat = glob.glob('au_I_levels*.txt')
levels = np.genfromtxt(levels_dat[0], delimiter='\t', dtype = str, skip_header = 1)
os.chdir(cwd)
level_labels = np.genfromtxt('table_auI_levels_input_08-30-19_update.txt',skip_header = 1, \
                             delimiter ='\t', dtype = str)
shot_list = genfromtxt('shots.csv',delimiter = ',')
references = np.genfromtxt('AuI_line_refs.txt', delimiter ='\t', usecols = (0,3),dtype =str)
#Grab the regions w/ wavelength ranges:
regions = genfromtxt('regions_with_wavelengths_AuI.txt', delimiter ='\t')
comments = np.genfromtxt('AuI_line_comments.txt', delimiter ='\t', dtype = str, usecols = (0,1))


#%%Remove commas from the number of lines part:
for i in range(0,len(levels[:,0])):
    levels[i,5] = (levels[i,5]).split(",")[0]
#%%grab relative intensities
line_list = np.empty((0,1))
for i in range(0,len(data_in[:,0])):
    if (data_in[i,1] != '_'):
        line = float(data_in[i,1])
        line = line / 10
        line_list = np.append(line, line_list)
line_list = line_list[line_list[:].argsort()]
probe2 = 'C:/Users/steve_000/Desktop/xray_filtered_data'
#%%
output = ''
#%%
#Choose whether you want the Ritz wavelengths to come from the experimental OR literature energies
#ritz_source = 'theory'
ritz_source = 'experimental'

line_intensities = intensity_search_v2(line_list, frame_in=83,normalize = 'True',scale_max = 100,\
                                       method = 'relative', regions = regions ,\
                                       data_directory=probe2,frame_source='file')
for r in range(0,len(regions[:,0])):
    #line_intensities = np.zeros((2,10))
    for i in range(0,len(data_in[:,0])):
        if (data_in[i,1] != '_'):
            if (regions[r,1] < float(data_in[i,1]) / 10 < regions[r,2]):
                output_temp = ''
                stdev = str(round_to_1(float(data_in[i,2]) / 10))
                wavelength = str(round(float(data_in[i,1]) / 10,2))+str('(') \
                +stdev.split(sep='.')[1]+str(')')
                for j in range(0,len(level_labels[:,0])):
                    if (data_in[i,13] != 'G0'):
```

```python
            if (str(round(float(data_in[i,13]))) == level_labels[j,0]):
                lower_level = str(level_labels[j,1])
                lower_j = str(level_labels[j,2])
                lower_e = float(level_labels[j,3])
        else:
            lower_level = str(level_labels[0,1])
            lower_j = str(level_labels[0,2])
            lower_e = float(0)

        if (str(round(float(data_in[i,14]))) == level_labels[j,0]):
            upper_level = str(level_labels[j,1])
            upper_j = str(level_labels[j,2])
            upper_e = float(level_labels[j,3])

if (ritz_source == 'theory'):
    ritz = val_vac_to_air(1e8 / (upper_e - lower_e)) / 10
    #ritz = round(0.9997e7 / (upper_e - lower_e),2)

if (ritz_source == 'experimental'):
    ritz = float(data_in[i,5]) / 10

#keep sig figs for ritz:
diff = str(round(float(data_in[i,1])/10 - float(ritz),2))

#round ritz for table
ritz = str(round(float(ritz),2))
##########################   INTENSITY   ########
check = 0
for k in range(0,len(line_intensities[:,0])):
    if (abs((float(data_in[i,1]) / 10) - line_intensities[k,0]) < .01):
        #intens = str('{:.2E}'.format(round(line_intensities[k,1],3)))
        intens = str('{:}'.format(int(round(line_intensities[k,1]+.3,0))))
        check = 1
if (check == 0):
        intens = str('1*')
##########################   REFERENCE   ########
ref = ''
for k in range(0,len(references[:,0])):
    if (abs((float(data_in[i,1]) / 10) - float(references[k,0])) < 0.02):
        ref = references[k,1]
if (ref == ''):
    ref = 'New'
comment = ''
for p in range(0,len(comments[:,0])):
    if (abs((float(data_in[i,1]) / 10) - float(comments[p,0])) < 0.03):
        comment = comments[p,1]
#################### OUTPUT ####################
output_temp = str(intens) + '&'+str(wavelength) + str('&') + str(ritz) \
+ str('&') + str(round(float(diff),2)) + str('&') + str(lower_level) \
+ str('&') +  str(lower_j) + str('&') + str(upper_level) + str('&') \
+ str(upper_j) + str('&') + str(comment) + str('&') +str(ref) \
+ str('\\\\') + str('\n')
```

```
                    #Note that python interprets the \f string as form feed and
                    #NOT a literal '\f' in text.
                    output = output + output_temp


            #############    WAVELENGTH REGIONS   #############
      if ((r != 16) or (r != 15)):
            output = output + str('\cline{1-10}') + str('\n')


text_file = open('AuI_lines_table.txt', "w")
text_file.write('%s' % output)
text_file.close()


os.chdir(paper_path)
text_file = open('AuI_lines_table.txt', "w")
text_file.write('%s' % output)
text_file.close()
os.chdir(cwd)
```

Bibliography

[1] A. WGLA, :, N. Brickhouse, J. Cowan, P. Drake, S. Federman, G. Ferland, A. Frank, W. Haxton, E. Herbst, K. Olive, F. Salama, D. W. Savin, and L. Ziurys, "Laboratory astrophysics and the state of astronomy and astrophysics," (2009), arXiv:0903.2469 [astro-ph.IM] .

[2] P. D. Mullen, R. S. Cumbee, D. Lyons, L. Gu, J. Kaastra, R. L. Shelton, and P. C. Stancil, Astrophys. J **844**, 7 (2017).

[3] T. E. Cravens, Geophysical Research Letters **24**, 105 (1997), https://agupubs.onlinelibrary.wiley.com/doi/pdf/10.1029/96GL03780 .

[4] K. Dennerl, Space Science Reviews **157**, 57 (2010).

[5] N. A. Schwadron and T. E. Cravens, Astrophys. J **544**, 558 (2000).

[6] J. B. Greenwood, I. D. Williams, S. J. Smith, and A. Chutjian, Phys. Rev. A **63**, 062707 (2001).

[7] R. Janev, M. Harrison, and H. Drawin, Nucl. Fusion **29**, 109 (1989).

[8] S. Katsuda, H. Tsunemi, K. Mori, H. Uchida, R. Petre, S. Yamada, H. Akamatsu, S. Konami, and T. Tamagawa, The Astrophysical Journal **756**, 49 (2012).

[9] M. Larsson, W. D. Geppert, and G. Nyman, Rep. Prog. Phys. **75**, 066901 (2012).

[10] Lallement, R., A&A **422**, 391 (2004).

[11] R. J. Mawhorter, A. Chutjian, T. E. Cravens, N. Djurić, S. Hossain, C. M. Lisse, J. A. MacAskill, S. J. Smith, J. Simcic, and I. D. Williams, Phys. Rev. A **75**, 032704 (2007).

[12] A. Bhardwaj, M. B. Dhanya, A. Alok, S. Barabash, M. Wieser, Y. Futaana, P. Wurz, A. Vorburger, M. Holmström, C. Lue, Y. Harada, and K. Asamura, Geosci. Lett. **2**, 10 (2015).

[13] R. J. Fonck, D. S. Darrow, and K. P. Jaehnig, Phys. Rev. A **29**, 3288 (1984).

[14] M. Tokar, M. Beckers, and W. Biel, Nuclear Materials and Energy **12**, 1298 (2017), proceedings of the 22nd International Conference on Plasma Surface Interactions 2016, 22nd PSI.

[15] J. S. Miller, H. S. Pullins, D. J. Levandier, Y. Chiu, and R. A. Dressler, J. Appl. Phys. **91**, 984 (2002).

[16] R. G. Roble and C. C. Ridley, Annales Geophys. **5A**, 369 (1987).

[17] L. Qian, A. G. Burns, B. A. Emery, B. Foster, G. Lu, A. Maute, A. D. Richmond, R. G. Roble, S. C. Solomon, and W. Wang, "The ncar tie-gcm," in *Modeling the IonosphereThermosphere System* (American Geophysical Union (AGU), 2014) Chap. 7, pp. 73–83, https://agupubs.onlinelibrary.wiley.com/doi/pdf/10.1002/9781118704417.ch7 .

[18] B. Friedman and G. DuCharme, J. Phys B: At. Mol. Opt. Phys. **50**, 115202 (2017).

[19] O. B. Firsov, Zh. Eksperim. I. Teor. Fiz. **21** (1951).

[20] D. Rapp and D. E. Francis, J. Chem Phys. **37**, 2631 (1962).

[21] D. P. Hodgkinson and J. S. Briggs, J. Phys. B: At. Mol. Phys. **9**, 255 (1976).

[22] B. G. Lindsay and R. F. Stebbings, J. Geophys. Res. **110**, A12213 (2005).

[23] Gu, Liyi, Kaastra, Jelle, and Raassen, A. J. J., A&A **588**, A52 (2016).

[24] Jorge, Alba, Errea, L. F., Illescas, Clara, and Méndez, L., Eur. Phys. J. D **68**, 227 (2014).

[25] A. Mller and E. Salzborn, Physics Letters A **62**, 391 (1977).

[26] S. Bliman, S. Dousson, B. Jacquot, and D. Van Houtte, J. Physique **42**, 1387 (1981).

[27] D. Lyons, R. S. Cumbee, and P. C. Stancil, The Astrophysical Journal Supplement Series **232**, 27 (2017).

[28] J. L. Nolte, P. C. Stancil, H. P. Liebermann, R. J. Buenker, Y. Hui, and D. R. Schultz, Journal of Physics B: Atomic, Molecular and Optical Physics **45**, 245202 (2012).

[29] R. S. Cumbee, P. D. Mullen, D. LyonsLyons, R. L. Shelton, M. Fogle, D. R. Schultz, and P. C. Stancil, The Astrophysical Journal **852**, 7 (2017).

[30] T. E. Cravens, I. P. Robertson, S. Snowden, K. Kuntz, M. Collier, and M. Medvedev, AIP Conference Proceedings **1156**, 37 (2009), https://aip.scitation.org/doi/pdf/10.1063/1.3211832 .

[31] D. Bodewits and R. Hoekstra, Atoms **7** (2019), 10.3390/atoms7010017.

[32] Simon Wedlund, Cyril, Bodewits, Dennis, Alho, Markku, Hoekstra, Ronnie, Behar, Etienne, Gronoff, Guillaume, Gunell, Herbert, Nilsson, Hans, Kallio, Esa, and Beth, Arnaud, A&A **630**, A35 (2019).

[33] E. D. Donets, V. I. Ilyushchenko, and V. A. Alpert, In Proceedings of the Premiere Conference Internationale sur les Sources d'Ions , 625 (1969).

[34] E. D. Donets, Review of Scientific Instruments **69**, 614 (1998), https://doi.org/10.1063/1.1148642 .

[35] M. A. Levine, R. E. Marrs, J. R. Henderson, D. A. Knapp, and M. B. Schneider, Physica Scripta **T22**, 157 (1988).

[36] R. Shyam, D. D. Kulkarni, D. A. Field, E. S. Srinadhu, D. B. Cutshall, W. R. Harrell, J. E. Harriss, and C. E. Sosolik, AIP Conf. Proc. **1640**, 129 (2015).

[37] J. D. Gillaspy, Physica Scripta **T71**, 99 (1997).

[38] "Dreebit gmbh," https://www.dreebit-ibt.com/.

[39] R. E. Marrs, S. R. Elliott, and D. A. Knapp, Phys. Rev. Lett. **72**, 4082 (1994).

[40] D. D. Kulkarni, C. D. Ahl, A. M. Shore, A. J. Miller, J. E. Harriss, C. E. Sosolik, and J. P. Marler, Rev. Sci. Instrum. **88**, 083306 (2017).

[41] J. Ullrich, R. Moshammer, A. Dorn, R. D. rner, L. P. H. Schmidt, and H. S.-B. cking, Reports on Progress in Physics **66**, 1463 (2003).

[42] M. Fogle, Private Communications.

[43] A. Kramida, Yu. Ralchenko, J. Reader, and and NIST ASD Team, NIST Atomic Spectra Database (ver. 5.6.1), [Online]. Available: https://physics.nist.gov/asd [2017, April 9]. National Institute of Standards and Technology, Gaithersburg, MD. (2018).

[44] V. Liccardo, M. Malheiro, M. S. Hussein, B. V. Carlson, and T. Frederico, The European Physical Journal A **54**, 221 (2018).

[45] M. G. Kozlov, M. S. Safronova, J. R. Crespo López-Urrutia, and P. O. Schmidt, Rev. Mod. Phys. **90**, 045005 (2018).

[46] M. Jaschek and S. Malaroda, Nature **225**, 246 (1970).

[47] B. N. G. Guthrie, Monthly Notices of the Royal Astronomical Society **206**, 85 (1984).

[48] K. Fuhrmann, Astronomy and Astrophysics Supplement Series **77**, 345 (1989).

[49] C. Sneden, J. E. Lawler, M. P. Wood, E. A. Den Hartog, and J. J. Cowan, Physica Scripta **89**, 114006 (2014).

[50] Castelli, F., Cowley, C. R., Ayres, T. R., Catanzaro, G., and Leone, F., A&A **601**, A119 (2017).

[51] B. Côté, C. L. Fryer, K. Belczynski, O. Korobkin, M. Chruślińska, N. Vassh, M. R. Mumpower, J. Lippuner, T. M. Sprouse, R. Surman, and R. Wollaeger, The Astrophysical Journal **855**, 99 (2018).

[52] M. R. Drout, A. L. Piro, B. J. Shappee, C. D. Kilpatrick, J. D. Simon, C. Contreras, D. A. Coulter, R. J. Foley, M. R. Siebert, N. Morrell, K. Boutsia, F. Di Mille, T. W.-S. Holoien, D. Kasen, J. A. Kollmeier, B. F. Madore, A. J. Monson, A. Murguia-Berthier, Y.-C. Pan, J. X. Prochaska, E. Ramirez-Ruiz, A. Rest, C. Adams, K. Alatalo, E. Bañados, J. Baughman, T. C. Beers, R. A. Bernstein, T. Bitsakis, A. Campillay, T. T. Hansen, C. R. Higgs, A. P. Ji, G. Maravelias, J. L. Marshall, C. M. Bidin, J. L. Prieto, K. C. Rasmussen, C. Rojas-Bravo, A. L. Strom, N. Ulloa, J. Vargas-González, Z. Wan, and D. D. Whitten, Science **358**, 1570 (2017).

[53] D. A. Coulter, R. J. Foley, C. D. Kilpatrick, M. R. Drout, A. L. Piro, B. J. Shappee, M. R. Siebert, J. D. Simon, N. Ulloa, D. Kasen, B. F. Madore, A. Murguia-Berthier, Y.-C. Pan, J. X. Prochaska, E. Ramirez-Ruiz, A. Rest, and C. Rojas-Bravo, Science **358**, 1556 (2017).

[54] R. Margutti, E. Berger, W. Fong, C. Guidorzi, K. D. Alexander, B. D. Metzger, P. K. Blanchard, P. S. Cowperthwaite, R. Chornock, T. Eftekhari, M. Nicholl, V. A. Villar, P. K. G. Williams, J. Annis, D. A. Brown, H. Chen, Z. Doctor, J. A. Frieman, D. E. Holz, M. Sako, and M. Soares-Santos, The Astrophysical Journal Letters **848**, L20 (2017).

[55] D. Watson, C. J. Hansen, J. Selsing, A. Koch, D. B. Malesani, A. C. Andersen, J. P. U. Fynbo, A. Arcones, A. Bauswein, S. Covino, A. Grado, K. E. Heintz, L. Hunt, C. Kouveliotou, G. Leloudas, A. J. Levan, P. Mazzali, and E. Pian, Nature **574**, 497 (2019).

[56] D. Kasen, N. R. Badnell, and J. Barnes, The Astrophysical Journal **774**, 25 (2013).

[57] C. J. Fontes, C. L. Fryer, A. L. Hungerford, R. T. Wollaeger, and O. Korobkin, Monthly Notices of the Royal Astronomical Society (2019), preprint.

[58] P. Quinet, Canadian Journal of Physics **95**, 790 (2017).

[59] A. Kramida, Atoms **7** (2019), 10.3390/atoms7030064.

[60] Ryabchikova, T., Ryabtsev, A., Kochukhov, O., and Bagnulo, S., Astronomy & Astrophysics **456**, 329 (2006).

[61] S. J. Bromley, D. C. Fox, C. E. Sosolik, J. E. Harriss, and J. P. Marler, Rev. Sci. Instrum. **89**, 073107 (2018).

[62] S. Bromley, C. E. Sosolik, and J. P. Marler, Journal of Physics B: Atomic, Molecular and Optical Physics **52**, 215203 (2019).

[63] S. Bromley, C. Ahl, C. Sosolik, and J. Marler, Atoms **7** (2019), 10.3390/atoms7040096.

[64] C. J. Foot, *Atomic Physics*, 1st ed. (Oxford University Press, Oxford, 1995).

[65] T. Tom and B. D. James, J. Vac. Sci. Technol **6**, 304 (1969).

[66] B. P. Mathur, J. E. Field, and S. O. Colgate, Phys. Rev. A **11**, 830 (1975).

[67] H. Martinez, F. Castillo, P. Reyes, and F. Santibaez, Int. J. Mass Spectrom **228**, 107 (2003).

[68] A. Dalgarno and M. R. C. McDowell, Proceedings of the Physical Society. Section A **69**, 615 (1956).

[69] S. H. po, R. A. Dressler, R. Torrents, and D. Gerlich, Z. Phys. Chem. **214**, 1279 (2000).

[70] M. B. Shah, J. Geddes, B. M. McLaughlin, and H. B. Gilbody, Journal of Physics B: Atomic, Molecular and Optical Physics **31**, L757 (1998).

[71] R. S. Gao, L. K. Johnson, D. A. Schafer, J. H. Newman, K. A. Smith, and R. F. Stebbings, Phys. Rev. A **38**, 2789 (1988).

[72] J. Baudon, M. Barat, and M. Abignoli, J. Phys. B: At. Mol. Phys. **1**, 1083 (1968).

[73] M. Barat, J. Baudon, M. Abignoli, and J. C. Houver, J. Phys. B: At. Mol. Phys. **3**, 230 (1970).

[74] V. Sidis, M. Barat, and D. Dhuicq, J. Phys. B: At. Mol. Phys. **8**, 474 (1975).

[75] R. Hegerberg, T. Stefansson, and M. T. Elford, J. Phys. B: At. Mol. Phys. **11**, 133 (1978).

[76] V. S. Nikolaev, I. S. Dmitriev, L. N. Fateeva, and Y. A. Teplova, Sov. Phys. JETP **40**, 23 (1975).

[77] W. H. Cramer and J. H. Simons, J. Chem. Phys. **26**, 1272 (1957), https://doi.org/10.1063/1.1743506 .

[78] H. B. Gilbody and J. B. Hasted, Proc. Royal Soc. Lond **238**, 334 (1956).

[79] B. I. Kikiani, Z. E. Saliya, and I. G. Bagdasarova, Zh. Tekh. Fiz. **45**, 586 (1975).

[80] J. A. Dillon, W. F. Sheridan, H. D. Edwards, and S. N. Ghosh, J. Chem. Phys. **23**, 776 (1955), https://doi.org/10.1063/1.1742120 .

[81] L. P. Flaks and E. S. Solov'ev, Sov. Phys. Tech. Phys. **3**, 564 (1958).

[82] M. Hause, B. Prince, and R. Bemish, J. Appl. Phys. **113**, 163301 (2013).

[83] A. Galli, A. Giardini-Guidoni, and G. G. Volpi, Il Nuovo Cimento (1955-1965) **26**, 845 (1962).

[84] R. M. Kushnir, B. M. Palyukh, and L. A. Sena, Izv. Akad. Nauk SSSR Ser. Fiz. **23**, 1007 (1959).

[85] H. S. W. Massey, Rep. Prog. Phys. **12**, 248 (1949).

[86] T. Kusakabe, S. Kitamuro, Y. Nakai, H. Tawara, and M. Sasao, Plasma Fusion Res. **7** (2012), 10.1585/pfr.7.2401062.

[87] G. T. V. Rudd, M. E. and A. Itoh, Phys. Rev. A **32**, 829 (1985).

[88] T. F. Moran and R. J. Conrads, The Journal of Chemical Physics **58**, 3793 (1973), https://doi.org/10.1063/1.1679732 .

[89] G. J. Lockwood, Phys. Rev. A **2**, 1406 (1970).

[90] D. W. Koopman, Phys. Rev. **166**, 57 (1968).

[91] R. F. Stebbings, A. C. H. Smith, and H. Ehrhardt, The Journal of Chemical Physics **39**, 968 (1963), https://doi.org/10.1063/1.1734399 .

[92] C. F. Barnett and P. M. Stier, Phys. Rev. **109**, 385 (1958).

[93] W. G. Graham, C. J. Latimer, R. Browning, and H. B. Gilbody, Journal of Physics B: Atomic and Molecular Physics **6**, 2641 (1973).

[94] A. F. Hedrick, T. F. Moran, K. J. McCann, and M. R. Flannery, The Journal of Chemical Physics **66**, 24 (1977), https://doi.org/10.1063/1.433673 .

[95] C. J. Latimer, Journal of Physics B: Atomic and Molecular Physics **10**, 515 (1977).

[96] P. Mahadevan and G. D. Magnuson, Phys. Rev. **171**, 103 (1968).

[97] W. Wolff, I. J. de Souza, A. C. Tavares, G. F. S. de Oliveira, and H. Luna, Review of Scientific Instruments **83**, 123107 (2012), https://doi.org/10.1063/1.4772395 .

[98] M. Kitajima, Y. Nakai, Y. Kanai, Y. Yamazaki, and Y. Itoh, Physica Scripta **T80**, 377 (1999).

[99] G. Scoles, *Atomic and Molecular Beam Methods*, Vol. 1 (Oxford University Press, 1988) pp. 16–52.

[100] A. Na and E. Steffens, Nuclear Instruments and Methods in Physics Research Section A: Accelerators, Spectrometers, Detectors and Associated Equipment **598**, 653 (2009).

[101] H. Schmidt, H. Cederquist, R. Schuch, L. Bagge, A. Källberg, J. Hilke, K.-G. Rensfelt, V. Mergel, M. Achler, R. Dörner, L. Spielberger, O. Jagutzki, H. Schmidt-Böcking, J. Ullrich, H. Reich, M. Unverzagt, W. Schmitt, and R. Moshammer, Hyperfine Interactions **108**, 339 (1997).

[102] H. Buchenau, E. L. Knuth, J. Northby, J. P. Toennies, and C. Winkler, The Journal of Chemical Physics **92**, 6875 (1990), https://doi.org/10.1063/1.458275 .

[103] H. Koivisto, J. Arje, and M. Nurmia, Review of Scientific Instruments **69**, 785 (1998), https://doi.org/10.1063/1.1148539 .

[104] T. Werner, G. Zschornack, F. Gromann, V. P. Ovsyannikov, and F. Ullmann, Review of Scientific Instruments **71**, 2038 (2000), https://doi.org/10.1063/1.1150574 .

[105] J. H. Moore, C. C. Davis, M. A. Coplan, and S. C. Greer, *Building Scientific Apparatus*, 4th ed. (Cambridge University Press, 2009).

[106] M. Fox, *Quantum Optics: An Introduction*, 1st ed. (Oxford University Press, Oxford, 2006).

[107] J. C. Ehrhardt and S. P. Davis, J. Opt. Soc. Am. **61**, 1342 (1971).

[108] M. Rosberg and J.-F. Wyart, Physica Scripta **55**, 690 (1997).

[109] S. E. Yoca, É. Biémont, F. Delahaye, P. Quinet, and C. J. Zeippen, Physica Scripta **78**, 025303 (2008).

[110] J. R. Platt and R. A. Sawyer, Phys. Rev. **60**, 866 (1941).

[111] C. H. Corliss and W. R. Bozman, *NBS Monograph, Washington: US Department of Commerce, National Bureau of Standards, —c1962* (1962).

[112] H. Bucka and J. Ney, Zeitschrift für Physik **194**, 208 (1966).

[113] P. Hannaford, P. L. Larkins, and R. M. Lowe, Journal of Physics B: Atomic and Molecular Physics **14**, 2321 (1981).

[114] O. Poulsen, T. Andersen, S. Bentzen, and I. Koleva, Nuclear Instruments and Methods in Physics Research **202**, 139 (1982).

[115] M. B. Gaarde, R. Zerne, L. Caiyan, J. Zhankui, J. Larsson, and S. Svanberg, Phys. Rev. A **50**, 209 (1994).

[116] V. Fivet, P. Quinet, É. Biémont, and H. L. Xu, Journal of Physics B: Atomic, Molecular and Optical Physics **39**, 3587 (2006).

[117] M. Zhang, L. Zhou, Y. Gao, Q. Yu, X. Wang, Q. Wang, Y. Gong, and Z. Dai, Journal of Physics B: Atomic, Molecular and Optical Physics **51**, 205001 (2018).

[118] G. Hartwell, S. Knowlton, J. Hanson, D. Ennis, and D. Maurer, Fusion Science and Technology **72**, 76 (2017).

[119] C. A. Johnson, D. A. Ennis, S. D. Loch, G. J. Hartwell, D. A. Maurer, S. L. Allen, B. S. Victor, C. M. Samuell, T. Abrams, E. A. Unterberg, and R. T. Smyth, Plasma Physics and Controlled Fusion **61**, 095006 (2019).

[120] L. H. Negri, "Peakutils," (2017), online; accessed 02-20-19.

[121] E. Jones, T. Oliphant, P. Peterson, *et al.*, "SciPy: Open source scientific tools for Python," (2001–), online; accessed 02-20-19.

[122] C. Johnson, S. Loch, and D. Ennis, Nuclear Materials and Energy , 100579 (2019).

[123] H. P. Summers, "The adas user manual," (2004), version 2.6.

[124] D. C. Morton, The Astrophysical Journal Supplement Series **130**, 403 (2000).

[125] A. Kramida, Computer Physics Communications **182**, 419 (2011).

[126] W. Whaling, M. Carle, and M. Pitt, Journal of Quantitative Spectroscopy and Radiative Transfer **50**, 7 (1993).

[127] C. M. Brown and M. L. Ginter, J. Opt. Soc. Am. **68**, 243 (1978).

[128] L. Iglesias, J. Res. Natl. Bur. Stand. (U.S.), Sect. A **64A**, 481 (1960).